Development and Characterization of a Novel Hybrid Magnetorheological Elastomer

Karl Adams-Gillstrom
A Thesis
In the Department of
Mechanical, Industrial, and Aerospace Engineering

Presented in Partial Fulfillment of the Requirements
For the Degree of Master of Applied Science
at
Concordia University
Montreal, Quebec, Canada

August 2024

Abstract

Development and Characterization of a Novel Hybrid Magnetorheological Elastomer

Karl Adams-Gillstrom

Over the past few decades, functional magnetorheological (MR) materials have been extensively researched due to their field-dependent adaptive mechanical properties, which hold substantial promise for implementing semi-active vibration control across various engineering applications. MR elastomers (MRE) are the solid analogue of well-known MR fluids (MRF), where micron-sized ferromagnetic particles are integrated within an elastomeric medium rather than a carrier fluid. In contrast to MRFs, which provide field-dependent variable damping properties, MREs exhibit adjustable stiffness and damping characteristics. MREs also do not experience the sedimentation of magnetic particles and leakage often encountered in MRF-based systems.

While there are several studies related to the characterization of MREs operating in shear mode under varying mechanical and magnetic excitation conditions, there are very few studies on the characterization of MREs under compression mode. In particular, the characterization of hybrid MREs, in which MRF is encapsulated within MREs, has been rarely investigated.

The objective of the present research is to systematically characterize and compare the viscoelastic properties and dynamic behavior of MREs, MRF-Es (where MR fluid is encapsulated within an elastomeric matrix), and new hybrid MRF-MREs (where MR fluid is encapsulated within MREs), considering the effects of design factors (i.e., shape factor and shape) and mechanical and magnetic loading conditions. To accomplish this, eight different samples of MREs, MRF-Es, and MRF-MREs were fabricated. Dynamic characterization was performed in compression mode under harmonic excitations with varying strain amplitude, frequency, and applied current, ranging from (2.5% to 15%), (0.088 Hz to 10 Hz), and (0 A to 8 A), respectively. Results suggested superior performance of MRF-MREs, exhibiting a relative MR effect of nearly 478%, almost three times that of its counterpart, the MRF-E, and surpassing the MRE by a factor of ten under identical loading conditions.

Finally, a phenomenological model was developed based on the modified viscoelastic Kelvin-Voigt model to predict the viscoelastic storage and loss moduli of MREs, MRF-Es, and MRF-MREs as functions of frequency, strain amplitude, and current. The developed model was subsequently used to derive the transmissibility response of an adaptive single-degree-of-freedom (SDOF) system to investigate its capability to tune the natural frequency. An experimental test setup was also designed to confirm the variation in natural frequency of the SDOF system under varying current.

Acknowledgment

Firstly, I would like to thank my supervisor, Prof. Ramin Sedaghati, along with Prof. Subnash Rakheja for trusting and bringing me into their research group. Their kind patience and guidance were greatly appreciated.

I would also like to express my gratitude to the people who helped me throughout this process.

Seyed Alireza Moezi, who assisted with the manufacturing of all the samples in this paper. His knowledge and dedication to help were undeniably of great importance.

Dr. Hossein Vatandoost, who provided his loyal and utmost constant support even in the most inconvenient of times.

Lastly, my great friends and family for their help in keeping me focused and constant support.

Table of Contents

List of Figures

List of Tables

Nomenclature

A_{MRE}	Loading area of MR sample
c_{MRE}	Equivalent damping of MR sample
E'	Compression elastic modulus
E''	Compression loss modulus
$\dot{\varepsilon}$	Rate of strain in compression mode
ε	Strain in compression mode
ε_0	Strain amplitude in compression
σ	Compression stress
σ_0	Mean compression stress
ρ	Density
F_{mg}	Electromagnetic force in absence of MR sample
F_{MRE}	Viscoelastic force of MR sample
F_{Total}	Total load cell force
f	Frequency of oscillation (Hz)
f_n	Natural frequency (Hz)
f_0	Reference frequency of 1 Hz
I	Current (A)
ff	Minimum function
k_{MRE}	Equivalent stiffness of MR sample
l_{MRE}	Height of MR sample
$norm$	Normalized function

m_c	Mass of upper section of electromagnetic core
m_p	Payload mass
m	Total active mass
MR	Magneto-rheological
MRE	Magnetorheological elastomer
MRF	Magnetorheological fluid
MRF-E	Encapsulated Magnetorheological fluid
MRF-MRE	Magnetorheological fluid encapsulated in MRE
SF	Shape Factor
t	Time interval
V	Volume
ω	Angular frequency
$\ddot{y}$	Acceleration of active mass
$\dot{y}$	Velocity of active mass
y	Displacement of active mass
$\frac{Y}{Z}$	Displacement transmissibility
$\dot{z}$	Velocity of base
z	Displacement of base

Chapter 1: Introduction

1.1 Literature Review of Magnetorheological Materials

Magnetorheological (MR) materials represent a fascinating class of smart materials that have garnered increasing attention due to their unique ability to alter their rheological properties when subjected to a magnetic field. This remarkable characteristic holds immense promise for a wide range of engineering applications to form smart composite structures whose mechanical response can be actively controlled in real-time [1, 2].

Magnetorheological materials are typically composed of micron-sized ferromagnetic particles suspended within a non-magnetic matrix, such as fluid, gel, or rubber-like materials [3]. These magnetic particles, typically on the order of a few micrometers in size, are the key to the unique properties of MR materials. When an external magnetic field is applied, the magnetic particles align along the field lines, creating a chain-like structure within the matrix [3]. This alignment leads to a rapid change in the mechanical and rheological properties of the MR material. The extent of this transformation depends on design and loading factors. The design factors include but are not limited to, particle size, particle volume/weight, and matrix type. Additionally, the loading parameters, such as the strength of the magnetic field, applied pre-strain/stress, frequency, and strain amplitude, all collectively influence the field-dependent properties of MR materials [3]. As the magnetic field is removed, the particles return to their random orientation, and the material regains its original properties.

The dynamic response of MR materials to applied external magnetic fields is almost instantaneous (in the order of milliseconds) [1], allowing for near real-time control and adjustment. MR fluids

(MRF) and MR elastomers (MRE) are the most utilized MR materials, primarily because of their strong MR effect (the ratio of the material properties at an applied magnetic field to that in the absence of magnetic field) and their potential to be applied across a wide range of applications.

1.1.1 Magnetorheological Fluid (MRF)

MR fluids consist of two main components: the base carrier fluid and the micron-sized magnetizable particles. The carrier fluids are selected based on their rheological and temperature stability with respect to the application [4]. The base fluid is typically an oil, which serves as the carrier medium for the magnetic particles. Typical carrier fluids include mineral and silicone oils, polyesters, polyethers, synthetic hydrocarbons, and water [4, 5]. The size of the magnetic particles typically ranges from micrometers to nanometers, where iron or cobalt particles are often selected for their high permeability and saturation magnetization [6].

In MR fluids, applying an external magnetic field causes ferromagnetic particles to become dipoles, which interact to form columnar structures that align approximately parallel to the applied magnetic field [5] as shown in Figure 1.1. These chain-like structures restrict the flow of the fluid, thereby increasing its apparent viscosity and yield strength, nearly transforming it into a semi-solid material [7]. The arrangement and rigidity of these structures are influenced by several factors including, the strength and distribution of the applied magnetic field, the volume fraction and distribution of magnetic particles, and the formation of agglomerates [8]. The mechanical energy required to deform these chain-like structures rises with the increase in applied magnetic field strength, leading to a field-dependent yield stress [4]. The material recovers to its fluid state when the magnetic field is removed.

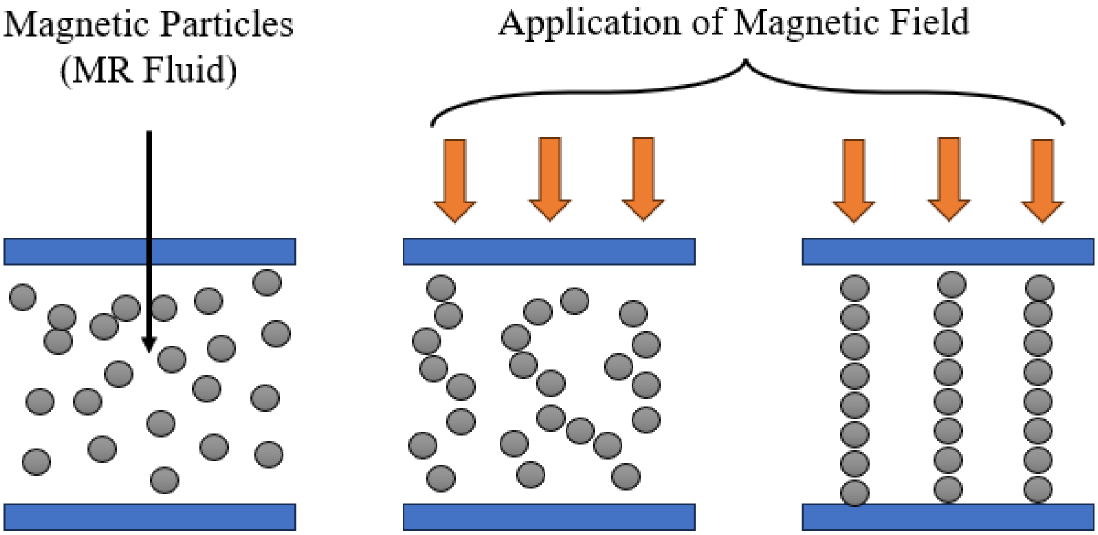

Figure 1.1: Chain structure of magnetic particles upon application of an increasing magnetic field (left to right)

MR fluids have found diverse applications across numerous industries, but they have shown great success in the automotive industry, particularly in suspension systems, where they provide adaptive damping capabilities to shock absorbers and dampers (Figure 1.2 & Figure 1.3) [9-13]. By adjusting the strength of the magnetic field, the damping characteristics can be dynamically changed to enhance vehicle comfort, stability, and performance [5]. In addition, MR disc brakes (Figure 1.4) have also been investigated [14, 15], where a rotating MR brake can provide variable braking torque through the activation of the MR fluid sandwiched in the gap between the driving disk and braking disk, resulting in effective braking on the rotor surface.

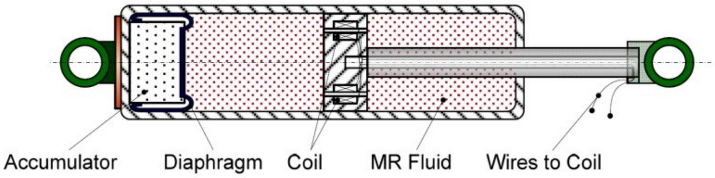

(a) Hardware structure

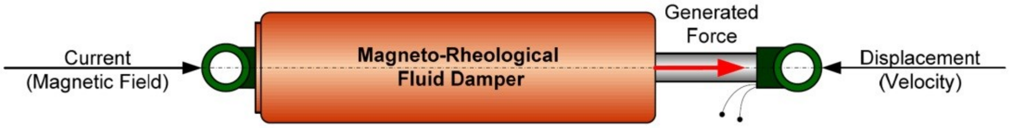

(b) Working principle

Figure 1.2: Magnetorheological linear damper [9]

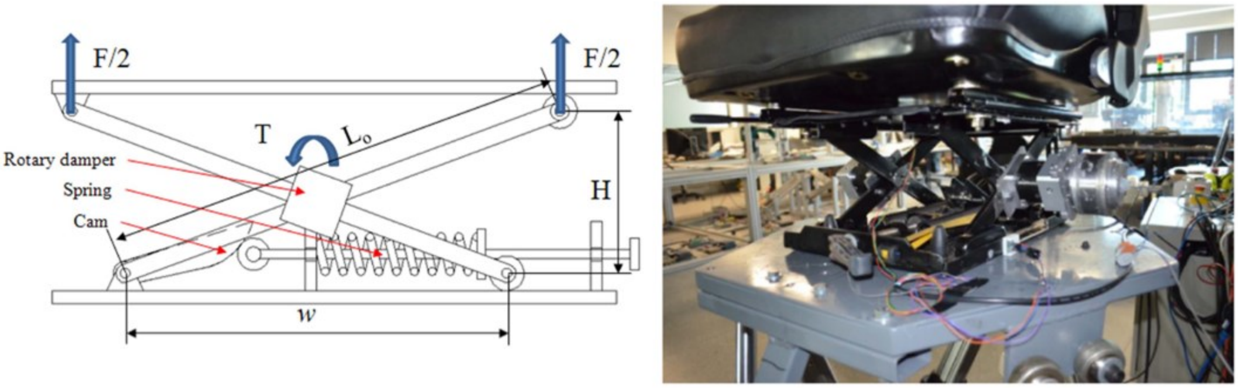

Figure 1.3: Structure of MR rotary damper seat suspension: working mechanism (Left); photograph of the suspension system (Right) [16]

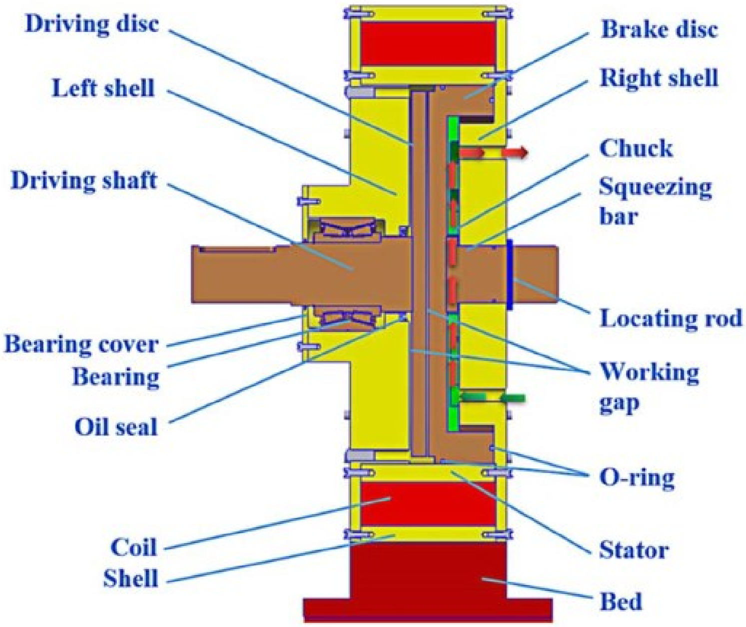

Figure 1.4: Magnetorheological fluid disc brake [10]

There are also known potential uses of MR fluids in civil infrastructures, as adaptive seismic dampers and base isolators that can adapt to the intensity of seismic activity [17, 18], thus improving the resilience of buildings, bridges, and infrastructure. Similarly, in the biomedical field, potential applications include prosthetic limbs to enhance mobility and shock absorption [19, 20].

MRFs do, however, have some shortcomings. One of the main drawbacks of MR fluids is the sedimentation and agglomeration of the magnetic particles, which significantly affects the performance of the MR effect exhibited by MR fluids. Sedimentation of the magnetic particles generally occurs within the carrier fluid after a certain period of inactivity due to the large density differences between the magnetic particles and the carrier fluids [21]. Agglomeration of the magnetic particles also occurs due to the application and removal of the magnetic field causing the existence of remnant magnetization in the magnetic particles [21]. Additives are generally used to prevent sedimentation and agglomeration. Surfactants and thickeners, such as oleic acid, tetramethylammonium hydroxide, fluorocarbon grease, colloidal clays, and silica, can be used to delay particle settling and facilitate re-dispersion by disrupting flow at ultralow shear rates [21]. Alternatively, coatings of particles, thixotropic agents, and nanoparticles to keep particles separated, have shown to hinder agglomeration [21-23]. Furthermore, due to the fluidic nature of the matrix rather than solid-state, issues such as liquid leakage, oxidation of particles, fluid particle separation, and reliance on containment measures may render MR fluids less desirable for specific applications [6].

1.1.2 Magnetorheological Elastomer (MRE)

The solid counterpart of MR fluids is the magnetorheological elastomer (MRE), which is composed of an elastomer matrix impregnated with micron-sized magnetic particles. The elastomeric matrix is typically made of polymers like silicone rubber, which provides the material with its elasticity. Other materials, such as polyurethane, thermosets/thermoplastic elastomers, interpenetrating polymer networks, and natural/synthetic rubber, have been used in other studies. However, silicone rubber has been adopted by more than 56% of studies as its initial liquid state allows for ease of particle dispersion [1]. The most crucial feature of the matrix material, apart from its rheological properties, is that it must have a low magnetic permeability. If the matrix material has high magnetic permeability, the polarization of the particles will be less effective, and the MR effect will therefore be smaller [3].

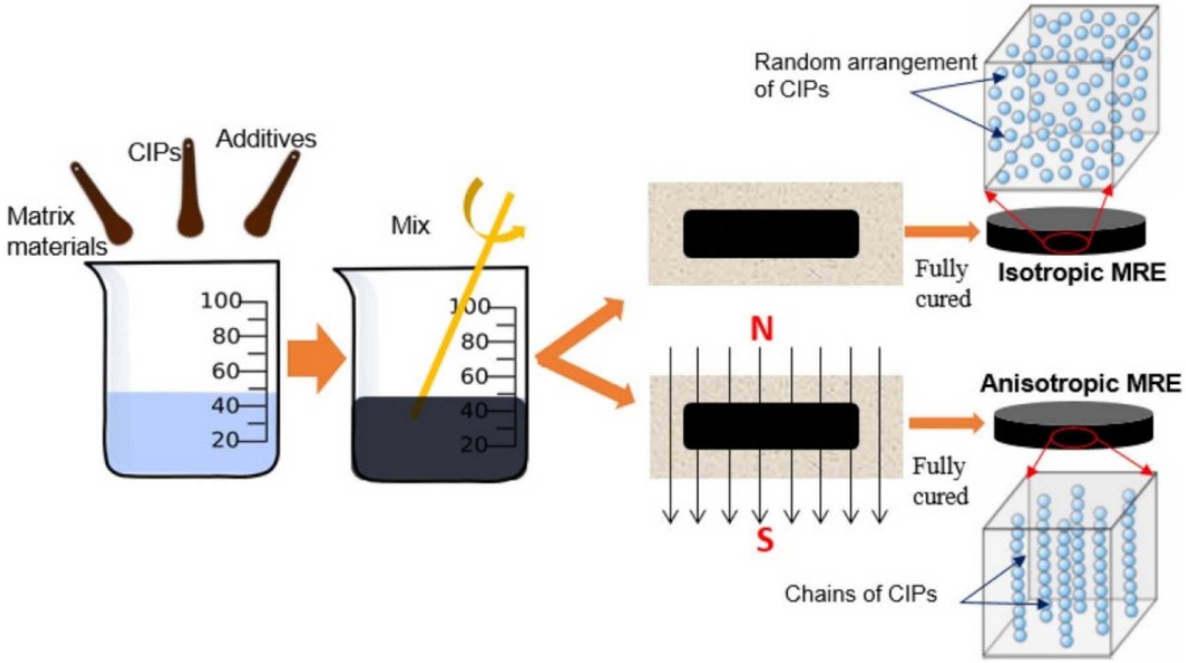

Figure 1.5: Schematic of typical MRE fabrication process [1]

MREs can be categorized in the form of isotropic and anisotropic configurations. The conventional method of MRE fabrication, as shown in Figure 1.5, starts with the silicone rubber in its initial liquid state. Once mixing the silicone rubber with the desired volume/weight fraction of magnetic particles and, if needed, other additives, the mixture is allowed to cure at room temperature. For an anisotropic MRE, a magnetic field is applied during crosslinking so that columnar particle structures form and become locked in place upon the final cure. For an isotropic MRE, no external magnetic field is applied during the curing process, which leaves the magnetic particles randomly dispersed and locked within the elastomer matrix after the mixture is fully cured [1]. In general, most studies have found that anisotropic MREs generate a higher MR effect in shear and compression mode as compared with isotropic MREs [24]. However, at high levels of pre-strain or strain amplitude, isotropic MREs have often shown higher MR effect as compared with anisotropic MREs due to the collapse of the anisotropic columnar structures [24-26].

The field-dependent mechanical characteristics of MREs are strongly influenced by the microstructure formed during the curing process of the elastomer matrix. When a magnetic field is applied to MREs, the particles' minimum energy state shifts, necessitating additional work that increases with the magnetic field strength due to the interactions between the magnetic particles (Figure 1.6) [3, 8]. Therefore, viscoelastic properties, such as storage and loss moduli, of MREs are strongly dependent on the strength of the magnetic field. The volume fraction of ferromagnetic particles also substantially affects the field-dependent viscoelastic properties of MREs [27].

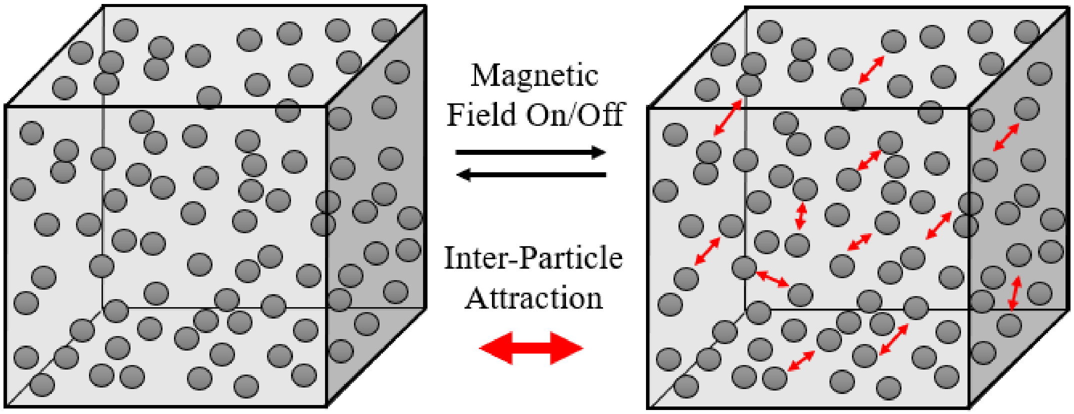

Figure 1.6: Magnetic particle interaction for MREs

Due to their adaptive field-dependent damping and stiffness properties, MREs can be effectively used for development of adaptive vibration absorbers and isolators to attenuate transmitted vibrations across a wide range of frequencies [28]. A number of studies have shown successful application of MREs [28-31] (Figure 1.7 & Figure 1.8).

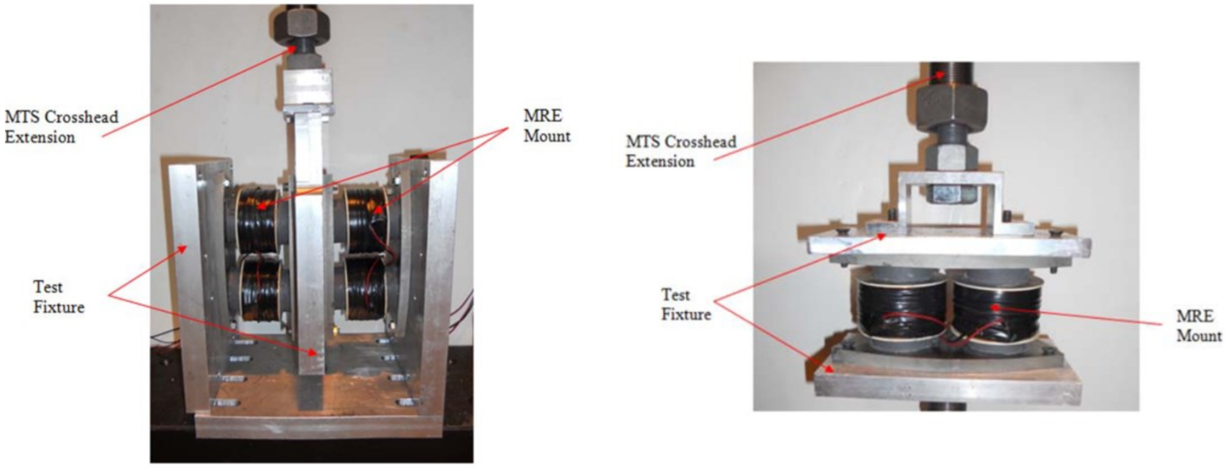

Figure 1.7: MRE mount shear (left) & compression (right) experiment setup [30]

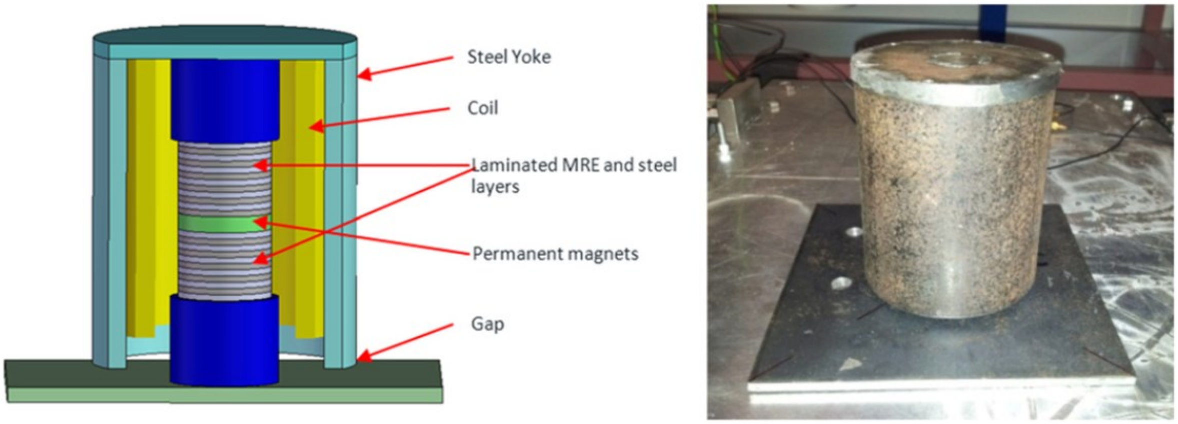

Figure 1.8: Structure (left) & Prototype (right) of laminated MRE absorber [31]

MREs provide both variable damping and stiffness and overcome the sedimentation problem of MR fluids, although they generally exhibit a lower MR effect compared to MR fluids [32]. Various efforts have been devoted to enhancing the MR effect of conventional MR elastomers. Commonly, additives can be used to achieve better results. Plasticizers, such as silicone oil, mineral oil, and silicone-based esters, can be dissolved in the matrix materials to facilitate the molecular chains to glide [1]. Carbon-based additives, such as carbon black, carbon nanotubes, and magnetic nanoparticles, may also be used to fill the voids between the magnetic particles, thus increasing the magnetic properties [1]. Additionally, increasing the shape factor has been shown to strongly improve MR effect [33]. While MREs provide variation in both stiffness and damping, their MR effect in view of damping is still lower compared to MR fluids. Therefore, there is a need for the development of new hybrid MRE materials that can incorporate the merits of both MR fluids and MR elastomers [34].

1.1.3 Hybrid Magnetorheological Elastomer

MREs generally exhibit limited damping variation as well as lower response time compared with their MR fluids counterparts [35, 36]. This is attributed to the suspension of magnetic particles with an elastomeric matrix which provide limited magnetic particle movement within the matrix. This limitation of MREs has led to the development of new class of materials known as hybrid MREs [35]. In hybrid MREs, an MR fluid may be encapsulated within a purely passive elastomeric matrix namely MRF-E or a MRE namely MRF-MRE as shown in Figure 1.9.

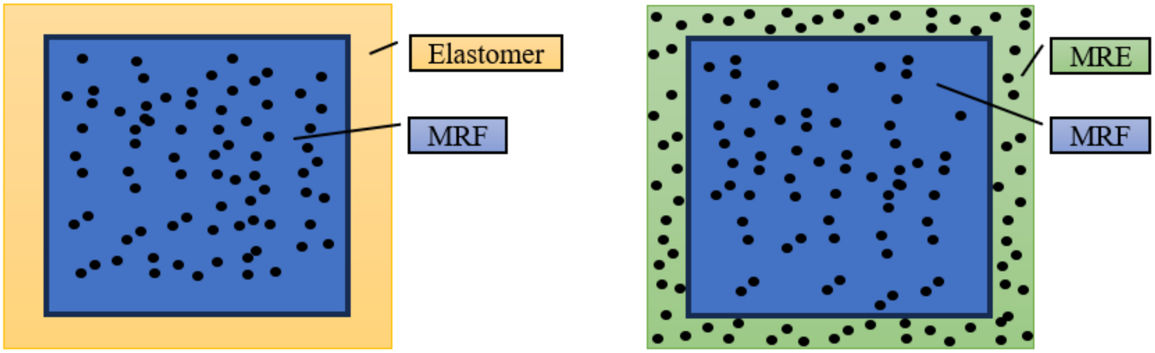

Figure 1.9: Basic section view sketch of an MRF-E (left) & MRF-MRE (right)

The existing research on the characterization of hybrid MREs has been mainly limited to several studies. For MRF-Es, Bastola et al. [34], developed a soft hybrid MRF-E by encapsulating MRF within a UV curable elastomeric matrix. The fabricated process and sample are shown in Figure 1.10. The objective of the study was to comprehend the effect of the concentration of the magnetic particles in the liquid core and the effect of viscosity in the liquid core in compression mode. They showed that a high viscosity MRF at the core practically overcomes the sedimentation of magnetic particles in MRF and exhibited a higher MR effect compared with low viscosity MRF.

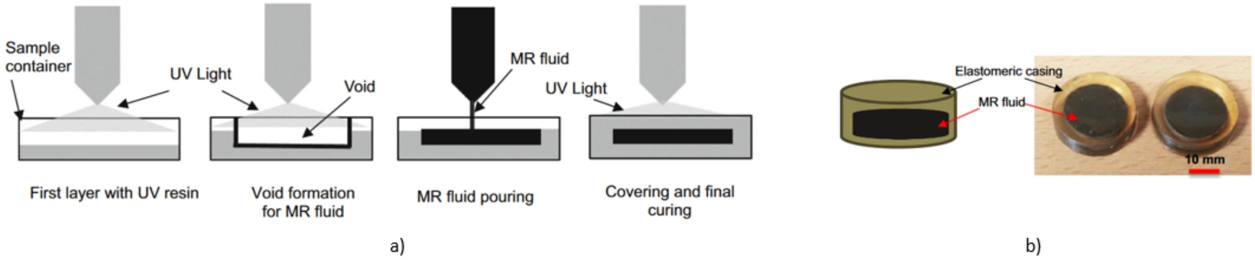

Figure 1.10: (a) Schematic illustration of fabrication process for MRF-E: (b) Photograph of MRF-E sample [37]

Bastola et al. [38], also developed a novel MRF-E using 3D printing technology in which MRF was encapsulated layer by layer into a UV-curable silicone sealant (Figure 1.11). The fabricated process produced samples with different MRF patterns, shown in Figure 1.12. The experimental results on the fabricated composite MRF-Es suggested that the developed MRF-Es can generate higher MR effect in view of damping compared with that of stiffness. Similar results were also found by Wang and Gordaninejad [39] under a compressive vibration isolator mount using a conventional MRF-E sample.

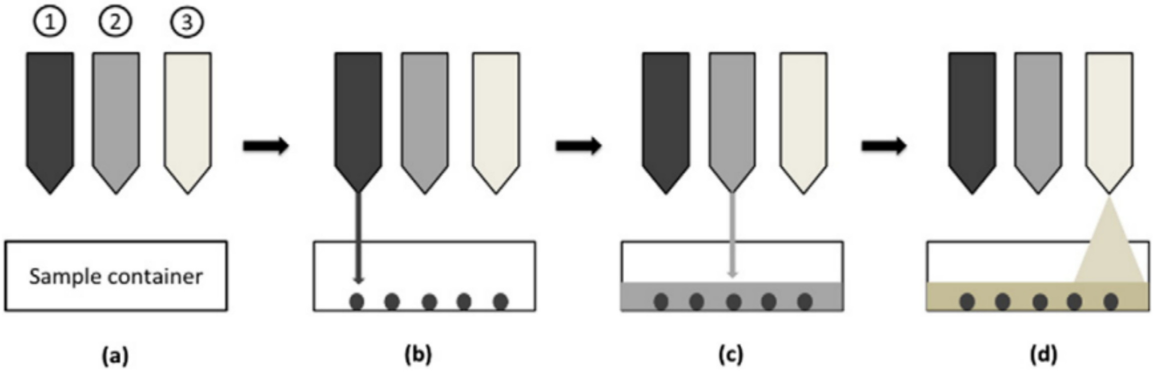

Figure 1.11: Schematic diagram 3D printed fabrication process of MRF-E (a) Three printing components: (1) MR fluid cartridge, (2) elastomer resin cartridge, (3) UV curing unit. (b) Printing of MR fluid (c) Dispensing of elastomer resin (d) Curing with UV light [38]

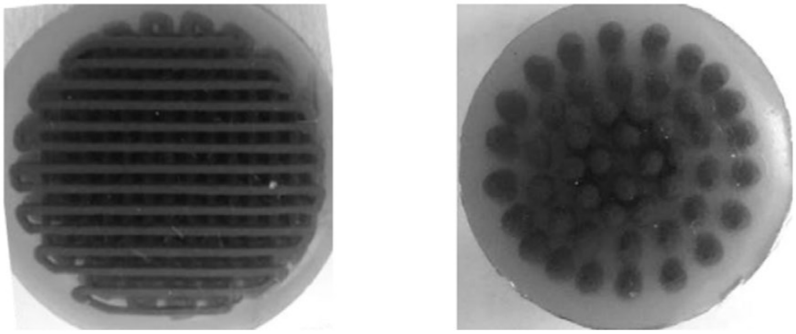

Figure 1.12: 3D printed MRF-E samples: Line formation pattern (left); Circular jointed dotted pattern (right) [38]

Compared with conventional MREs and hybrid MRF-Es, there are only very limited studies on the characterization of MRF-MREs. Zhang et al. [40] explored anisotropic MRF-MREs in which columnar holes (1.5mm diameter) were punched into the conventional MREs and filled with MR fluid and MR gels to form chain like structures within the elastomer matrix as shown in Figure 1.13. Experimental results showed that in shear mode, the new hybrid MRE generate higher MR effect compared with conventional MREs.

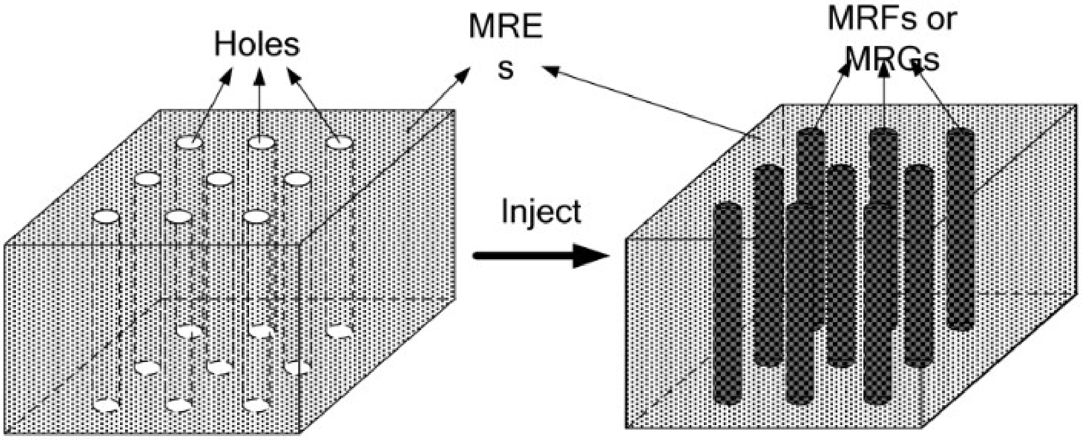

Figure 1.13: Schematic diagram of hybrid samples with holes [40]

Choi and Wereley [41] investigated four different designs of hybrid MREs in order to measure their controllable mechanical properties range in compression mode (Figure 1.14). The samples consisted of two MRF-MRE samples of different encapsulated designs, and two MRF-Es of different MR fluid viscosities and volume fractions. Comparison of the samples concluded that the MRF-MRE which utilized an MRE base on top of which sat a passive silicone rubber encapsulant provided the widest range of controllable mechanical properties.

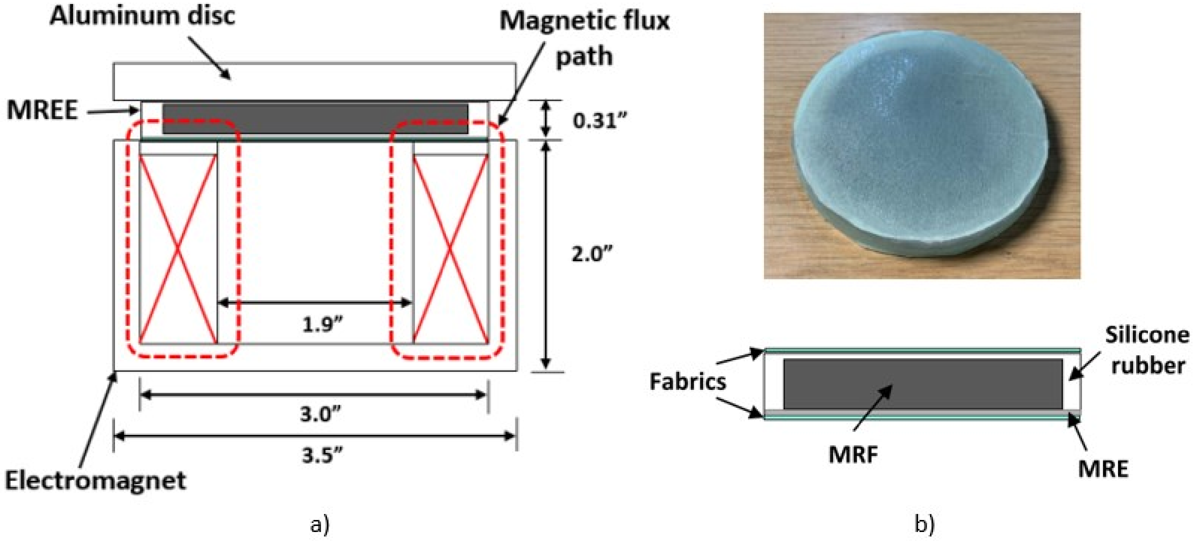

Figure 1.14: (a) Schematic of experimental setup (b) Fabricated MRF-MRE sample [41]

Few studies have shown the superior performance of hybrid MREs (compared with conventional MREs) in development of adaptive vibration absorption and isolation devices [35, 36]. While there are a number of studies on hybrid MREs, no fundamental research study has been conducted to investigate the effect of host elastomeric matrix, sample shape and shape factor while under a wide range of mechanical and magnetic load excitations on the field dependent properties of hybrid MREs.

1.3 Scope and Objectives

The main goal of this research is to conduct systematic study to investigate the field-dependent viscoelastic behaviour of various types of hybrid MREs, including MRF-MREs and MRF-Es, as well as MREs of different shape and shape factors, under a wide range of excitation frequencies, strain amplitudes, and applied magnetic fields. The specific objectives of the present research study may be summarized as:

- Fabricating isotropic, MREs and MRF-MREs as well as MRF-Es using a reliable and repeatable process.
- Characterizing the hysteresis and viscoelastic properties of all samples with different shape factor under various mechanical and magnetic loading conditions in compression mode.
- Formulating a material constitutive model that can predict the viscoelastic properties (storage and loss moduli) of various MREs and hybrid MREs as a function of current, frequency, and strain amplitude.
- Formulating and testing a simple single degree of freedom system (SDOF) using the developed material model to investigate vibration transmissibility and the effect of applied current to shift the natural frequency of the system.

1.4 Organization of the Dissertation

The present research consists of 6 chapters.

- Chapter 1 provides pertinent literature review on the subject and outlines the scope and objective of the study.
- Chapter 2 describes the material design and methods used to fabricate different types of MRE and hybrid MRE samples. A thorough explanation of the material selection, fabrication design and procedure are provided in this chapter.
- Chapter 3 covers the experimental procedure and sample characterization. A summary of the compression test setup used for the experiment along with the applied various static and dynamic strains and current intensities are provided. The housing unit to activate the MRE and hybrid MRE samples is also discussed. The data acquired under various

mechanical and magnetic inputs is analyzed and used to understand the effects of the individual loading conditions on the viscoelastic properties of samples.

- Formulation of the phenomenological model to predict the field-dependent viscoelastic behaviour of the samples is addressed in Chapter 4. Based on the measured data from the experiment, the parameters of the proposed models are identified using a combination of the genetic algorithm and sequential quadratic programming optimization techniques. The validity of the model is further explored for predicting the hysteresis and transmissibility effects of the MR materials over the wide range of mechanical and magnetic loading conditions compared with the measured data.
- The implementation of the developed phenomenological model to formulate a single-degree-of-freedom (SDOF) spring-damper system is discussed in Chapter 5. The developed SDOF system is then utilized to predict the transmissibility and shift in natural frequency. A shaker test is also conducted to investigate the validity of the developed SDOF model.
- Chapter 6 concludes the study by summarizing the findings and shortcomings, along with providing suggestions for future works.

Chapter 2: Material Design and Fabrication Procedure

2.1 Introduction

Magnetorheological (MR) materials usually consist of magnetically permeable particles in a non-magnetic fluid or solid. In this research study, three distinct MR materials have been designed and fabricated. Theses include magnetorheological elastomer (MRE), magnetorheological fluid encapsulated with an elastomeric matrix (MRF-E), and magnetorheological fluid encapsulated with an MRE (MRF-MRE). Factors such as the choice of matrix (whether fluid or solid), the selection of ferrous particles along with their volume fraction, and the overall size of the sample are crucial factors that affect the overall field-dependent properties of MR materials. This chapter addresses the steps for each of the different sample types including their design, material selection, and manufacturing process.

2.2 Fabrication Design

As mentioned before, the main objective is to investigate the performance of the new hybrid MRF-MRE, along with an MRE and MRF-E in compression mode considering the effect of shape and shape factor. The original fabrication process included two cylindrical and two cubical samples of different height for each material, totaling 12 samples as listed in Table 2.1. However, due to limitations of the experiment's housing unit and samples themselves, four samples were unable to be tested and the list was refined as provided in Table 2.2.

Table 2.1: Original list of fabricated MR samples

Cube MRE 20mm	Cube MRE 30mm
Cylinder MRE 20mm	Cylinder MRE 30mm
Cube MRF-E 20mm	Cube MRF-E 30mm
Cylinder MRF-E 20mm	Cylinder MRF-E 30mm
Cube MRF-MRE 20mm	Cube MRF-MRE 30mm
Cylinder MRF-MRE 20mm	Cylinder MRF-MRE 30mm

Table 2.2: Reduced list of tested MRE and hybrid MRE samples

Cube MRE 20mm	Cylinder MRE 20mm
Cube MRE 30mm	Cylinder MRE 30mm
Cube MRF-MRE 30mm	Cylinder MRF-MRE 30mm
Cube MRF-E 20mm	Cylinder MRF-E 20mm

In Tables 2.1 and 2.2, Cube MRE 20 mm and Cube MRE 30 mm stand for MRE cubical samples with heights of 20 mm and 30 mm, respectively. Same terminology is applied to other samples. It is noted that in this research study, the effect of shape factor which is associated with variations in dimensions of samples has been investigated. The cylindrical samples have a diameter of 30mm, and cubical samples have a depth and width of 30 mm. This allows similar shape factor for cubical and cylindrical samples with the sample length.

The shape factor (SF) is generally defined as the ratio of the loaded area of the elastomer to the lateral surface area that is free to bulge as [42].

$$SF = \frac{compression\ loading\ area}{free\ to\ bulge\ area} \tag{2.1}$$

To clarify this, Figure 2.1 defines the dimensions of a cylindrical and rectangular sample in order to calculate their respective shape factor Eqs. (2.2) and (2.3) in Table 2.3.

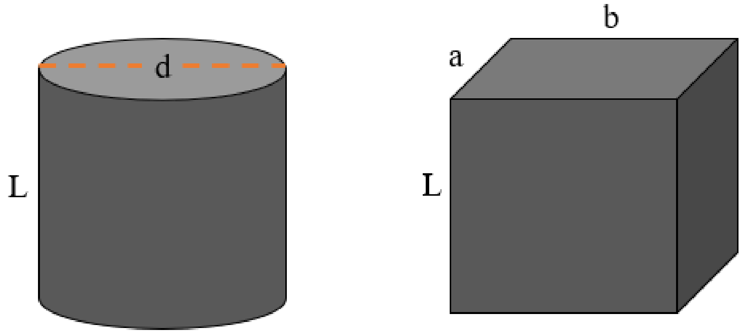

Figure 2.1: Cylindrical & cubic dimensions

$$SF_{disc} = \frac{d}{4 * L} \tag{2.2}$$

$$SF_{rectangle} = \frac{ab}{2L(a + b)} \tag{2.3}$$

Table 2.3: Shape factor for different sample aspect ratios

Sample Aspect Ratio	a (mm)	b (mm)	d (mm)	L (mm)	SF
Cylinder 20mm	-	-	30	20	0.375
Cylinder 30mm	-	-	30	30	0.25
Cube 20mm	30	30	-	20	0.375
Cube 30mm	30	30	-	30	0.25

As it can be realized from Table 2.3, the cubic and cylindrical specimens with identical heights yields similar shape factors. Moreover, it's noted that the shape factor decreases as the height increases for any given shape, attributable to the expanding bulge area.

For the hybrid MRE samples with encapsulating MR fluid, a wall thickness of 5mm on all sides was chosen based on preliminary tests. Considering the dimensions provided, a thinner wall would likely lack sufficient strength, while a thicker wall would restrict the volume available for the MR fluid to demonstrate its potential. 3D sketches (mid-section view) of the hybrid MRE samples are shown in Figure 2.2.

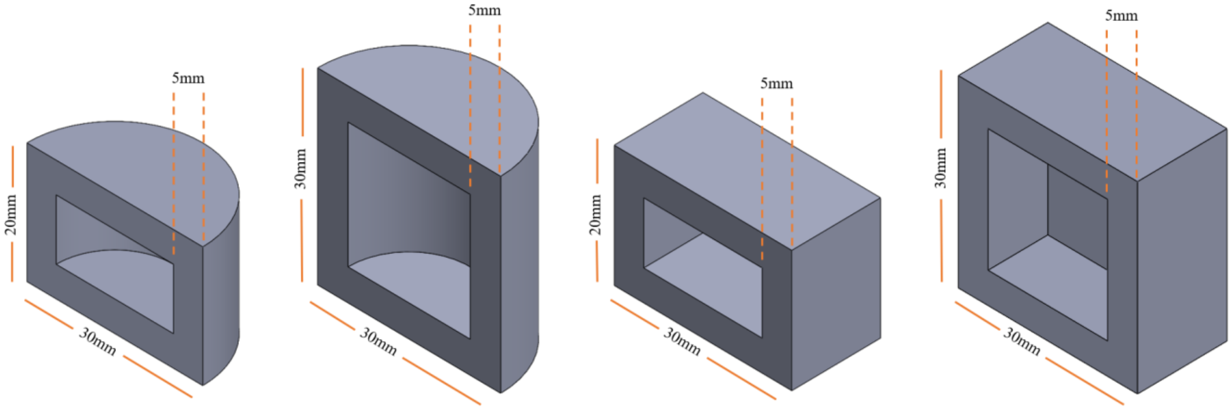

Figure 2.2: Mid-section view of hybrid MREs with encapsulated MRF in the cavity for 20mm and 30mm height samples

To fabricate the samples, unique molds were conceptualized and designed in SOLIDWORKS 2021 software as shown in Figure 2.3 & Figure 2.4 and fabricated via an FDM 3D printer (Original Prusa i3 MK3S+) with an accuracy of 100 microns.

For the hybrid MRE samples, the bottom plate includes a matching protruding cubical or cylindrical shape to form the necessary cavity for the encapsulated MR fluid, ensuring a consistent 5 mm wall thickness on all sides except the bottom. Furthermore, the caps, which seal the MR fluid within the elastomeric matrix, is fabricated using separate distinct mold with a thickness of 5 mm as shown in Figure 2.4.

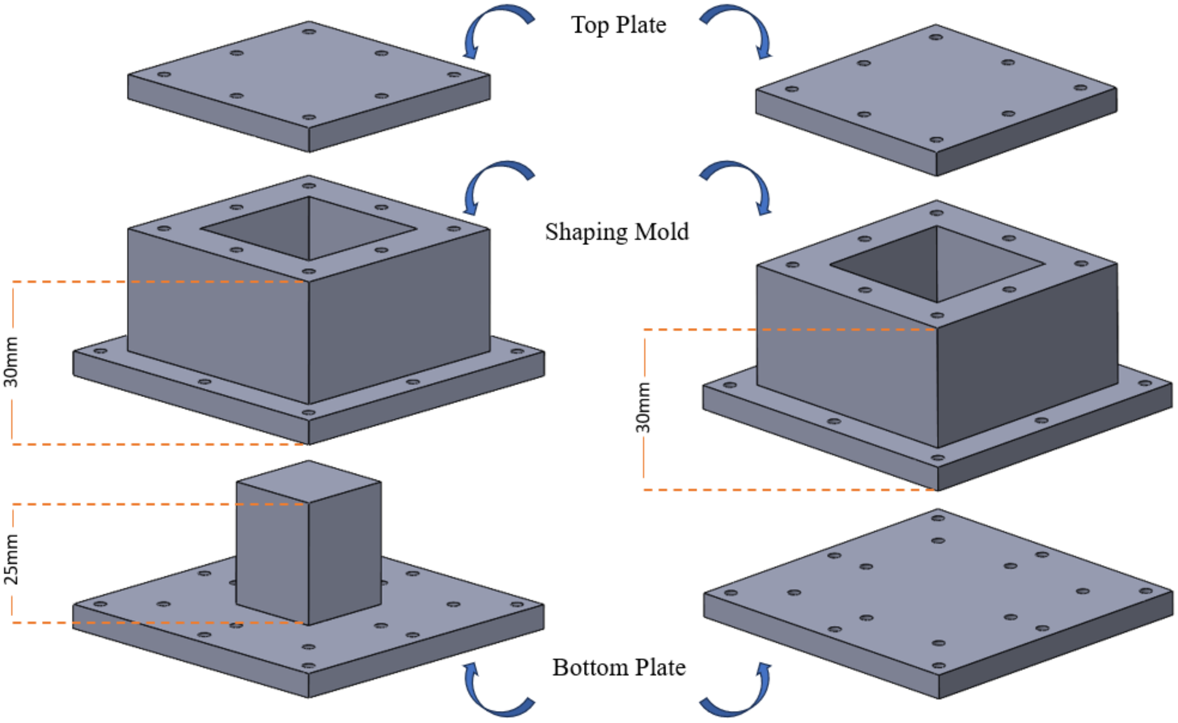

Figure 2.3: Exploded view of mold parts for cubic MRF-MRE 30mm (left) & cubic MRE 30mm (right) samples

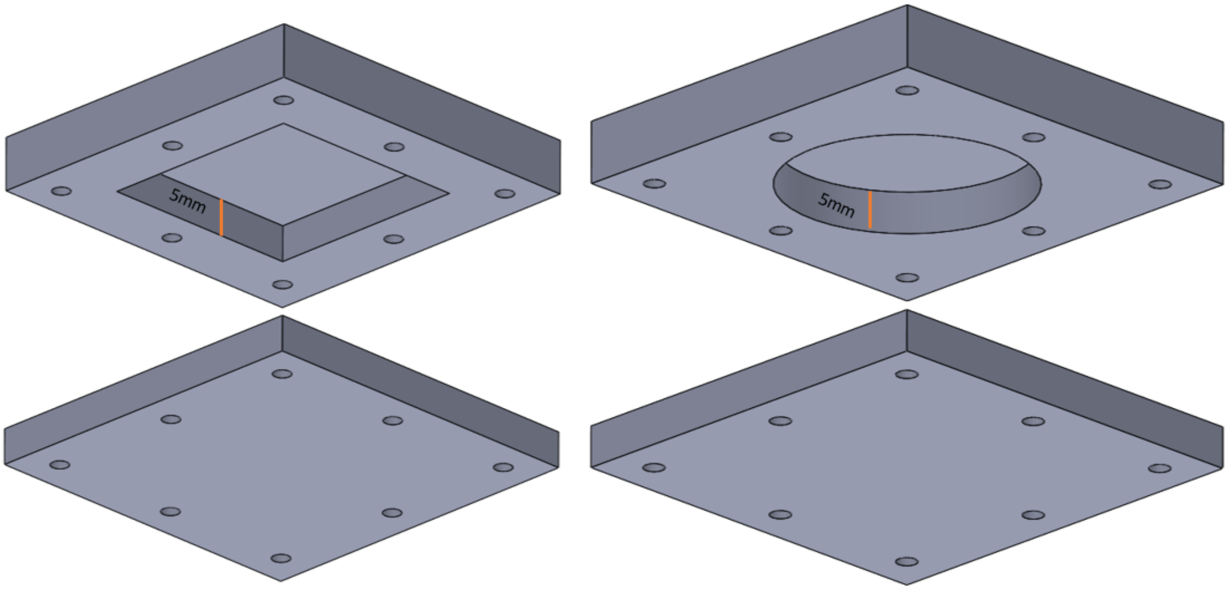

Figure 2.4: Exploded view of cubic (left) and cylindrical (right) caps for hybrid MREs

The base plate can be secured to the shaping mold using several bolts and nuts, allowing for the mixture to be poured into the cavity. Then the top plate is secured to complete the mold and give all sides of the sample a smooth and precise finish.

2.3 Material Selection

For the samples, silicone rubber was chosen to be the base elastomeric matrix. The silicone rubber Ecoflex 00-30, named for its Shore hardness of 00-30, was chosen as matrix and was obtained from Smooth-On Inc [43]. The product consists of the rubber component (A) and the catalyst component (B): are then mixed together with the ratio of A1:B1. For the magnetic particles, carbonyl iron was chosen due to its high permeability and low coercivity. They are acquired from BASF Corporation [44]. For the samples that require MR fluid, MRF-132DG from lord corporation [45] was selected. The fluid consists of a base hydrocarbon silicone oil mixed with carbonyl iron particles. Optimal volume fraction is estimated to be around the 20-25% range [3], therefore, the volume fraction of the MRE and MRF were chosen to be 20% to keep samples as soft and light weight as possible while keeping MR effect at an optimum level. It is noted that the volume fraction of magnetic particles is the same for all samples.

2.4 Fabrication Procedure

To begin the fabrication, the desired amount of each component (Part A and Part B of the silicone rubber) was measured and prepared in separate beakers. Then, the two parts of silicone rubber were mixed thoroughly in a glad beaker with a wooden stick. For MREs and hybrid MREs a measured amount of carbonyl iron particles (CIP-SQ, BASF) was then added to the uncured liquid compound. The calculation for the required mass of CIP for a volume fraction of 20% considering 60g of the Ecoflex 00-30 matrix (Part A: 30g, Part B: 30g) are provided below:

$$Ecoflex\ 00-30 \begin{cases} Part\ A, & 30\ g \\ Part\ B, & 30\ g \end{cases}$$

$$V_{Silicon} = \frac{m_{silicon}}{\rho_{silicon}} = \frac{60g}{\frac{1.07g}{cm^3}} = 56.0748\ cm^3 \tag{2.4}$$

$$Volume\ Fraction = \frac{V_{CIP}}{V_{Silicon} + V_{CIP}} = \frac{\frac{m_{CIP}}{\rho_{CIP}}}{V_{Silicon} + \frac{m_{CIP}}{\rho_{CIP}}}$$

$$\frac{20}{100} = \frac{\frac{m_{CIP}}{7.874\frac{g}{cm^3}}}{56.0748\ cm^3 + \frac{m_{CIP}}{7.874\frac{g}{cm^3}}}$$

$$m_{CIP} = 110.3177g$$

It is to be noted that the masses and volumes for both the carbonyl iron particles and silicone may not reflect the actual amount in any of the samples. These measurements were conducted to create a large amount of the mixture to be poured for multiple samples to make the manufacturing process faster. For the MRF-E samples, since the MR fluid was encapsulated into only the silicone elastomer, the measuring and mixing of the CIP particles would not be needed.

Once the required measurements were roughly mixed by hand, the mixture was then placed in a vacuum mixer (Thinky: ARV-200, Figure 2.5) at a controlled vacuum pressure of 27 in-Hg (91.4 kPa) and angular speed of 2000 rpm, for a duration of 40s. This procedure ensures a uniform and smooth mixture, eliminating any tiny air bubbles trapped inside or on the surface.

Figure 2.5: Thinky ARV-2000 Vacuum Mixer

Finally, the fabricated 3D printed molds (see Figure 2.6 and Figure 2.7 for cubic MRE and MRF-MRE molds for samples with 30mm height as an example) are initially sprayed with a release agent (Ease Release 200, Smooth-On-Inc) before pouring the prepared vacuumed mixture into the related molds. Once poured the molds are sealed and allowed to cure at room temperature for 12 hours and subsequently removed.

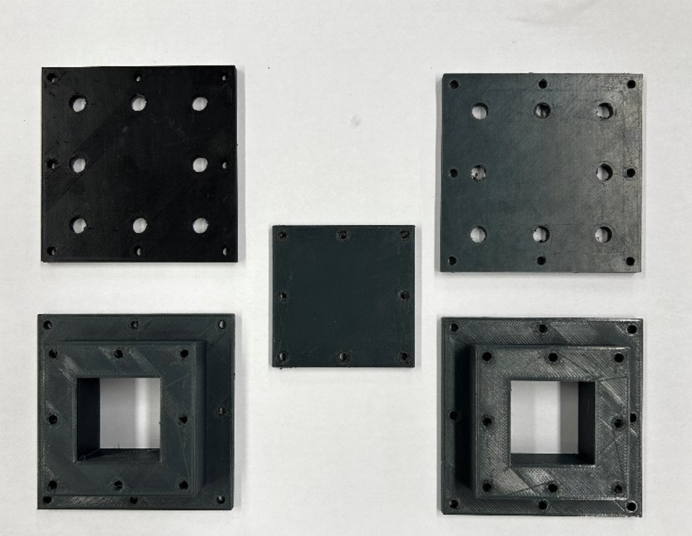

Figure 2.6: 3D-printed molds for cubic MRE 30mm sample

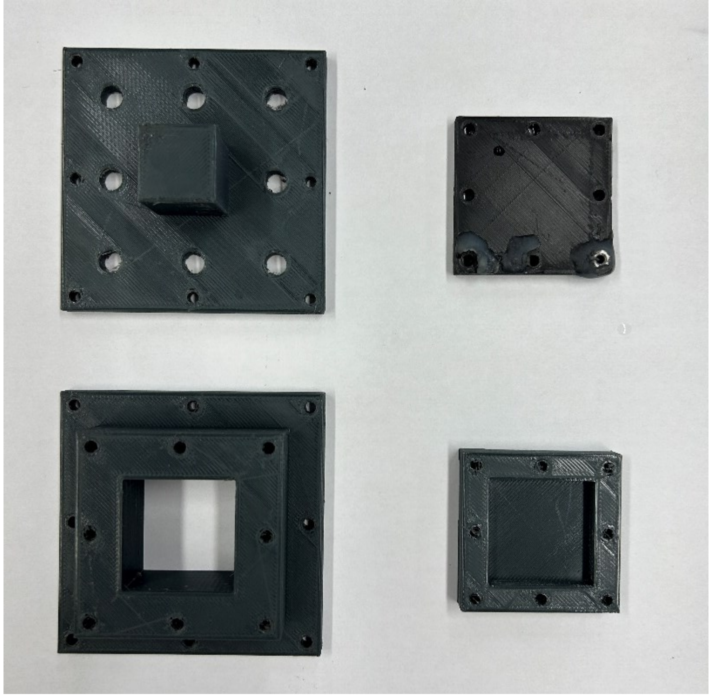

Figure 2.7: 3D-printed molds for cubic MRF-MRE 30mm sample

It is noted that for the MRF-MRE and MRF-E samples the fabrication procedure continues by pouring the magnetorheological fluid (LORD MRF-132DG) into the cured pure silicone or MRE cavities. Once filled, the relative caps are glued on top using (Sil-Poxy, Smooth-On Inc.) to seal the MR fluid within the sample. The fabrication process for the hybrid MRE samples is summarized in Figure 2.8.

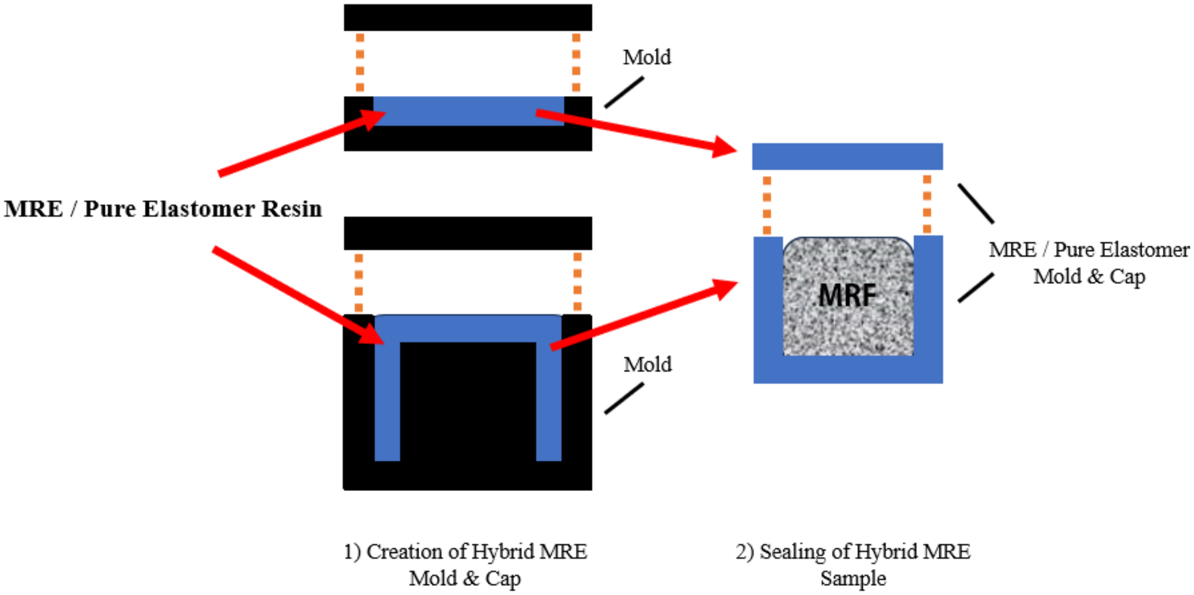

Figure 2.8: Fabrication process of hybrid MREs

The finalized fabricated MRE samples are shown in Figure 2.9 as an example.

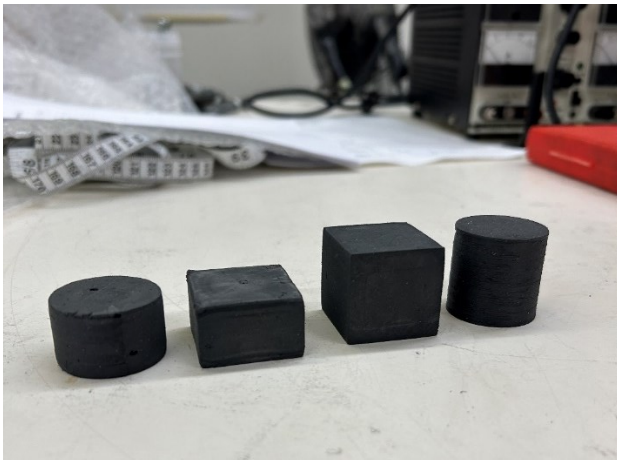

Figure 2.9: MRE samples: Cylinder 20mm, Cube 20mm, Cube 30mm, Cylinder 30mm (left to right)

Chapter 3: Experimental Characterization of MRE and Hybrid MRE-MRF Materials

3.1 Introduction

As mentioned in Chapter 1, the characterization of MREs in shear mode has been widely studied, while there are relatively limited studies on the compression mode characterization of MREs. This is partially due to the complexities associated with the experimental test setup and compensation of the magnetic force in characterization for compression mode. Also, as discussed, the compression mode characterization of hybrid MREs with various shapes (ex. cylinder and cube) and shape factors (aspect ratios) under a wide range of loading conditions has been scarcely explored. This chapter addresses the characterization for MREs, MRF-Es and MRF-MREs in compression mode under an expansive range of strain amplitudes (2.5% to 15%), frequencies (0.088 Hz to 10 Hz) and applied current (0 to 8A) considering a static pre-strain of 40%. A test setup including an MTS machine and electromagnet cell to activate MREs is designed for experimentation to assess the magneto-mechanical characteristics of the MR samples. Subsequent analysis entails extracting hysteresis stress-strain curves and their corresponding dynamic properties, including elastic modulus (E') and loss modulus (E''), from the acquired data. The results are subsequently discussed, and explanations are provided for the observed response behaviour.

3.2 Experimental Test Setup

In order to characterize MR materials there is a need of providing constant magnetic fields to the fabricated samples during the tests. To facilitate this requirement, a housing unit or electromagnet cell designed by Martins et al. [46] for a MRE seat cushion was used. The magnetic cell was given to Concordia University by National Research Council (NRC) of Canada. The unit was initially designed to be integrated within a seat cushion for closed loop semi-active seat vibration control in helicopters. However, following preliminary tests, it was determined that the unit would serve a more beneficial purpose by being reformatted for the characterization of MREs and open loop vibration characterization.

The unit consists of an upper and bottom section, as shown in Figure 3.1. The main features include top and bottom steel cores within aluminum cases and an embedded electromagnetic coil to activate the MRE samples. The steel cores are made entirely of AISI 1018 steel, which effectively guides the magnetic field generated by the electromagnetic coil to form a closed magnetic circuit path due to the steel's high magnetic permeability. The bottom aluminum case houses two clamps that secure the coil in place. A guiding system composed of two shafts and the corresponding ball bearings fits in the aluminum cases to ensure that the top and bottom pieces are aligned during the loading displacement [46].

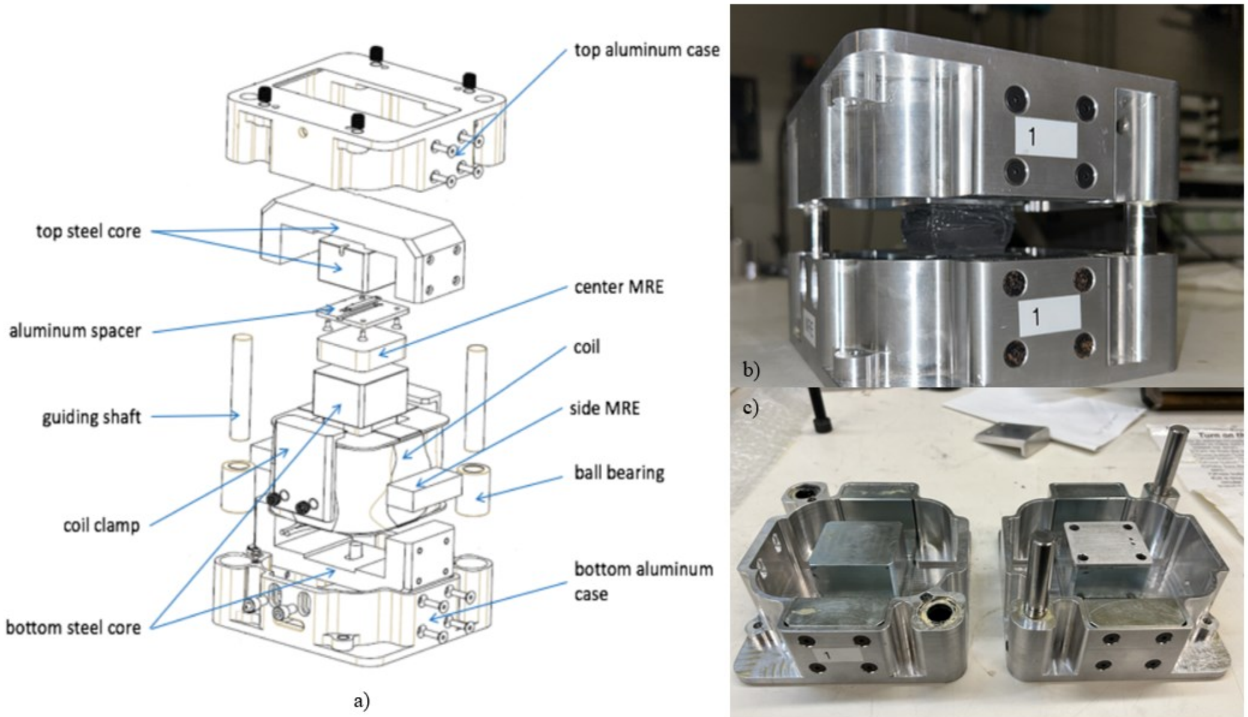

Figure 3.1: Housing Unit a) Schematic exploded view [46] b) Assembled with sample (No Coil) c) Bottom half (right) Top half (left)

The electromagnet coil is connected to a DC power supply (Volteq HY10416EX) to generate the magnetic field in the MRE region. It is noted that due to the closed nature of the cell, measuring the magnetic field intensity directly was not possible. In total, the samples are tested under five different currents, starting from 0A and then increasing in intervals of two until 8A (I=0, 2, 4, 6, 8 A). The MR samples are carefully sandwiched between the bottom and top steel cores in the unit cell. The unit cell was subsequently integrated into a servo-hydraulic material test system (MTS) 858 frame for uniaxial compression where the bottom case was secured in place by two wedge grips and the upper section was clamped to a fixed beam via a 9kN load cell. Figure 3.2 shows the experimental test rig which includes the MTS machine with the unit cell to be tested. The actuation is applied from the bottom of the frame by a hydraulic actuator and the displacement is measured through a Linear Variable Differential Transformer (LVDT) integrated within the actuator. The output force of the MR samples was measured via the loadcell. For safety reasons, a thermocouple was installed on the coil surface to monitor its surface temperature, and a large size fan was used, to ensure that the coil surface temperature remained near 40°C±5°C. By using this setup, a series of compression tests under varying excitation frequency, displacement amplitude and applied current were subsequently performed on the eight samples. It is noted that the cyclic deformation was performed after applying a large static pre-strain of 40%.

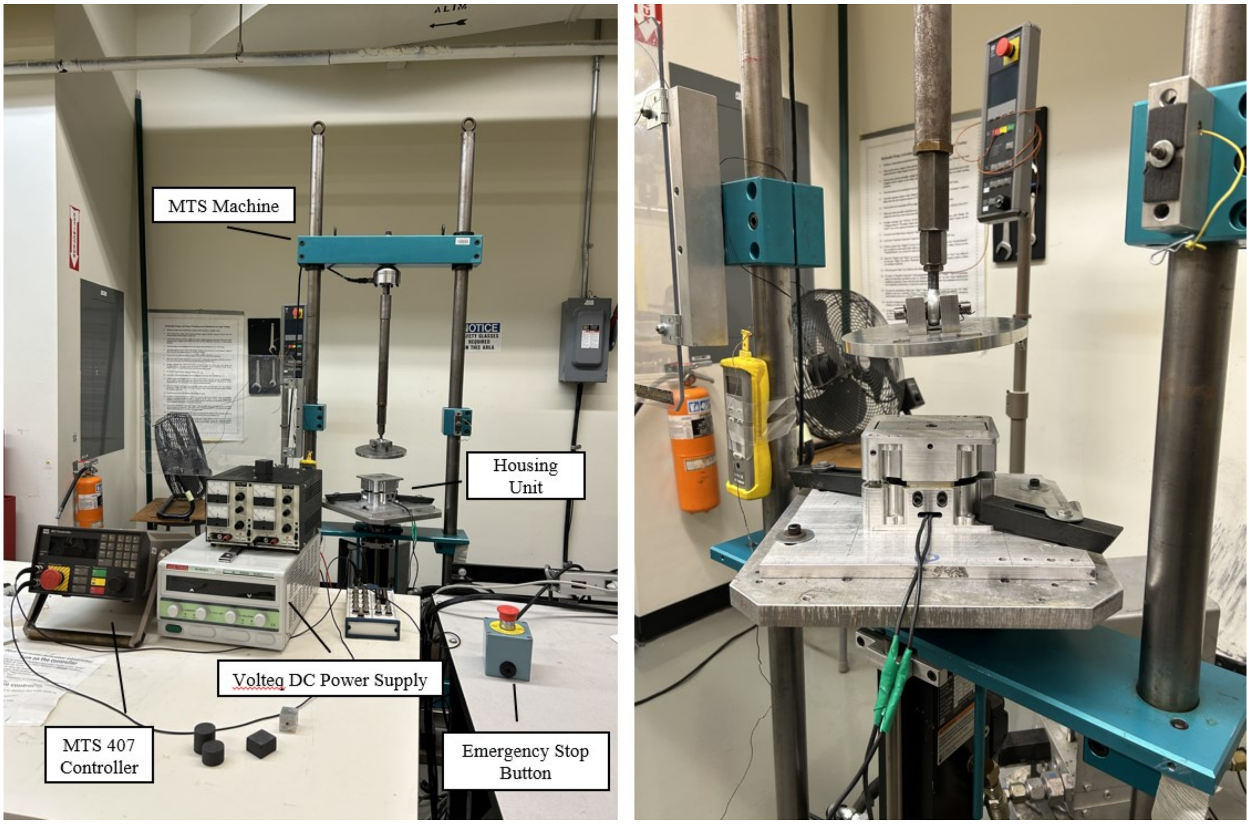

Figure 3.2: Experiment test setup

The loading frequencies and strain amplitudes are varied as f = 0.088, 0.5, 1, 2.5, 5, 7.5, 10 Hz and ε_0=2.5%, 5%, 10%, 15%, respectively. It is to be noted that for the quasi-static measurements

(0.088 Hz and 0.5 Hz), only a strain amplitude of 15% was applied. The force and displacement signals were acquired during each measurement in the LabView platform through a National Instruments (NI) Data Acquisition (DAQ) board, with a sampling rate of ranging from 50Hz to 2500Hz depending on the loading frequency. A total of 110 tests were conducted on each sample. The steady state force-displacement data for all samples are then extracted which are subsequently analyzed and discussed in the next section.

3.3 Analysis of Experimental Data

The steady-state force-displacement response of the MR samples was acquired and averaged at minimum over three consecutive oscillation cycles and then processed via a low-pass filter. The measured compression mode force data acquired during experimental testing comprises of two components: the magnetic force developed by the electromagnet's magnetic poles and the viscoelastic force attributed to the compression loading of the MR samples. Considering that the viscoelastic properties of the samples are desired, the magnitude of the magnetic force must be removed through the compensation procedure [33]. As written in Equation 3.1, the compensation procedure is implemented by initially measuring the magnetic force of the electromagnet (F_{mg}) which is subsequently subtracted from the total measured force (F_{Total}) to obtain the field dependent magneto-viscoelastic force (F_{MRE}) attributed to deformation of the MR samples [33]. The resulting viscoelastic force and displacement data were subsequently used to obtain stress-strain characteristics of the samples under different mechanical and magnetic loading conditions.

$$F_{MRE}(f, I, \varepsilon_0) = F_{Total}(f, I, \varepsilon_0) - F_{mg}(f, I, \varepsilon_0) \tag{3.1}$$

The magnetic force is measured by setting the gap length between the top and bottom sections of the housing cell equal to the sample’s compressed height at a pre-strain of 40%. For instance, a sample with a height of 20 mm at 40% pre-strain must be compressed by 8 mm, resulting in a gap length of 12 mm. Similarly, a sample with a height of 30 mm at 40% pre-strain would have a gap length of 18 mm.

In the absence of the MRE samples and at the defined gap length, the magnetic force is measured at the same loading conditions as the experimental tests. Results for the total, magnetic, and viscoelastic force-displacement response for a Cube 30 mm MRF-MRE sample under an excitation frequency and strain amplitude of 1 Hz and 10% is shown in Figure 3.3 as an example.

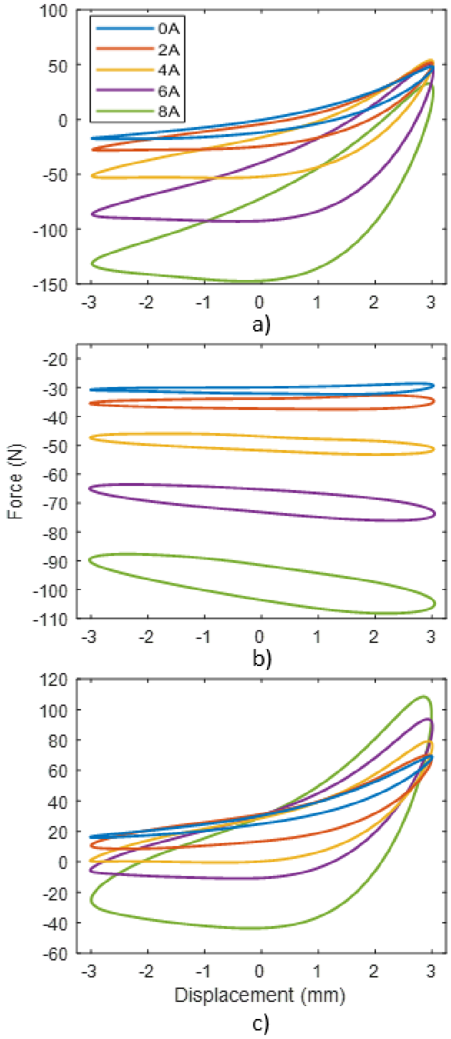

Figure 3.3: Force data magnetic force compensation for Cube MRF-MRE 30mm at 1 Hz and strain amplitude of 10% (a) Total Force (b) Magnetic Force (c) Compensated Viscoelastic Force

The significance of magnetic force compensation is demonstrated in Figure 3.3. In Figure 3.3(a), a majority of the total force is subjected to negative force (tension), specifically, during the unloading of the specimen which is due to the included magnetic force. In Figure 3.3(b), the effects of magnetic force are shown under varying current. As the current increases, the magnetic force becomes much stronger. It is note at current above 4A, the magnetic force begins to have a noticeable slope as the strain nears its maximum. Due to the large loading strain amplitude, the gap between the upper and lower sections of the electromagnet cell become closer and thereby, the magnetic field becomes stronger at these points. Figure 3.3(c) shows the compensated force-displacement results. As it can be realized in Figure 3.3(c), by increasing the current from 0 to 8A both the major slope (representing stiffness) and the area enclosed (representing damping) of the force-displacement hysteresis loop increases.

To further assess the dynamic properties of the MR samples in the compression mode, the elastic modulus (E'), and loss modulus (E'') were evaluated through the analysis of the resulting measured compensated force-displacement data. Considering the nonlinearities of compression mode, the first harmonic of Fourier series approximation was chosen as the equivalent storage and loss moduli, as prescribed in the standardized method ASTM D5992-96 [47]. Although it has been reported that at high strain amplitudes, the first harmonics often cannot accurately capture rich nonlinearities, the method is still widely considered adequate for providing an equivalent measure of viscoelastic moduli for nonlinear responses [48]. It is also worth mentioning that commercial rheometers and dynamic mechanical analyzers provide materials' characterizations on the basis of the first harmonic elastic and loss moduli [49]. Assuming a sinusoidal strain input $\varepsilon(t) = \varepsilon_0 \sin(2\pi f t)$, the nonlinear stress response can be represented by a Fourier series in the following equation [48]:

$$\sigma(t; f, I, \varepsilon_0) = \sigma_0 + \varepsilon_0 \sum_{n=1}^{m} \{E_n'(f, I, \varepsilon_0) \sin 2\pi n f t + E_n''(f, I, \varepsilon_0) \cos 2\pi n f t\} \tag{3.2}$$

where $E_n'(f, I, \varepsilon_0)$ and $E_n''(f, I, \varepsilon_0)$ denote n th-harmonic elastic and loss moduli, respectively, as functions of frequency (*f*), strain amplitude (ε_0) and applied current (I). σ_0 represents the nonzero mean stress attributed to the static preload and m denotes the maximum chosen order considered in the Fourier equation [49]. Using the MATLAB curve fitting tool and the Fourier series (Equation 3.2) truncated up to an order of $n = 4$, the moduli at each harmonic are obtained. As an example, Figure 3.4 compares the measured stress response and the curved fitted approximation using Fourier series for the Cylinder MRF-E 20mm sample at an excitation frequency and strain amplitude of 1 Hz and 10%, respectively, at an applied current of 6A.

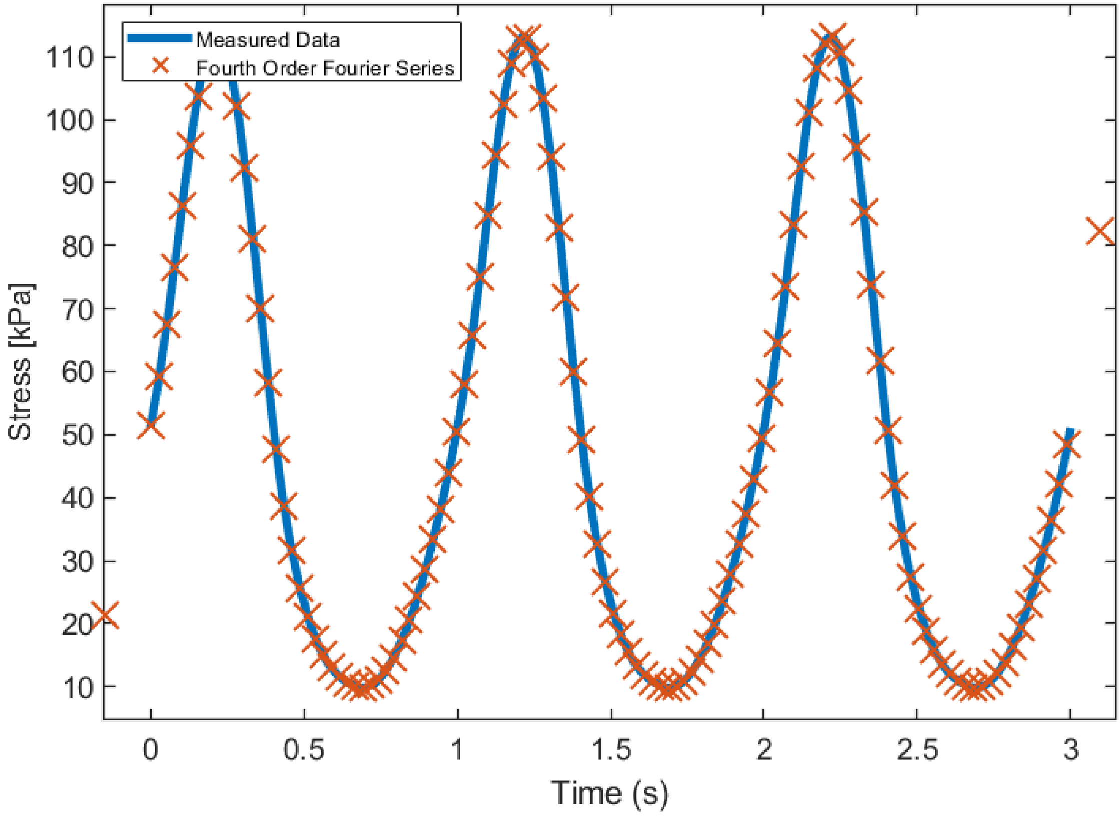

Figure 3.4: Fourth order Fourier series curve fitting to stress vs. time measured data – Cylinder MRF-E 20mm (f=1 Hz, ε_0=10%, I=6 A)

Table 3.1 provides the identified coefficients values of the fourth order Fourier series from the example shown in Figure 3.4.

Table 3.1: Results of fourth order Fourier series – Cylinder MRF-E 20mm (f=1 Hz, ε_0=10%, I=6 A)

Parameter	**Value (Pa)**
σ_0	4.86×10^4
E_1'	4.6×10^5
E_2'	4.36×10^4
E_3'	-3.47×10^4
E_4'	-2.75×10^3
E_1''	1.49×10^5
E_2''	-1.19×10^5
E_3''	-1.05×10^4
E_4''	4.05×10^3

Using the values of the first harmonics E_1' and E_1'', the hysteresis loop based on first harmonic approximation and measured stress-strain hysteresis are compared in Figure 3.5. E_1' and E_1'' can also be obtained by the following set of equations using the approximate symmetric hysteresis [50].

$$E_1' = \frac{\sigma|_{\varepsilon_{max}} - \sigma|_{\varepsilon_{min}}}{\varepsilon_{max} - \varepsilon_{min}} \tag{3.3}$$

$$E_1'' = \frac{Area\ of\ Ellipse}{\pi \sigma_{max} \varepsilon_{max}} \tag{3.4}$$

where σ_{max}, $\sigma_{\varepsilon_{max}}$ are the maximum stress, and stress at maximum strain (ε_{max}). $\sigma_{\varepsilon_{min}}$ refers to stress at minimum strain (ε_{min}).

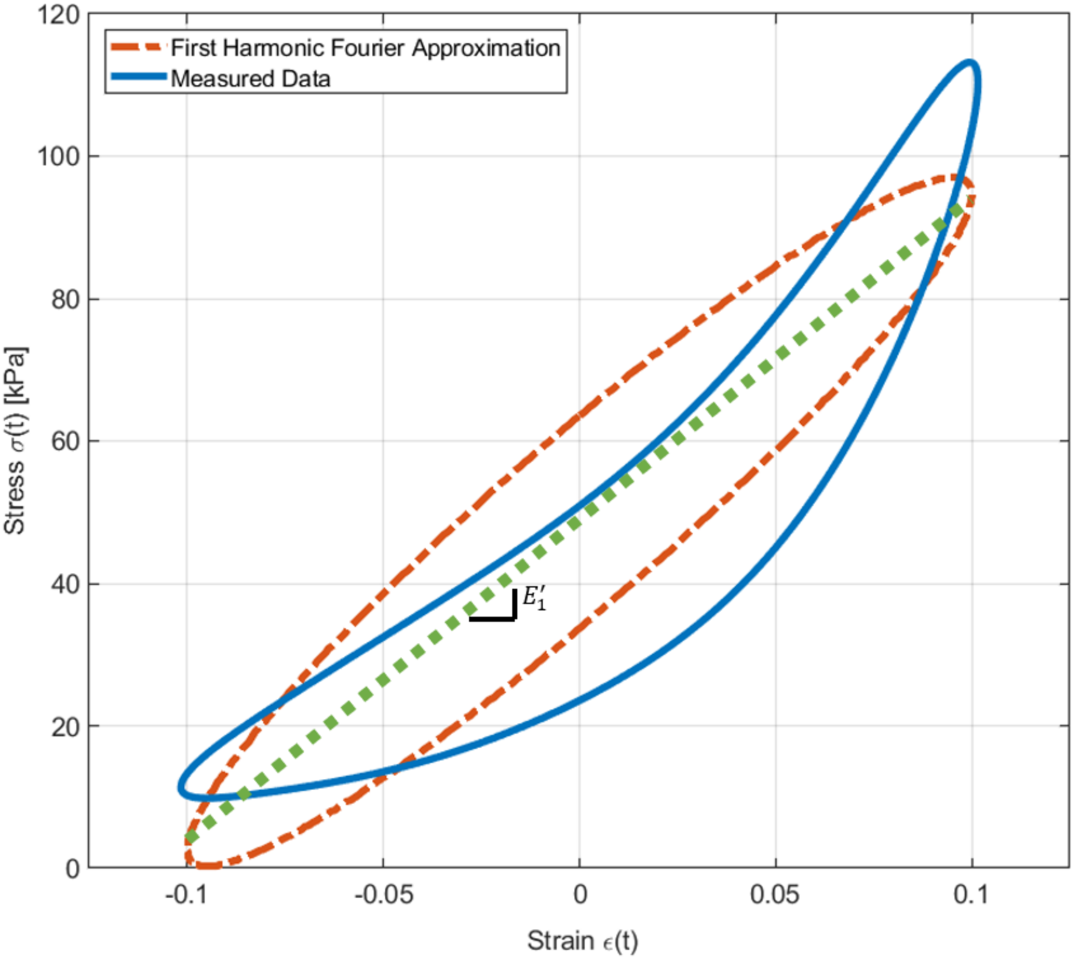

Figure 3.5: Comparison of measured data with first harmonic approximation – Cylinder MRF-E 20mm (f=1 Hz. ε_0=10%, I=6 A)

Using the first harmonic approach, as described above, the effective storage and loss moduli for the nonlinear compressive stress-strain hysteresis have been extracted for all test configurations.

3.4 Stress-strain Hysteresis Loop Viscoelastic Responses

As mentioned in sections 3.1 & 3.2, for dynamic characterization, total number of 110 tests were carried out on each sample, containing 20% volume fraction iron particles and at a pre-strain of 40%, in simple compression mode to capture stress-strain hysteresis loops under various harmonic excitations. The effects of shape factor, shape, frequency rate, amplitude and current on the hysteresis loops are investigated and the results are presented in the following subsection.

3.4.1 Effect of the Shape Factor

Figure 3.6 illustrates the effect of shape factor (SF) on the stress-strain characteristics of different MRE samples, subject to peak strain of 15%, respectively, at a frequency of 5 Hz in the presence of an applied current of 4A, as an example. The results demonstrate the effects of SF on both the equivalent stiffness and the effective damping properties of the MRE samples. Increasing the SF from 0.25 for Cube MRE 30 mm to 0.375 for Cube MRE 20 mm results in a dramatic increase in the slope of the major axis of the hysteresis curves, along with a slight increase in area. Thereby, increasing the effective stiffness and yielding a much higher peak stress during compression. This behaviour has also been observed for cylindrical MRE samples. Results generally show that increasing the shape factor induces a strain-stiffening effect, as the hysteresis loop response becomes highly nonlinear.

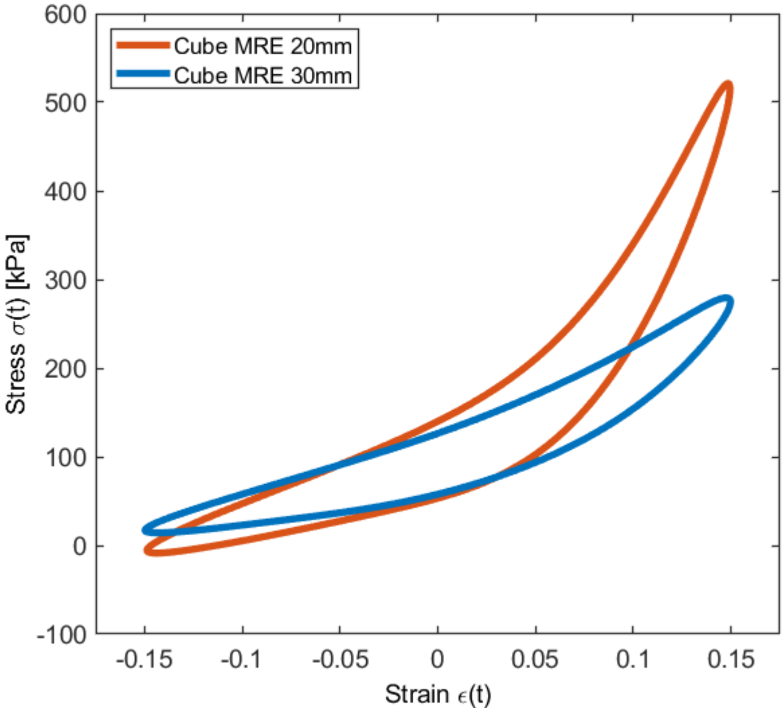

Figure 3.6: Effects of height on the stress-strain characteristics of cubic MRE samples (f=5 Hz. ε_0=15%, I=4 A)

3.4.2 Effects of Shape (Cubic and Cylindrical)

Effect of shape of the sample on the hysteresis stress-strain response has also been investigated for MRE and hybrid MRE samples. Figure 3.7 shows the results for cubic and cylindrical MRE, MRF-E and MRF-MRE samples with equal heights (same shape factor) under excitation frequency, strain amplitude and applied current of 5 Hz, 15% and 4A, respectively.

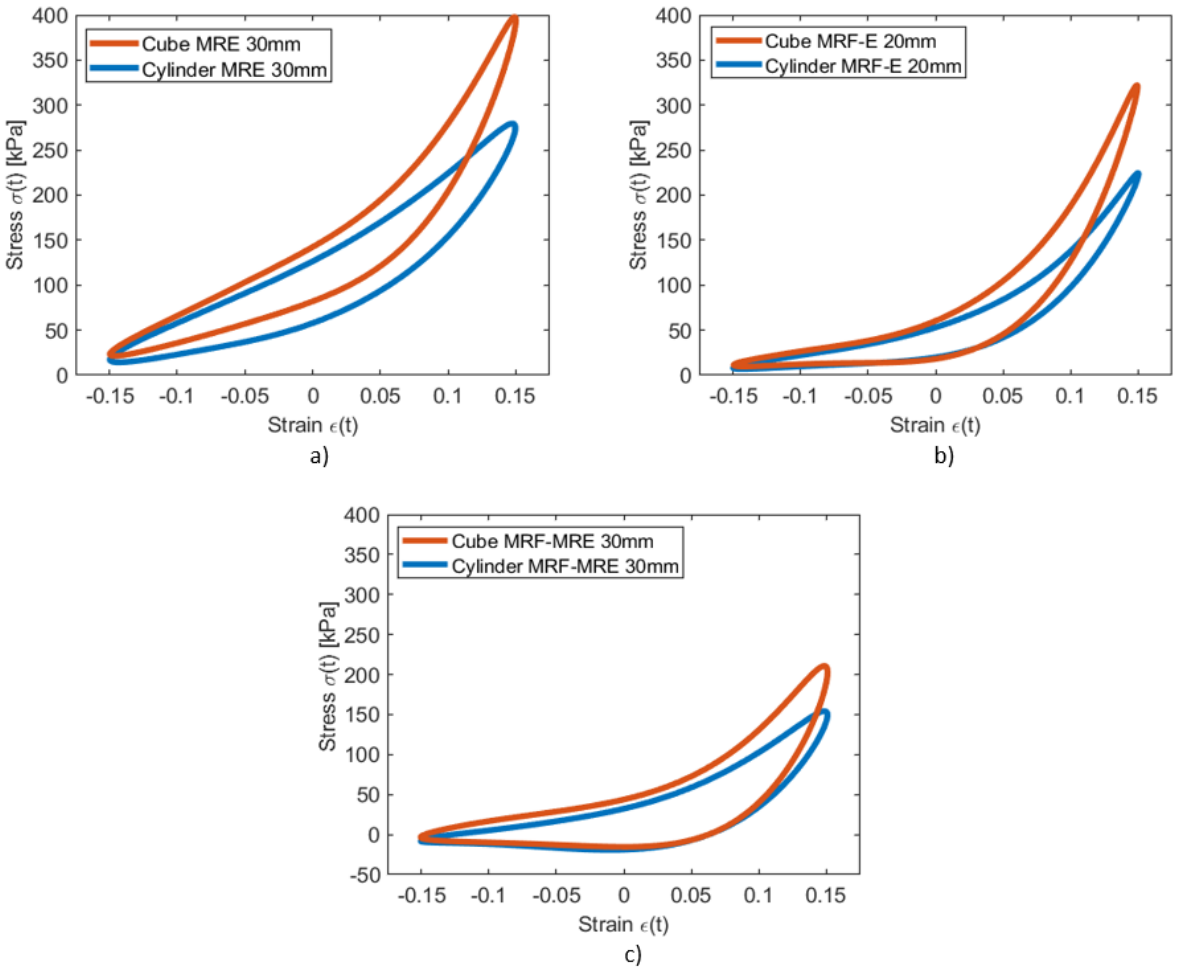

a)

b)

c)

Figure 3.7: Effects of shape on the stress-strain characteristics of 3 different sample types (f=5 Hz. ε_0=15%, I=4 A) (a) MRE 30mm samples (b) MRF-E 20mm samples (c) MRF-MRE 30mm samples

Examination of results reveal that cubic MREs have a higher stiffness as compared to cylindrical MREs. Similar trends were also observed for MRF-Es and MRF-MREs. This is partly due to the larger loading area of the cubic samples which cause higher amounts of friction during expansion of the specimen [33]. Moreover, the peak stress in cubic samples exceeds that of cylindrical samples regardless of their type. Comparing the effects of shape for all sample types, it seems the hybrid MRF-MREs are the least affected by the shape of the sample, which could be due to their softness. Additionally, MRE samples exhibit a higher peak stress compared with MRF-E samples, and MRF-E samples have a higher peak stress compared with MRF-MRE samples.

3.4.3 Effects of Excitation Frequency

Figure 3.8 illustrates the effect of excitation frequency on the stress-strain hysteresis loop characteristics of different MR samples, subject to peak strain of 10%, respectively, in the presence of a current of 0A and 4A. Results generally show that the excitation frequency has more pronounced effect on the stiffness and damping characteristics of the MR samples in the absence of the applied magnetic field. This is partly because, at lower current levels, the MR samples have not yet stiffened due to the applied current. Thus, increasing the frequency leads to a rate-stiffening effect in the MR samples, primarily due to the rubber-like characteristics of the matrix in the fabricated MR samples.

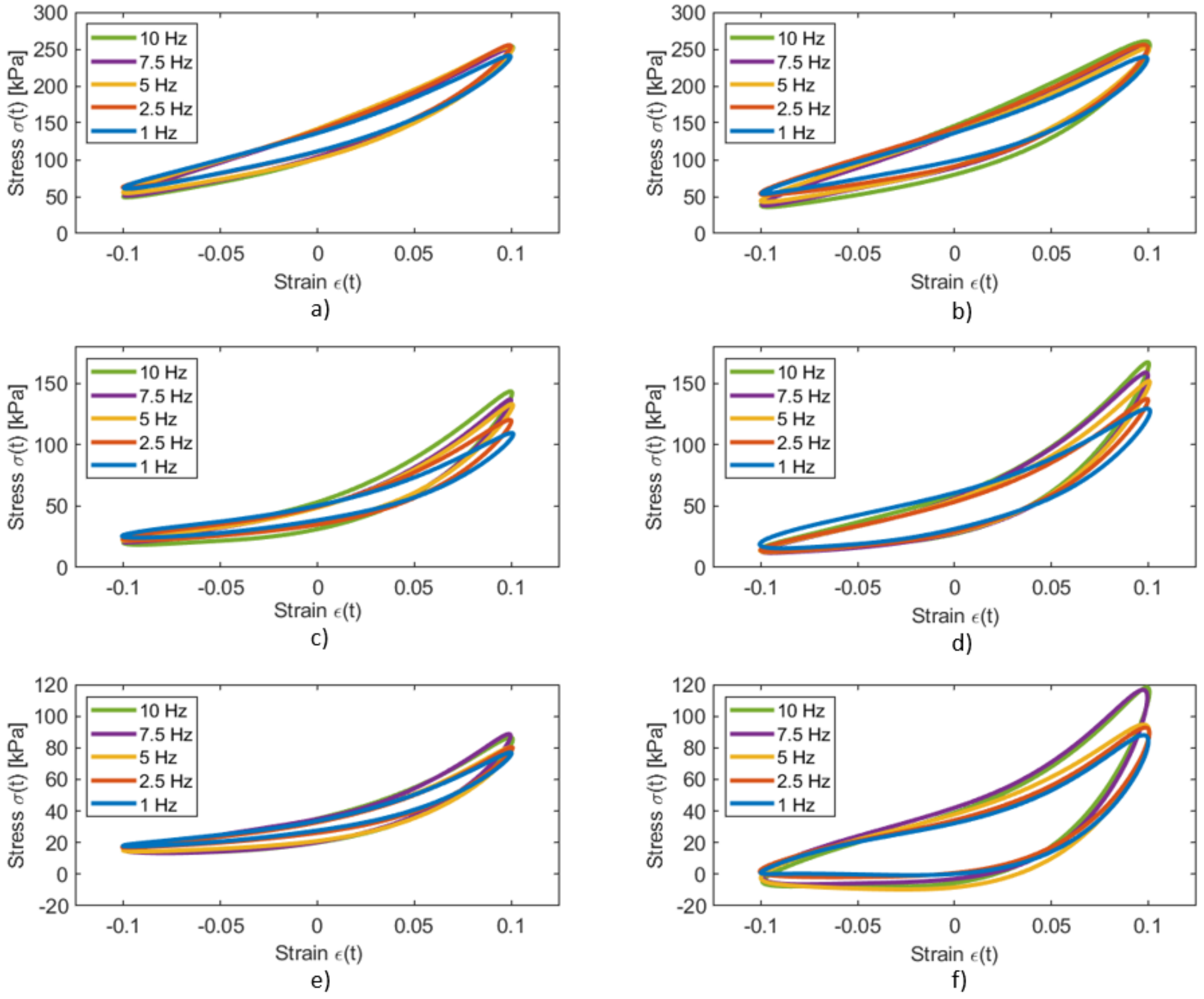

Figure 3.8: Measured hysteresis of 3 different sample types with 10% strain amplitude (a) Cube MRE 30mm 0A (b) Cube MRE 30mm 4A (c) Cube MRF-E 20mm 0A (d) Cube MRF-E 20mm 4A (e) Cube MRF-MRE 0A (f) Cube MRF-MRE 4A

Observations also indicate an increase in the equivalent stiffness due to the increase in major slope of hysteresis loop with increasing frequency, suggesting strain rate stiffening effect typically observed in rubbery material. Even though the results presented are at a strain amplitude of 10%, relatively similar trends were also observed at other strain amplitudes. Furthermore, the peak stress during loading increases with the increase in strain rate. These effects, however, start to diminish when excitation frequencies reach above the 7.5 Hz to 10 Hz range. By increasing the applied current, the effect of strain rate stiffening effect is reduced as the samples have already stiffened due to the applied current. Differences between the sample types seem to be minimal, as the increase in peak stress are consistent with each other. Further examination of results in Figure 3.8 also reveals that MRF-MRE sample shows substantial increase in damping level upon application of the applied current.

3.4.4 Effects of Strain Amplitude

Figure 3.9 illustrates the effect of strain amplitude on the stress-strain hysteresis loop characteristics of different MR samples, subjected to an excitation frequency of 2.5 Hz, respectively, in the presence of an applied current of 0A and 6A.

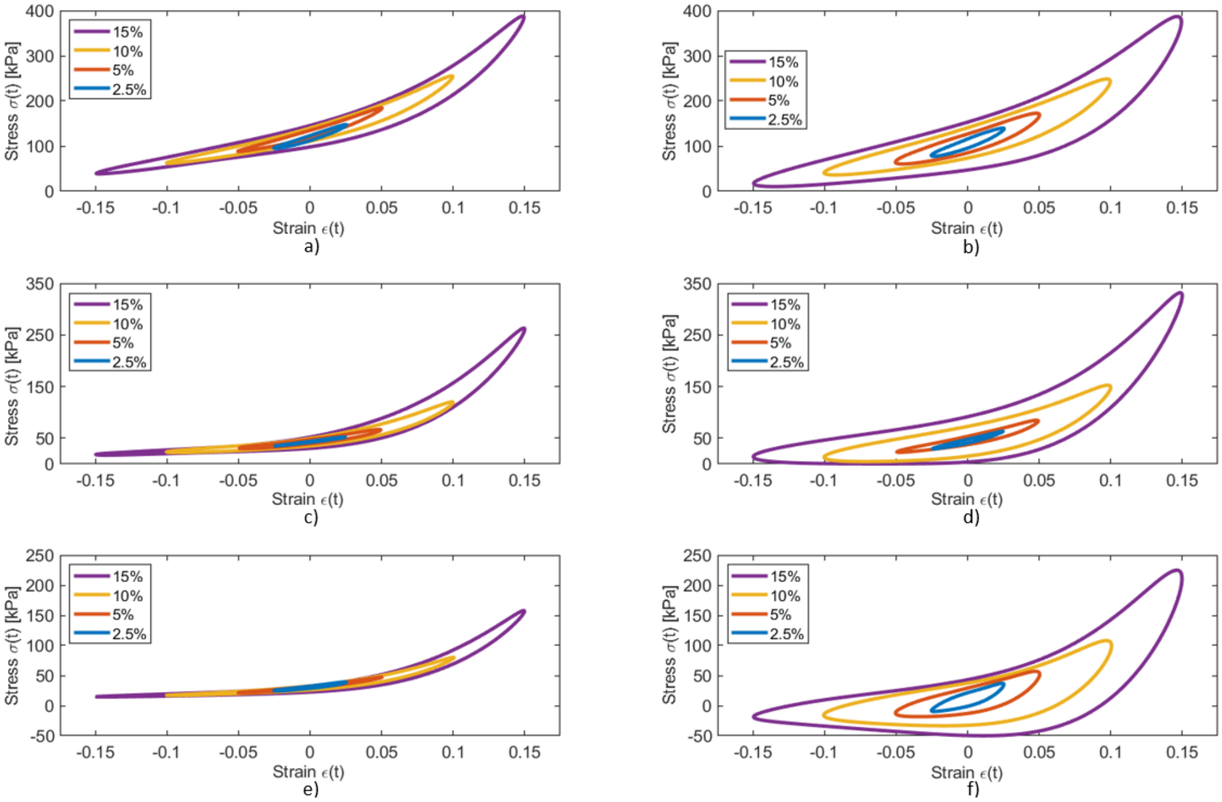

Figure 3.9: Measured hysteresis of 3 different sample types at 2.5 Hz (a) Cube MRE 30mm 0A (b) Cube MRE 30mm 6A (c) Cube MRF-E 20mm 0A (d) Cube MRF-E 20mm 6A (e) Cube MRF-MRE 0A (f) Cube MRF-MRE 6A

It can be realized that irrespective of the type of MR samples, results show linear viscoelastic characteristics behaviour (pure ellipse shape stress-strain characteristics) at relatively lower level of strain amplitude (i.e., 2.5%). This linear viscoelastic behaviour of MR samples is also more pronounced in the absence of the applied magnetic field. Moreover, the hysteresis shape gradually changes from nearly elliptical shape at low strain amplitudes (below 5%) to non-elliptical nonlinear hysteresis shape at high strain amplitudes which is characteristic of nonlinear viscoelastic behaviour. Results show that by increasing the strain amplitude above nearly 5%, the equivalent stiffness reduces (major axis rotates in clockwise direction) which is known as strain softening effect. This phenomenon is also observed in typical filled rubbery, where the viscoelastic storage modulus decreases with increasing strain amplitude beyond a certain limit, known as the Payne effect [51]. Examination of results also show that strain softening effect is more pronounced under application of current and for the hybrid MRF-MRE sample.

3.4.5 Effects of Magnetic Field Intensity

Figure 3.10 illustrates the effect of the applied current on the stress-strain characteristics of different MR samples, subject to an excitation frequency of 1 Hz, and at a strain amplitude of 15%. Results clearly show that the applied magnetic field has substantial effect on dynamic response regardless of the type of MR samples.

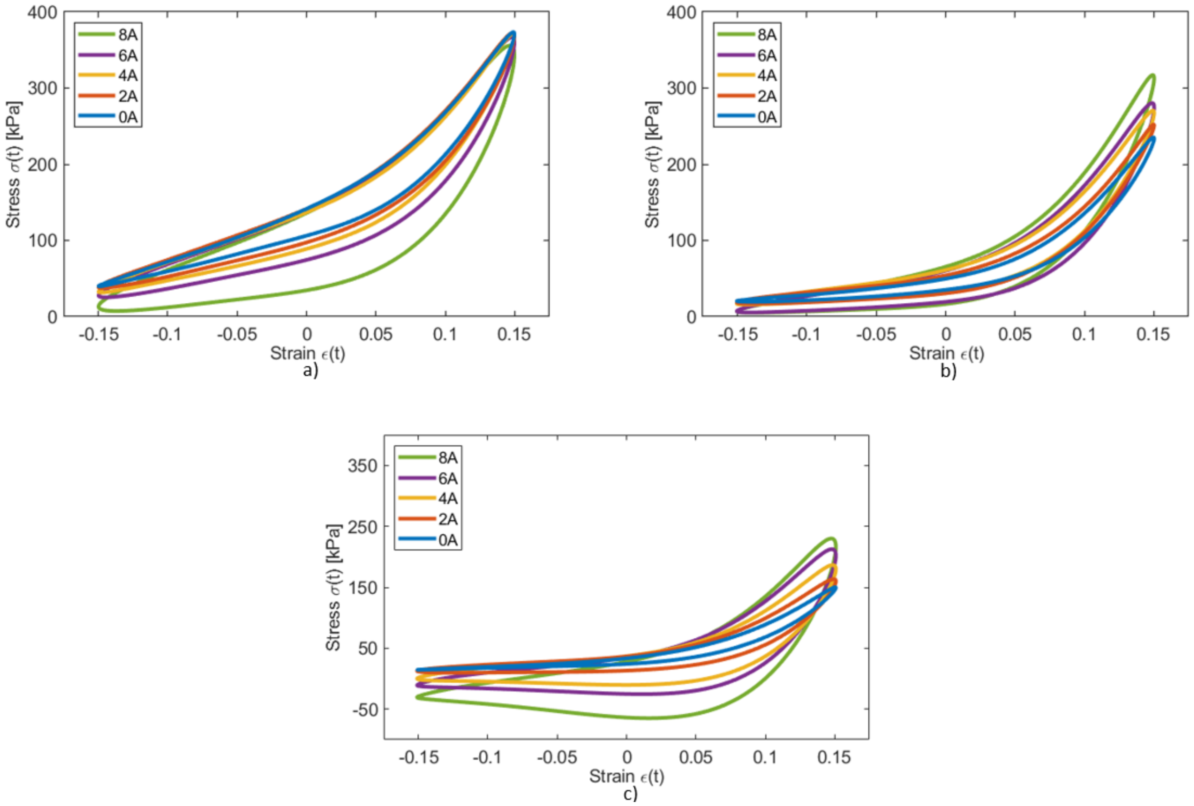

Figure 3.10: Measured hysteresis of 3 different sample types (f=1 Hz. ε_0*=15%) (a) Cube MRE 30mm (b) Cube MRF-E 20mm (c) Cube MRF-MRE 30mm*

Examination of results show that the slope of major axis and the area enclosed by the hysteresis loops substantially increase with the increasing the input current. These observations suggest a magnetic field stiffening effect similar to the strain rate stiffening. The rate of increase in the equivalent stiffness and energy dissipation with the current, however, start to decrease at higher levels of current (above 6A), which suggest magnetic saturation.

Comparing each of the sample types, it is apparent that the MRE indicates the least amount of change in slope while the hybrid MREs show the greatest. The corresponding enclosed areas of different samples further implies that MRF-MREs have higher damping characteristics as compared to those of MRE and MRF-E samples. This partly due to the added effect of damping from the MRF and MRE. With respect to MRF-MRE sample, it is interesting to note that peak negative stress (tension) is seen and as it becomes more magnetically activated. This can be in part attributed to the magnetic field-stiffening of the MR sample that limits recovery or unloading of the specimen.

3.5 Equivalent Elastic (Storage) Modulus

As it was mentioned in section 3.2, the value of the equivalent elastic modulus can be evaluated using the nonlinear stress-strain hysteresis loop along with the Fourier series first harmonic approximation. It is noted that the equivalent loss modulus could not be investigated, as much of the data did not exhibit a consistent trend (examples are provided in Appendix A). Similar to the nonlinear hysteresis stress-strain characteristics loops, the effects of design factors (shape and shape factor) and loading factors (frequency, amplitude and current) on the elastic modulus of the MR samples are thoroughly investigated. The results are presented in the following subsections.

3.5.1 Effects of Shape Factor

The effect of shape factor (SF) on the dynamic properties of the MRE samples are evaluated in terms of the elastic modulus (E'). Figure 3.11, Figure 3.12*,* Figure 3.13 show the effect of shape factor on the storage modulus of MRE samples with respect to frequency, strain amplitude, and current, respectively. Figure 3.11 illustrates the difference in the storage modulus between MREs of two shape factors, 0.25 and 0.375, across different levels of frequency, subject to a strain amplitude of 5%, and a current of 4A.

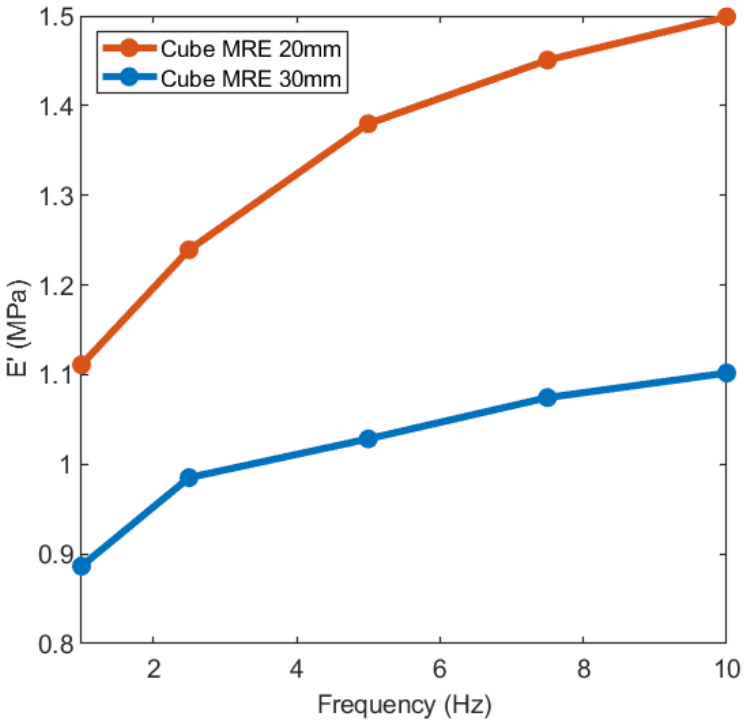

Figure 3.11: Effects of frequency on the elastic modulus with MREs of different shape factors (ε_0=5%, I=4A)

Figure 3.12 illustrates the difference in the moduli between MREs of two shape factors, 0.25 and 0.375, across different levels of strain amplitude, subject to an excitation frequency of 2.5 Hz, and at a current of 6A.

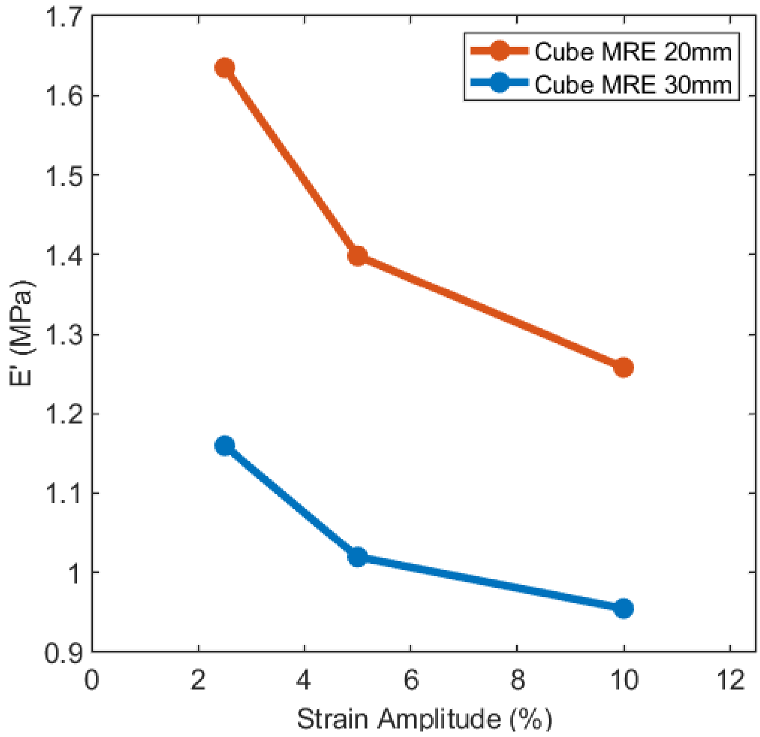

Figure 3.12: Effects of strain amplitude on the elastic modulus with MREs of different shape factors (f=2.5 Hz, I=6A)

Lastly, Figure 3.13 illustrates the difference in the moduli between MREs of two shape factors, 0.25 and 0.375, across different levels of current, subject to an excitation frequency of 10 Hz, and at a strain amplitude of 5%.

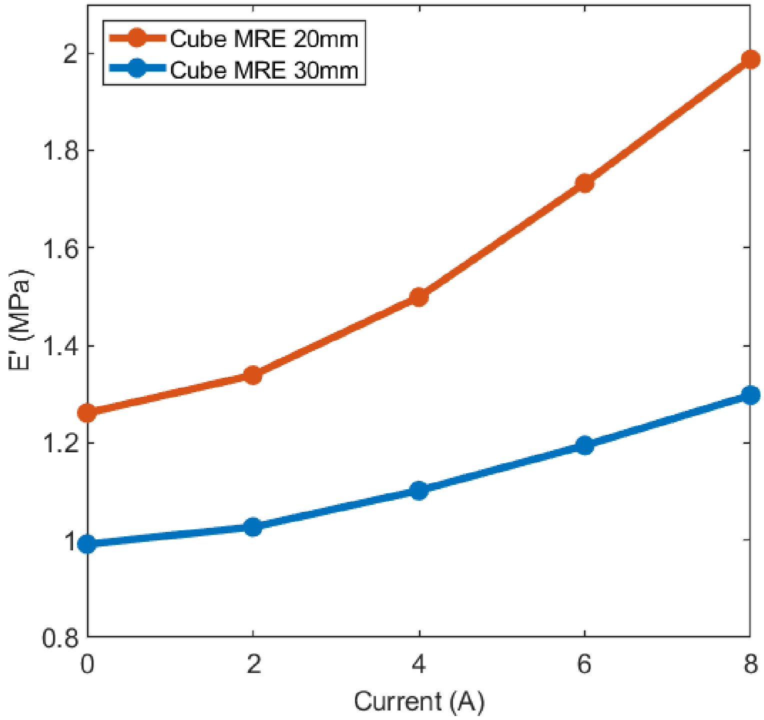

Figure 3.13: Effects of current on the elastic modulus with MREs of different shape factors (f=10 Hz, ε_0*=5%)*

Results clearly show that the elastic modulus significantly increases with the increase in the SF irrespective of frequency, strain amplitude, or applied current confirming previous observations from the hysteresis loop responses. Furthermore, an increase in shape factor generally shows a higher relative change in elastic modulus. For example, as shown in Figure 3.13, by increasing current from 0A to 8A, the storage modulus of Cube MRE 30 mm (SF=0.25) increases from 1 MPa to almost 1.2 MPa (20% increase) while storage modulus of Cube MRE 30mm (SF=0.375) increases from 1.25 MPa to almost 2 MPa (60% increase) when applied current increases from 0 to 8A. Thus, suggest that MR effect substantially increases by increasing the shape factor for the MREs. Same observation can also be realized from Figure 3.11 in which strain rate stiffening effect is more pronounced for samples with higher shape factor. Also examination of Figure 3.12 reveals that by increasing strain amplitude from 2.5% to 10%, the storage modulus decreases by almost

0.4 MPa and 0.2 MPa for Cube MRE 20 mm (SF=0.375) and Cube MRE 30mm (SF=0.25) samples, respectively. Figure 3.11 to Figure 3.13 also further confirms previous observation on strain rate stiffening effect by increasing the frequency, strain amplitude softening effect by increasing strain amplitude and magnetic field stiffening effect by increasing the applied magnetic field regardless of shape factor.

3.5.2 Effects of Shape (Cubic and Cylindrical)

The effect of shape of the MR samples on the dynamic properties of the MRE, MRF-E, and MRF-MRE samples are investigated. Figure 3.14, Figure 3.15, Figure 3.16 show the effects of shape with respect to frequency, strain amplitude, and current, respectively.

Figure 3.14 shows the variation in elastic moduli of the cubic and cylindrical MR samples with respect to excitation frequency subjected to strain amplitude of 5% and applied current of 8A. Results generally show higher elastic modulus for cubic samples (with same shape factor) regardless of the sample type. Results also suggest that the effect of shape is more pronounced for MRE and MRF-MRE samples compared with MRF-E sample. The reduction in elastic modulus for the cylindrical MRE sample from 1 Hz to 2.5 Hz is noteworthy, possibly attributable to experimental error.

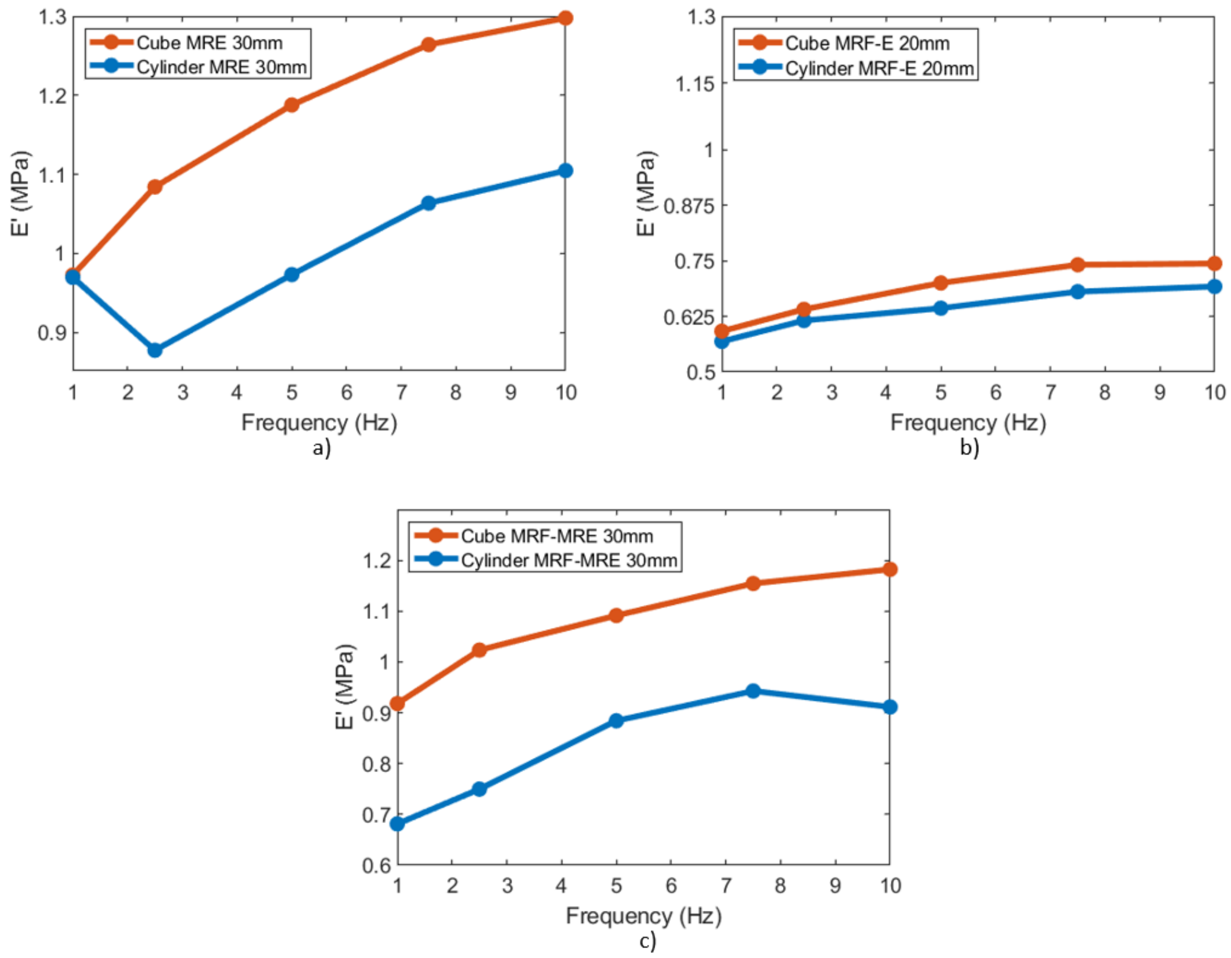

Figure 3.14: Effects of frequency on the elastic modulus with (a) MREs (b) MRF-Es (c) MRF-MREs samples of different shape (ε_0=5%, I=8A)

Figure 3.15 also illustrates variation of elastic modulus for the cubic and cylindrical samples with respect to strain amplitude under excitation frequency of 2.5 Hz and applied current of 6A. Results confirm the strain softening effect as the strain amplitude increases and also show a higher elastic modulus for cubic samples compared to cylindrical samples with the same shape factor. The effect of shape is more pronounced for MRE samples compared with MRF-E and MRF-MRE samples. It is noted that an error has been observed with the cubic MRF-E sample at a strain amplitude of

10%.

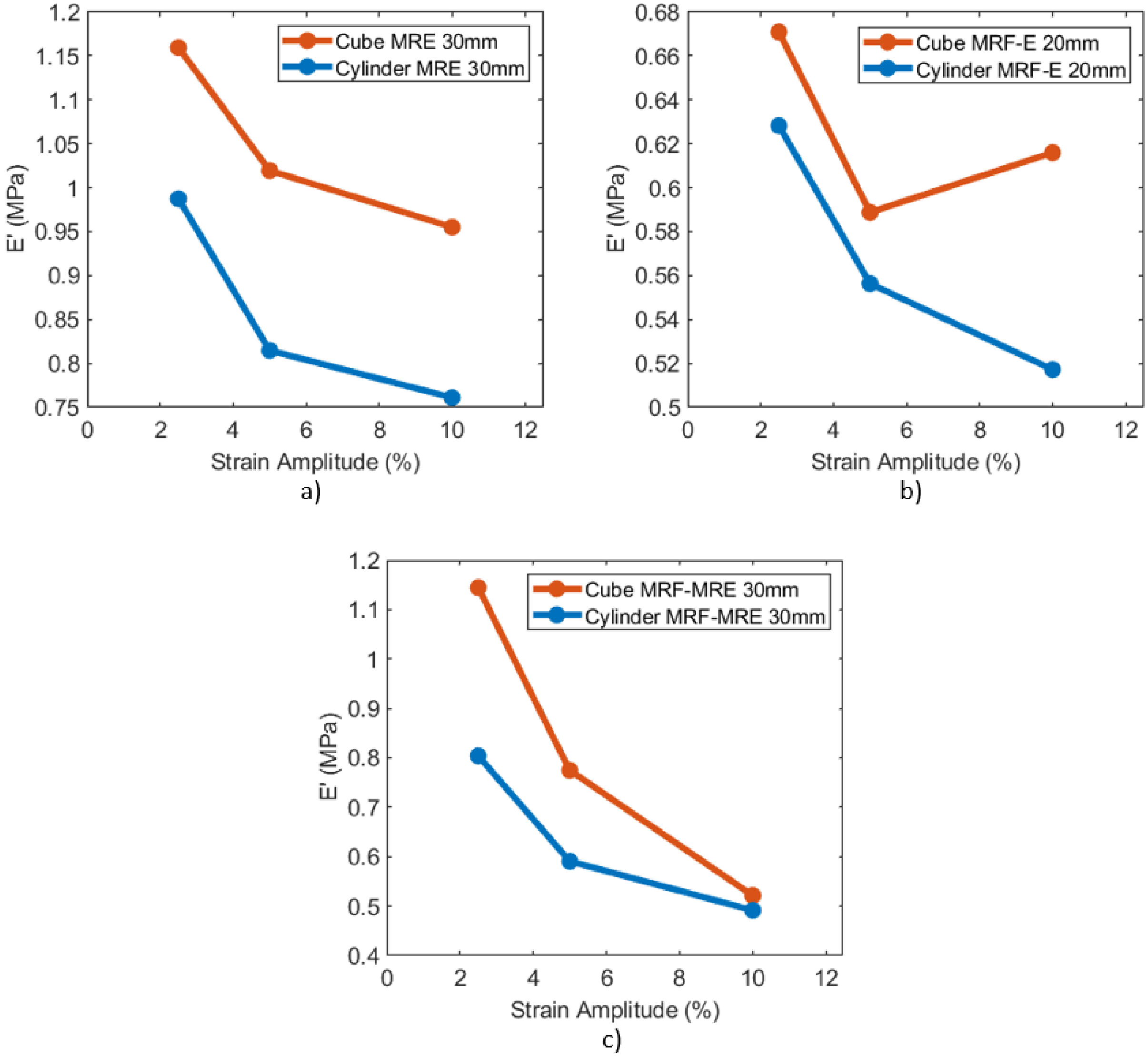

Figure 3.15: Effects of strain amplitude on the elastic modulus with (a) MREs (b) MRF-Es (c) MRF-MREs samples of different shape (f=2.5 Hz, I=6A)

Figure 3.16 reveals the variation of elastic modulus with respect to the applied current for cubic and cylindrical samples under excitation frequency of 2.5 Hz, and a strain amplitude of 5%.

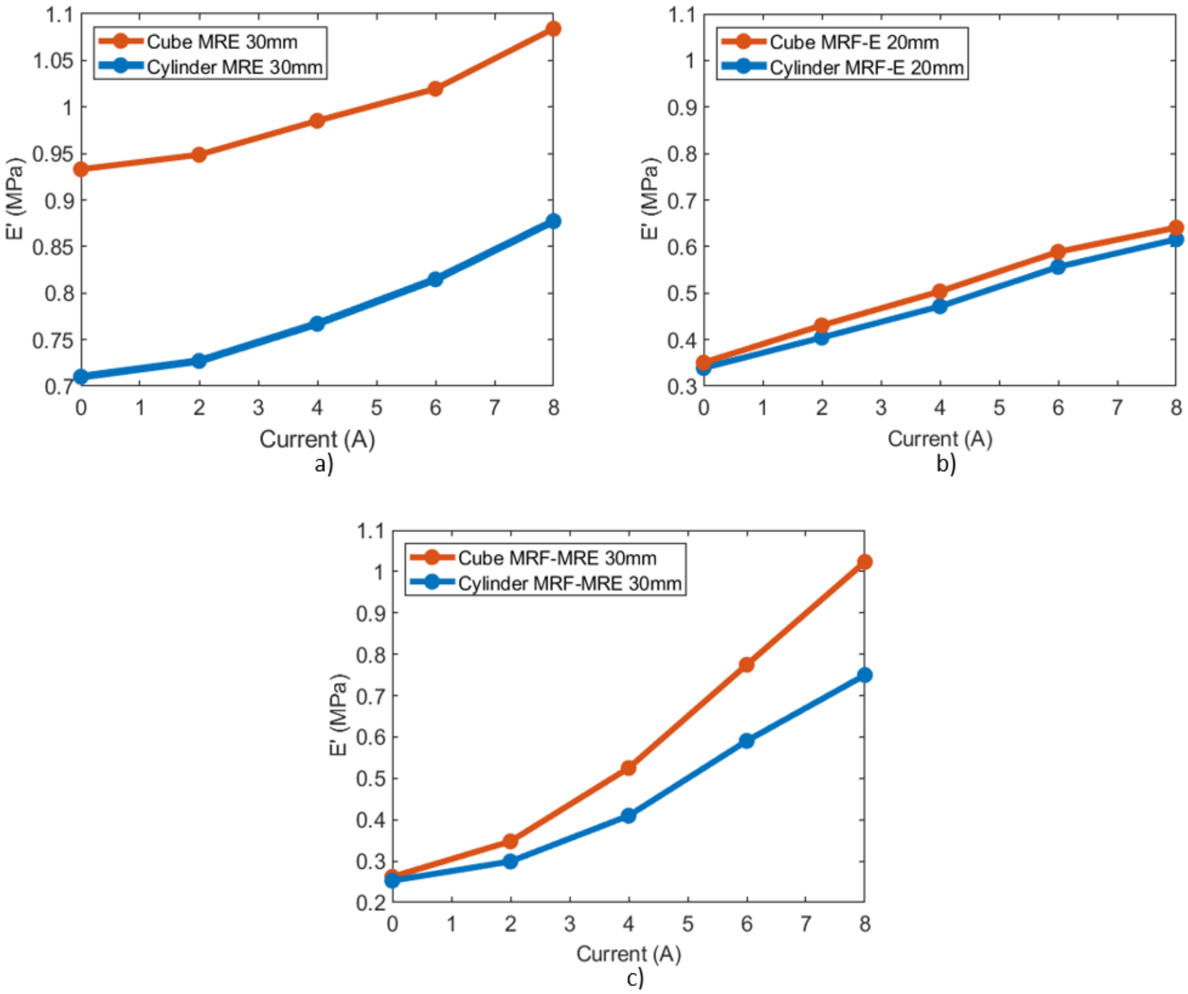

Figure 3.16: Effects of current on the elastic modulus with (a) MREs (b) MRF-Es (c) MRF-MREs samples of different shape (f=2.5 Hz. ε_0=5%)

Results clearly show the magnetic field stiffening effect regardless of the shape of the MR samples. Cubic MR samples show higher elastic modulus compared with their cylindrical counterparts for the given shape factor. The effect of shape is particularly more pronounced for MRE samples and less significant for MRF-E samples.

Results generally suggest that irrespective of frequency, strain amplitude, and current, the shape of MRF-E samples has insignificant effect on the relative change in their elastic modulus while it has substantial effect for both MREs and MRF-MRE samples. For example, from Figure 3.16(a) and Figure 3.16(b), the increase in modulus in cubic sample compared with cylindrical sample is maximum 0.025MPa which is much smaller compared with that of MRE samples which is found to be nearly 0.25 MPa.

It is noted that for MRF-MRE samples, the effect of shape on elastic modulus becomes more pronounced as the current increases, particular for the current above 4A. This is likely due to the higher concentration of MR fluid and MRE materials per unit volume of cubic samples compared with cylindrical samples. As the current applied intensifies, the magnetic particles suspended in the MR fluid within the cavity begin to organize into chain-like structures. This, coupled with the stiffening of the MRE shell, markedly enhances stiffness as the current increases.

3.5.3 Effects of the Excitation Frequency

Figure 3.17 illustrates the effect of excitation frequency on the elastic modulus for different MR samples, subject to a strain amplitude of 5% and different applied currents.

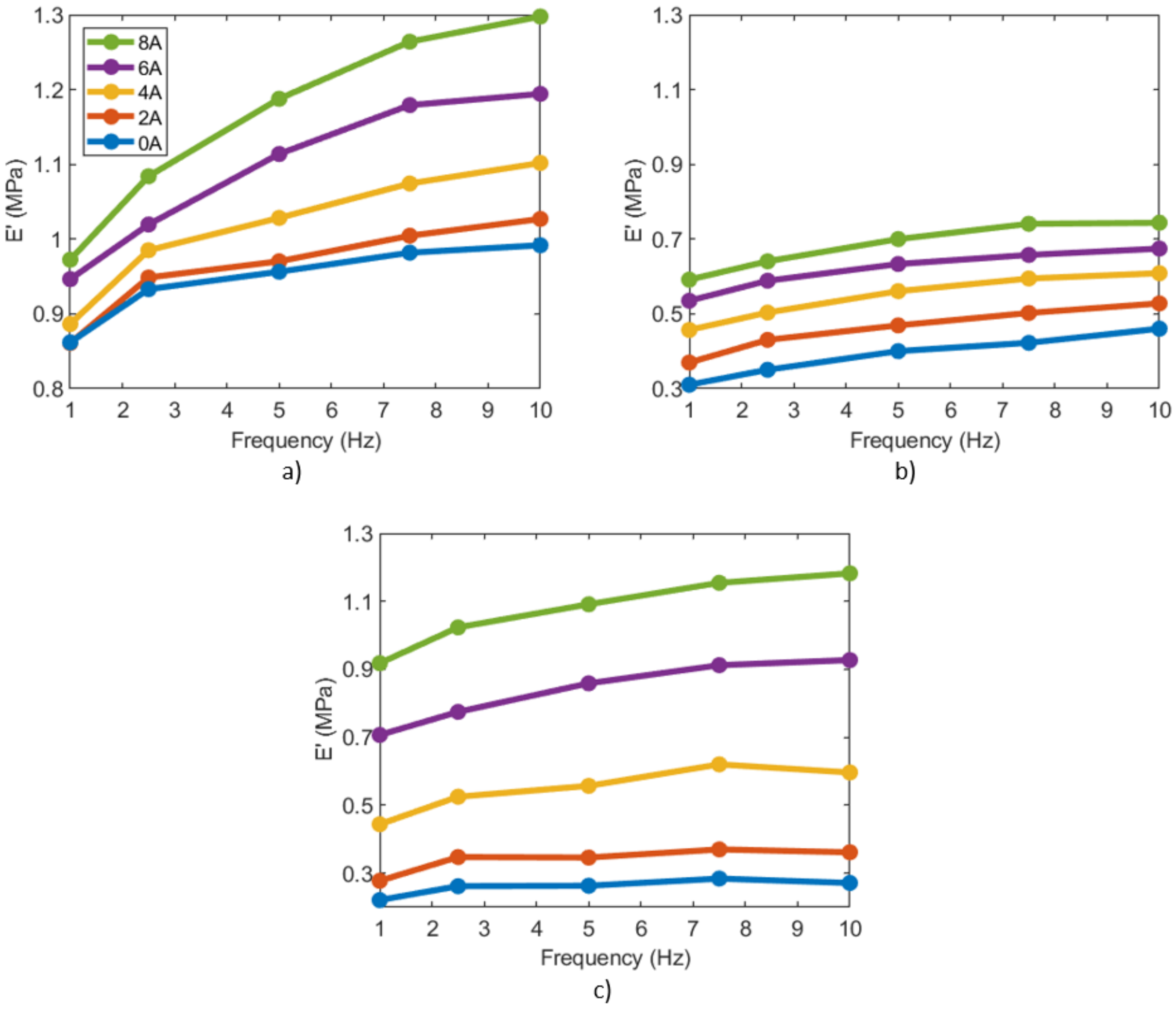

Figure 3.17: Effects of frequency on the elastic modulus of 3 different MR sample types at a strain amplitude of 5% with varying currents (a) Cube MRE 30mm (b) Cube MRF-E 20mm (c) Cube MRF-MRE 30mm

Results show that the elastic modulus increases with rising excitation frequency, indicating the presence of a strain-rate stiffening effect. In general, the rate of increase in elastic modulus decreases as the excitation frequency increases until reaching saturation. This is consistent with the observations made from stress-strain hysteresis loops. Results also show that the effect of frequency is more pronounced in MRE sample, and it has nearly an insignificant effect in the MRF-E sample. This can be attributed to the solid nature of the MRE samples and thus are more sensitive to the excitation frequency.

3.5.4 Effects of Strain Amplitude

Figure 3.18 illustrates the dependency of elastic modulus on the strain amplitude subjected to different applied current and excitation frequency of 2.5 Hz.

From Figure 3.18, it is apparent that the elastic modulus decreases with increasing strain amplitude, irrespective of the applied current or type of MR samples, confirming the strain amplitude softening effect observed previously. It is note that the rate of decrease substantially declines for strain amplitudes beyond 5%. It is also interesting to note that strain dependency of the elastic modulus increases by enhancement of the current, especially above the 4A region. In other words, strain softening is more pronounced at higher applied current as compared to lower current.

Comparing sample types, the hybrid MRF-MRE sample sees the most substantial reduction in elastic modulus at higher currents comparatively to other samples. For example, for MRF-MRE sample at the applied current of 8A, the elastic modulus is reduced by nearly 0.35 MPa by increasing the strain amplitude from 2.5% to 5%. while that for MRE and MRF-E are 0.2 MPa and 0.1 MPa, respectively.

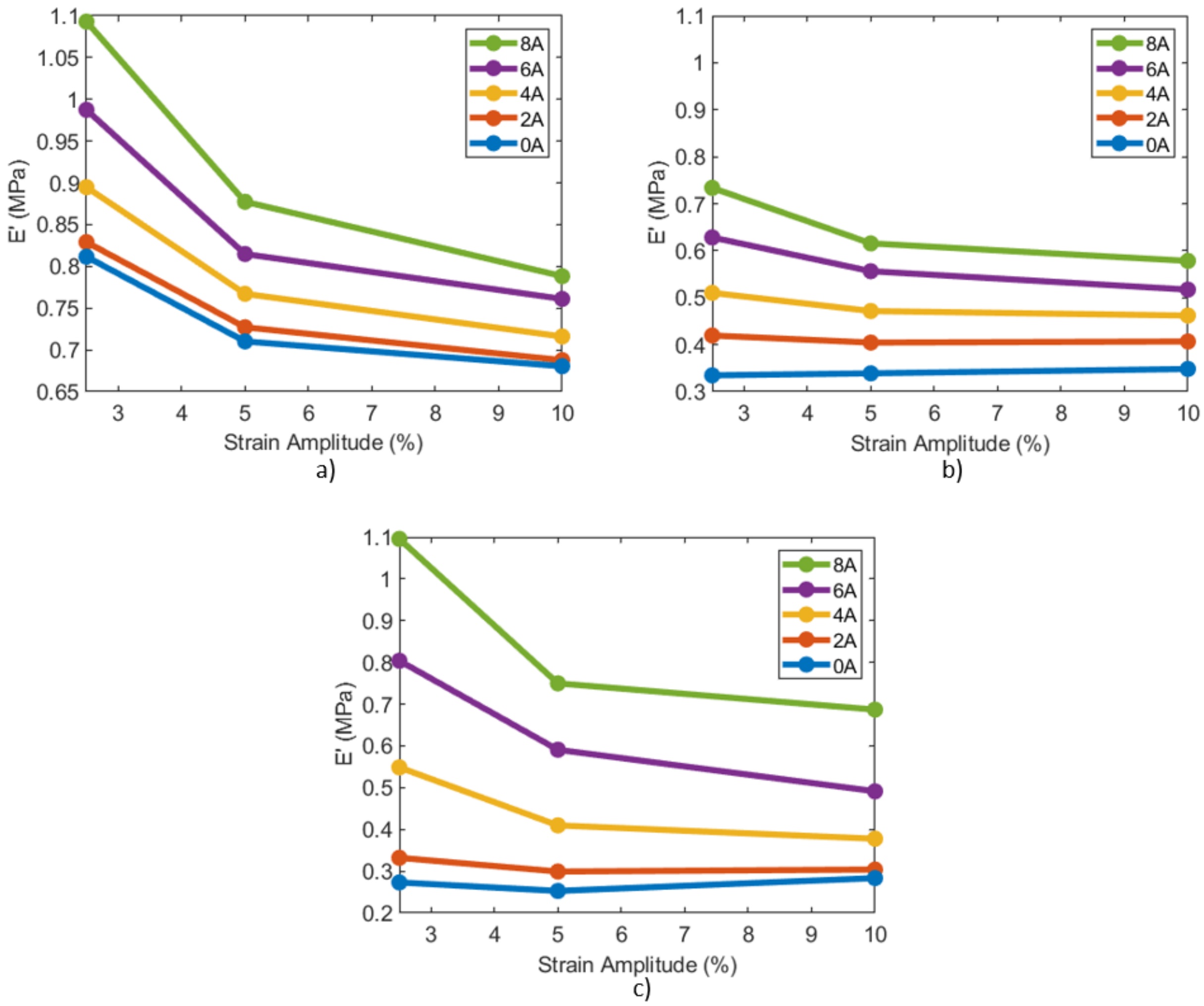

a)

b)

c)

Figure 3.18: Effects of strain amplitude on the elastic modulus of 3 different sample types at 2.5 Hz with varying currents (a) Cylinder MRE 30mm (b) Cylinder MRF-E 20mm (c) Cylinder MRF-MRE 30mm

3.5.5 Effects of Magnetic Field Intensity

The variation of elastic modulus for different MR samples with respect to the applied current for the given strain amplitude of 5% and under varying frequencies is shown in Figure 3.19.

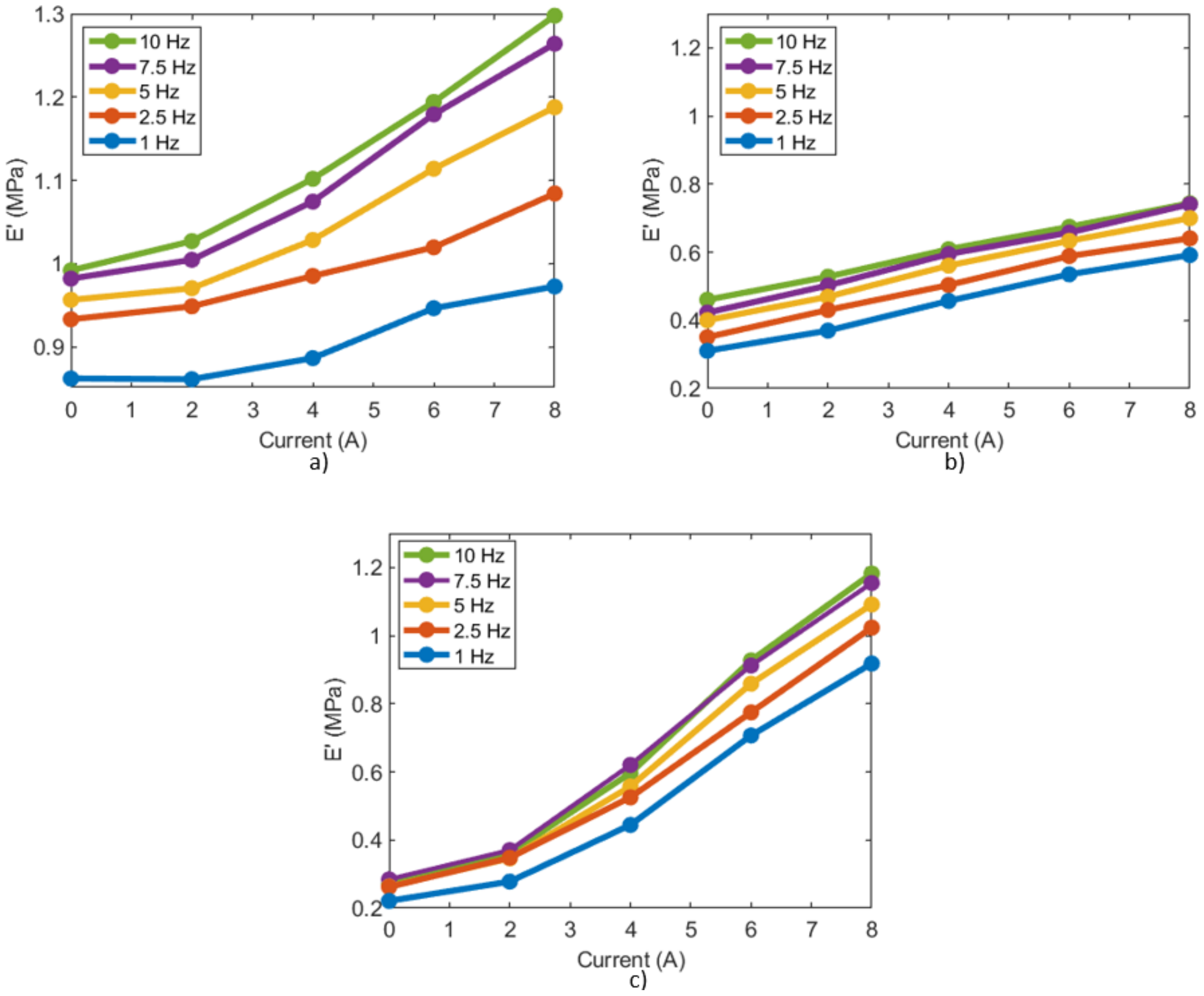

Figure 3.19: Effects of current on the elastic modulus of 3 different sample types at a strain amplitude of 5% with varying frequencies (a) Cube MRE 30mm (b) Cube MRF-E 20mm (c) Cube MRF-MRE 30mm

Examination of Figure 3.19 reveals the elastic modulus increases substantially by enhancement of the current, regardless of the excitation frequencies and type of MR materials. It is noted that the rate of increase in the elastic modulus decreases as the applied current reaches higher than 6A indicating saturation at applied current beyond 8A.

Comparing the samples, the MRF-MRE sample shows the greatest tuneability. For instance, at a frequency of 10 Hz the elastic modulus ranges from around 0.3 MPa at 0A and increases exponentially to 1.2 MPa at 8A, an increase of nearly four times. While for the MRF-E sample, the elastic modulus increases from 0.45 MPa to 0.75 MPa by increasing current from 0 to 8 A.

This can be better realized in Figure 3.20 which compares the variation in elastic modulus with respect to applied current for all 8 MR samples under excitation frequency of 5 Hz and strain amplitude of 2.5%.

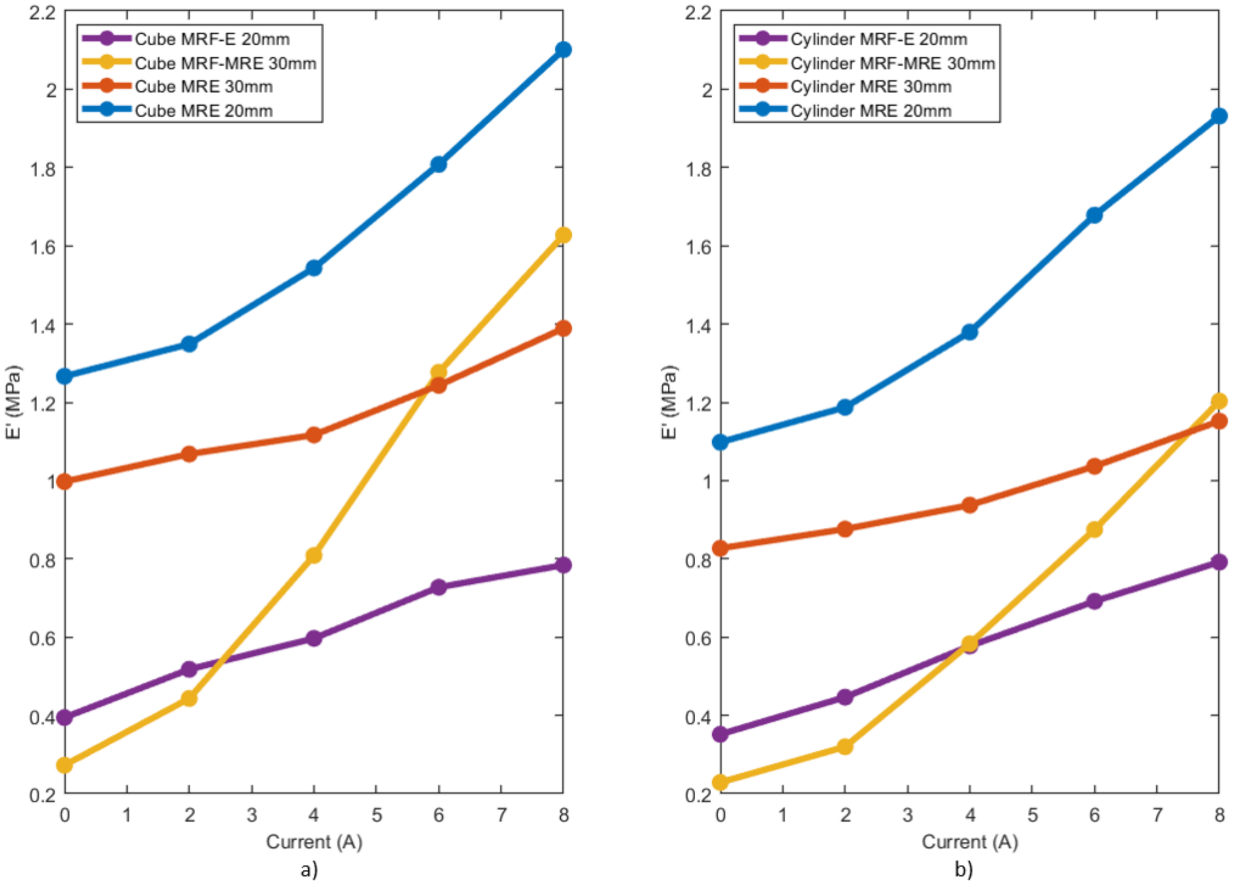

Figure 3.20: Effects of current on the elastic modulus (f=5 Hz. ε_0=2.5%) (a) cubic samples (b) cylindrical samples

Figure 3.20 clearly shows the impressive capabilities of the cubic and cylindrical MRF-MRE as both samples show the largest increase in elastic modulus from 0A to 8A. The absolute MR effect ($\Delta E'$) and relative MR effect as described in Eqs. (3.5) and (3.6), respectively can be affectively used to quantify the adaptability and variation in elastic modulus of the MR samples

$$\Delta E' = E'_{I=8A} - E'_{I=0A} \tag{3.5}$$

$$MR_{effect}(\%) = \frac{E'_{I=8A} - E'_{I=0A}}{E'_{I=0A}} \tag{3.6}$$

Table 3.2 summarizes the results for the absolute and relative MR effect for MR samples.

Table 3.2: Summary of the MR Effect across all samples (f=5 Hz. ε_0=2.5%)

Sample	Static Modulus (0A)	Max Modulus (8A)	Absolute MR Effect	Relative MR Effect (%)
Cube MRE 20mm	1.26	2.1	0.84	66.66
Cube MRE 30mm	1	1.39	0.39	39
Cube MRF-MRE 30mm	0.28	1.62	1.34	478.6
Cube MRF-E 20mm	0.39	0.78	0.39	100
Cylinder MRE 20mm	1.1	1.93	0.83	75
Cylinder MRE 30mm	0.82	1.15	0.33	40.2
Cylinder MRF-MRE 30mm	0.22	1.2	0.98	445.5
Cylinder MRF-E 20mm	0.35	0.8	0.45	128.6

Results in Table 3.2 show that the hybrid cubic and cylindrical MRF-MRE samples show the highest relative MR effect of nearly 479% and 446%, respectively. It is also noted that samples with higher shape factor have substantially higher relative MR effect. For instance, Cube MRE 20 mm with SF of 0.375 has the MR effect of nearly 67% compared with relative MR effect of 39% for Cube MRE 30 mm with SF of 0.25. It is also interesting to note that cylindrical samples for the same SF have slightly higher relative MR effect compared with their cubical counter parts except for hybrid MRF-MRE.

3.6 Discussion of Results

Due to the inherent nonlinearities in compression mode testing, establishing a clear and consistent relationship for loss modulus proved challenging, as no discernible pattern emerged. Upon correcting for the magnetic force in the hysteresis loops, it became apparent that the samples had been subjected to a slightly higher pre-strain than intended. This inadvertent compression might have impacted their magnetic properties and elastic recoverability (relaxation time) prior to cyclic testing. It is probable that this also influenced various aspects of the hysteresis loops, such as mean stress, slope, or area, occasionally leading to inaccuracies. Thankfully, the extensive volume of recorded data allowed for the identification and resolution of many of these issues.

When viewing the effects of shape factor, the results showed a noticeable increase in the material's stiffness and MR effect. Similar behaviour has also been reported by Vatandoost et al. [33] who experimentally investigated the effect of increasing the shape factor and found similar shape factor stiffening for MREs of anisotropic and isotropic structures. In addition, the effect of the sample's shape for samples of equal shape factor was also investigated. It was discovered that for the MREs and MRF-Es, an increase in the material's stiffness was seen with no effect on its magnetorheological abilities. This is due to the friction at the loaded surfaces which resists expansion of the rubber specimen during tests, thus contributing to relatively higher effective modulus of the rubber [33]. Since the cubic samples have a larger loading area, their storage modulus is notably higher than their cylindrical counterparts. However, for the hybrid MRF-MREs, a unique effect was observed. Initially, the influence of shape is nearly nonexistent at 0A and 2A due to the material's softness. However, as the current increases, the MR fluid begins to form sturdier columnar chains and the MRE walls stiffen. Eventually, reaching a point where the friction on the loading area becomes more relevant. This causes the MR effect to be substantially higher for the cubic MRF-MRE sample.

When viewing the effects of frequency, typical strain-rate stiffening was seen throughout the samples. The response of this effect is characterized by an increase in stiffness as the rate of deformation increases, as evidenced by the amplified elastic modulus and slopes in the hysteresis loops. This means that the material becomes more resistant to deformation at higher rates of frequency. The mechanism behind strain-rate stiffening involves the alignment dynamics of the ferromagnetic particles within the elastomer or fluid matrix. At higher frequencies, the particles have less time to reorient themselves in response to the applied stress, resulting in a greater resistance to deformation [27, 33]. Additionally, higher currents influence the particle alignment more effectively at higher deformation rates, contributing to the observed stiffening behaviour. When comparing the sample types, it was evident that this phenomenon had much more affect on the MREs. However, once the current reaches higher levels, above 6A, the effect becomes more noticeable for the hybrid samples. This is due to the MRF within the samples becoming more solid-like as the columnar structures become stronger. While at lower currents, below 4A, the fluid's weaker structure can move more freely.

When viewing the effects of strain amplitude, a gradual decrease was seen in the elastic modulus across all the samples. Known as strain softening or Payne effect, this phenomenon is mainly due to weakening of the bond between the filler particles, as well as between the rubber matrix and the filler particles, which is a widely reported phenomenon for natural filled rubbers. As the strain amplitude rises, the particle network structure begins to yield, causing the chains to buckle. This leads to an expansion in the spacing between the dipoles, ultimately resulting in a reduction in the stiffness of the compressed sample [3, 8, 27]. This also means that when a current is applied, the strain softening behaviour becomes increasingly more dependent and reactive to the strain amplitude. Hence, higher currents resulted in increased losses. When comparing the samples, much like seen in the strain-rate stiffening effect, the hybrid samples are mostly unaffected by the increase in strain amplitude for lower currents, below 4A, for much of the same reasons. Then at higher currents, above 6A, they become much more reactive to strain amplitude. However, the hybrid MRF-MRE samples exhibit a more pronounced decrease in elastic moduli at these higher currents. Since the MRF-MREs are encapsulated by an MRE and can become much stiffer, strain softening becomes a detrimental effect.

When viewing the effects of current, multiple conclusions can be made. Specifically, from Table 3.2, the MR effect was found to be substantially greater in the samples containing MR fluid, as the MRF transitions from a fluid state to a quasi-solid state. The MRF-MREs exhibited the largest MR effect, which was evident due to the use of an MRE shell. Due to the solid nature of MREs, the magnetic particles are trapped in the elastomer matrix, and the effect of increasing current had the least amount of impact on the change in stiffness and moduli. For many of the samples, their cylindrical counterparts had a greater relative MR effect due to their lower static elastic modulus. This was not the case for the MRF-MRE, where due to the unique influence of shape became much more significant, thereby increasing the MR effect for the cubic sample.

3.7 Summary

A compression experimental test setup was designed with the goal to investigate the field-dependent viscoelastic behaviour of various types of MREs, including MRF-MREs, MRF-Es, and MREs of different shapes (cube and cylindrical) and shape factors (0.25, and 0.375), under a wide range of excitation frequencies, strain amplitudes, and applied currents. A total number of 110 tests are carried out for each sample, and their respective stress-strain curves and moduli were obtained to analyze the effects of shape factor, shape, frequency, strain amplitude, and current. It was demonstrated that the hybrid MRF-MRE samples exhibited a staggering relative MR effect of 450%. The MRF-E yielded a relative MR effect of 100%. While the 30mm MREs and 20mm MREs only showed a relative MR effect of around 40% and 70%, respectively. Following the interpretation of the experimental results in detail, it is apparent that the MRF-MRE provides a significant advantage over an MRF-E or MRE.

Chapter 4: Development of the Material Model

4.1 Introduction

The development of a material model to predict the dynamic behavior of MR materials is of paramount importance for the development and design of MR-based adaptive systems, as well as for synthesizing control strategies. In this section, based on the observed experimental data discussed and analyzed in Chapter 3, a phenomenologically based model is developed to reasonably predict the dynamic viscoelastic and hysteresis behaviour of the MRE and hybrid MREs in compression mode while taking into account the variation in excitation frequency, strain amplitude, and applied current.

4.2 Development of a Field-Dependent Viscoelastic Model

In this study, a field-dependent viscoelastic model based on the modified Kelvin-Voigt model has been developed to predict the stress-strain response behaviour of the MR materials addressed in Chapter 3. Under the harmonic strain excitation expressed as:

$$\varepsilon(t) = \varepsilon_0 \sin(2\pi f t) \tag{4.1}$$

the generated total stress based on the Kelvin-Voigt model consists of elastic and viscous parts which can be described as:

$$\sigma(t) = E'(f, I, \varepsilon_0)\, \varepsilon(t) + E''(f, I, \varepsilon_0)\, \dot{\varepsilon}(t) \tag{4.2}$$

Here, in contrast to conventional linear viscoelastic material, storage modulus (E') and loss modulus (E'') are not only functions of frequency (f) but also, strain amplitude (ε_0) and applied current (I). The sketch of the proposed modified Kelvin-Voigt model is shown in Figure 4.1.

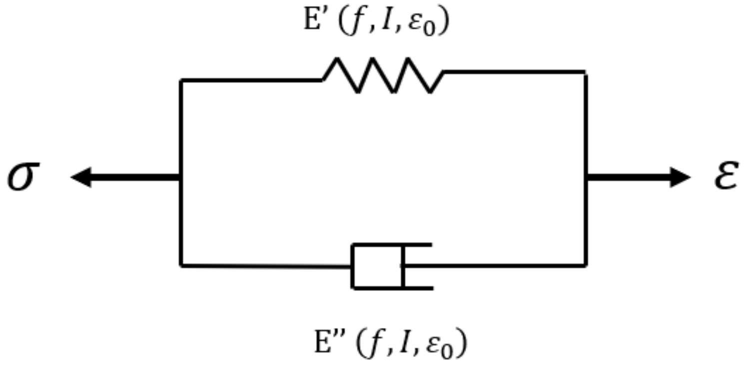

Figure 4.1: Proposed modified Kelvin-Voigt model for MR materials

Vatandoost et al. [8] investigated several phenomenological models for predicting the dynamic properties of only MREs. In their study, a similar modified viscoelastic Kelvin-Voigt model is introduced which outperformed other models.

Based on the experimental observation, the following power functions for elastic modulus (E') and loss modulus (E'') are proposed by Vatandoost et al. [8] in which f_0 is a reference frequency of 1 Hz:

$$E'(f, I, \varepsilon_0) = a_B \left(\frac{f}{f_0}\right)^b {\varepsilon_0}^{c_B} \tag{4.3}$$

$$E''(f, I) = d_B \left(\frac{f}{f_0}\right)^{1+e} \tag{4.4}$$

where a_B, b, c_B, d_B, e are model characteristics parameters. In the study, these five parameters were identified by implementing the nonlinear regression algorithm in order to minimize the error between experiment moduli and model-predicted moduli for each given increment of the applied current. After performing the optimization at different currents while varying the frequency and strain amplitude, it was found that the parameters a_B, c_B, d_B are field dependent while b and e remained constant irrespective of the applied current. It was realized that the variation of the a_B

and d_B with respect to the applied current can be approximated using a quadratic function while the variation of c_B with respect to the applied current is nearly linear. The three polynomial functions for the magnetic field dependent parameters a_B, c_B, d_B may thus be represented as:

$$a_B(I) = \beta_1' I^2 + \beta_2' I + \beta_3' \tag{4.5}$$

$$c_B(I) = \beta_4' I + \beta_5' \tag{4.6}$$

$$d_B(I) = \beta_1'' I^2 + \beta_2'' I + \beta_3'' \tag{4.7}$$

Vatandoost et al. [8] argued that based on experimental results, the loss modulus remains constant with varying strain amplitude. Although no discernible pattern could be retrieved from the measured data in Chapter 3, the loss modulus generally depended on the strain amplitude. Therefore, to maintain consistency between moduli Eqs. (4.3) and (4.4), a strain dependent equation for the loss modulus is also considered using an exponential function. The proposed model for loss moduli can be described as:

$$E''(f, I, \varepsilon_0) = d_B \left(\frac{f}{f_0}\right)^{1+e} \left(e^{-\beta_4'' * \varepsilon_0}\right) \tag{4.8}$$

By substituting the current dependent Eqs. (4.5-4.7) into Eqs. (4.3) and (4.8), the phenomenological model to describe the elastic and loss moduli can be presented as:

$$E'(f, I, \varepsilon_0) = (\beta_1' I^2 + \beta_2' I + \beta_3') \left(\frac{f}{f_0}\right)^{b} {\varepsilon_0}^{(\beta_4' I + \beta_5')} \tag{4.9}$$

$$E''(f, I, \varepsilon_0) = (\beta_1'' I^2 + \beta_2'' I + \beta_3'') \left(\frac{f}{f_0}\right)^{1+e} \left(e^{-\beta_4'' \varepsilon_0}\right) \tag{4.10}$$

4.3 Parameter Identification Procedure

The proposed phenomenological model presented in Eqs. (4.9) and (4.10) consist of six constant parameters for the elastic modulus (β_1', β_2', β_3', b, β_4', β_5') and five constant parameters for the loss modulus (β_1'', β_2'', β_3'', e, β_4''). These parameters are subsequently identified through minimization of the merit functions J' and J'' in order to minimize the error between the predicted and the respective experimental measured moduli. The merit function J' and J'' are thus defined as:

$$\begin{cases} J' = \displaystyle\sum_{i=1}^{F}\sum_{j=1}^{S}\sum_{k=1}^{I}\left(E'(f,I,\varepsilon_0) - E_m'(f,I,\varepsilon_0)\right)^2 \\ J'' = \displaystyle\sum_{i=1}^{F}\sum_{j=1}^{S}\sum_{k=1}^{I}\left(E''(f,I,\varepsilon_0) - E_m''(f,I,\varepsilon_0)\right)^2 \end{cases} \tag{4.13}$$

where E_m' and E_m'' represent the experimentally measured elastic and loss moduli, respectively, and indices i, j, and k denote the experimental data corresponding to specific values of the frequency, strain amplitude, and current, respectively. F, S and I stand for the number of outcomes corresponding to the respective input factors (frequency, strain amplitude, and applied current) considered in the error function, which were taken as 5 (1, 2.5, 5, 7.5, 10 Hz), 3 (2.5%, 5%, 10%), and 5 (0, 2, 4, 6, 8 A), respectively. The error minimization problem is solved using a combination of the genetic algorithm (GA) and the Sequential Quadratic Programming (SQP) technique. The GA is a stochastic based method for solving optimization problems based on the natural selection process. Generally, GA has demonstrated its capability to produce solutions that are close to the global optimum. Through iterative modification of a population of individual solutions and mimicking the principles of evolution, it can find near-optimal solutions to complex problems. In this study, GA is first executed to obtain a solution near the global minimum. Using the solution from GA as the initial point, the SQP technique, which is a gradient based nonlinear optimization algorithm, is subsequently employed to accurately capture the precise global minimum solution. Repeated runs of GA and SQP yielded nearly identical solutions. The identified coefficients of the model for all MRE and hybrid MRE samples discussed in Chapter 3 are summarized below in Table 4.1 and Table 4.2.

Table 4.1: The identified coefficients of the proposed modified Kelvin-Voigt model for predicting elastic modulus

Sample	E' Parameters					
	β'_1	β'_2	β'_3	b	β'_4	β'_5
Cube MRE 20mm	2172.5	-28166.8	767255.3	0.138	-0.022	-0.072
Cube MRE 30mm	1017.0	-20892.1	696130.6	0.099	-0.016	-0.056
Cube MRF-MRE 30mm	-1242.0	20656.3	65947.0	0.127	-0.038	-0.283
Cube MRF-E 20mm	-1433.2	11417.8	309201.8	0.123	-0.024	-0.014
Cylinder MRE 20mm	1538.3	-28130.6	677718.8	0.107	-0.026	-0.078
Cylinder MRE 30mm	752.0	-10200.4	472661.8	0.122	-0.015	-0.094
Cylinder MRF-MRE 30mm	1676.84	11287.90	78679.10	0.13	-0.007	-0.28
Cylinder MRF-E 20mm	-978.7	21809.8	245511.9	0.087	-0.013	-0.059

Table 4.2: The identified coefficients of the proposed modified Kelvin-Voigt Model for predicting loss modulus

Sample	E'' Parameters				
	β'_1	β'_2	β'_3	e	β'_4
Cube MRE 20mm	3972.76	11255.48	237007.84	-0.82	1.35
Cube MRE 30mm	1842.2	16261.1	182525.0	-0.874	3.248
Cube MRF-MRE 30mm	633.29	78227.81	88271.93	-0.91	6.39
Cube MRF-E 20mm	698.7	20565.1	68949.6	-0.706	4.826
Cylinder MRE 20mm	1962.4	33560.0	209871.8	-0.890	1.817
Cylinder MRE 30mm	3675.6	-7054.4	163915.6	-0.830	3.293
Cylinder MRF-MRE 30mm	3962.12	35817.77	88162.85	-0.89	4.38
Cylinder MRF-E 20mm	1955.2	22044.9	107561.2	-0.826	4.439

The identified parameters in Tables Table 4.1 and Table 4.2 and substituted in Eqs. (4.9) and (4.10) are then used to predict the elastic and loss moduli of investigated MRE and hybrid MREs.

The predicted elastic modulus and its comparison with experimental data are provided in Figure 4.2 to Figure 4.7 as examples. It is noted that in each plot, the colored dots represent the experimental data, and the solid lines formed from a diamond shape represent the predicted results using the model. Discrepancies arising from experimental errors and the nonlinearities from the measured compression data led to the existence of some data points that did not align with physical expectations. Consequently, this data was disregarded and excluded during the parameter identification phase, therefore, the following figures may contain several missing experimental data points. Figure 4.2 and Figure 4.3 compares the variation of predicted elastic modulus with respect to the frequency with the measured data for both cubic and cylindrical MR samples, respectively at a strain amplitude of 2.5% under varying current.

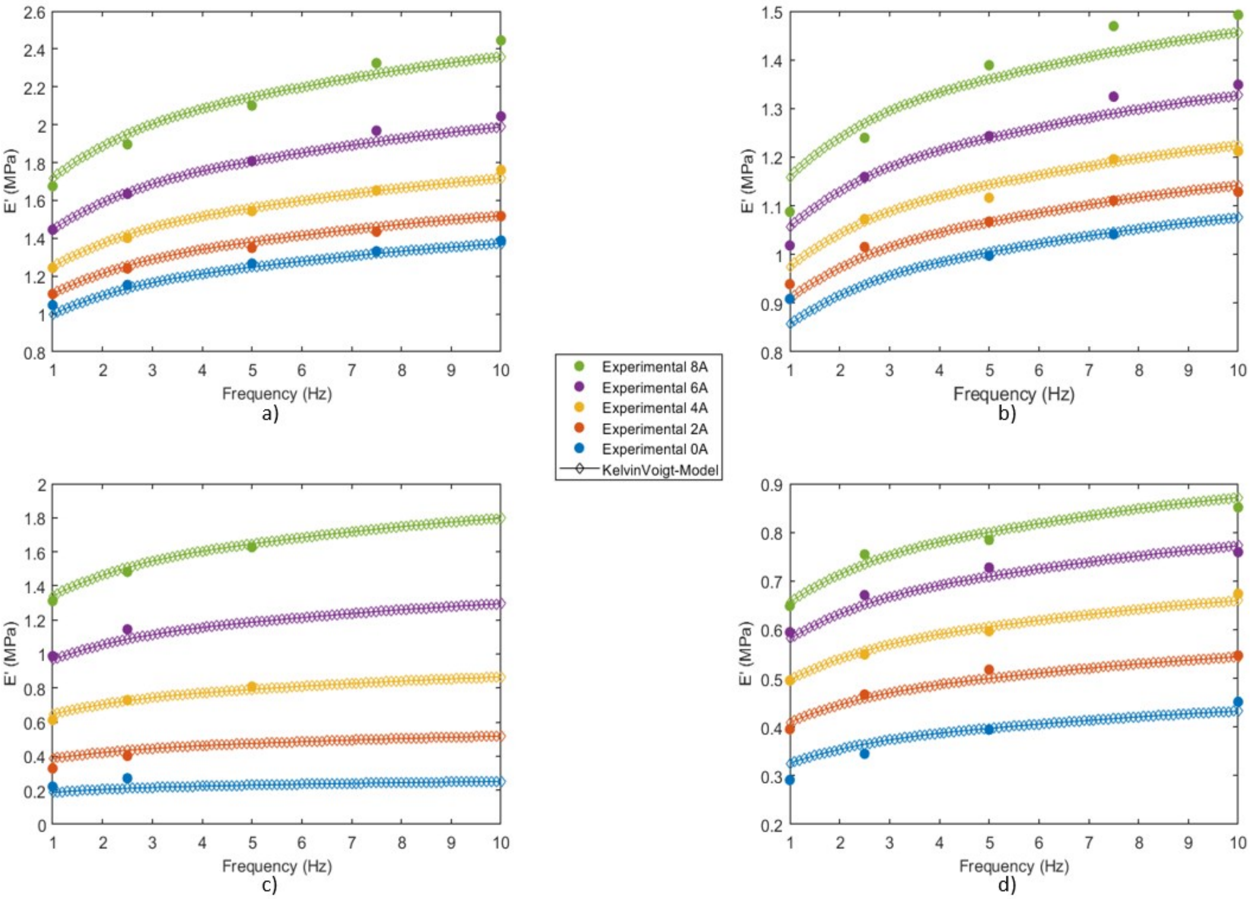

Figure 4.2: Effects of frequency on the elastic modulus of cubic samples at a strain amplitude of 2.5% with varying currents - Kelvin Voigt comparison (a) Cube MRE 20mm (b) Cube MRE 30mm (c) Cube MRF-MRE 30mm (d) Cube MRF-E 20mm

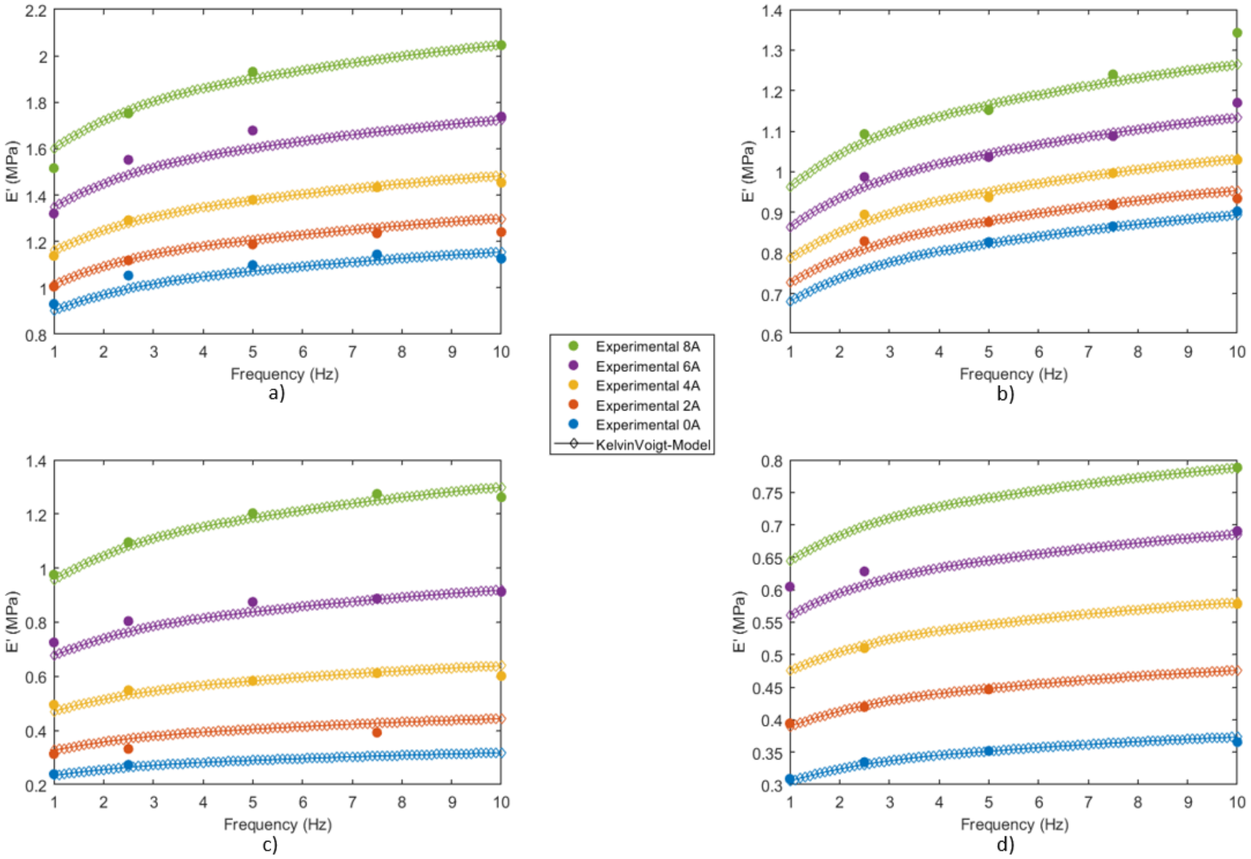

Figure 4.3: Effects of frequency on the elastic modulus of cylindrical samples at a strain amplitude of 2.5% with varying currents - Kelvin Voigt comparison (a) Cylinder MRE 20mm (b) Cylinder MRE 30mm (c) Cylinder MRF-MRE 30mm (d) Cylinder MRF-E 20mm

Figure 4.4 and Figure 4.5 provide comparison between predicted and measured elastic modulus with respect to strain amplitude at a given frequency of 5 Hz under varying applied current for both cubic and cylindrical MR samples, respectively.

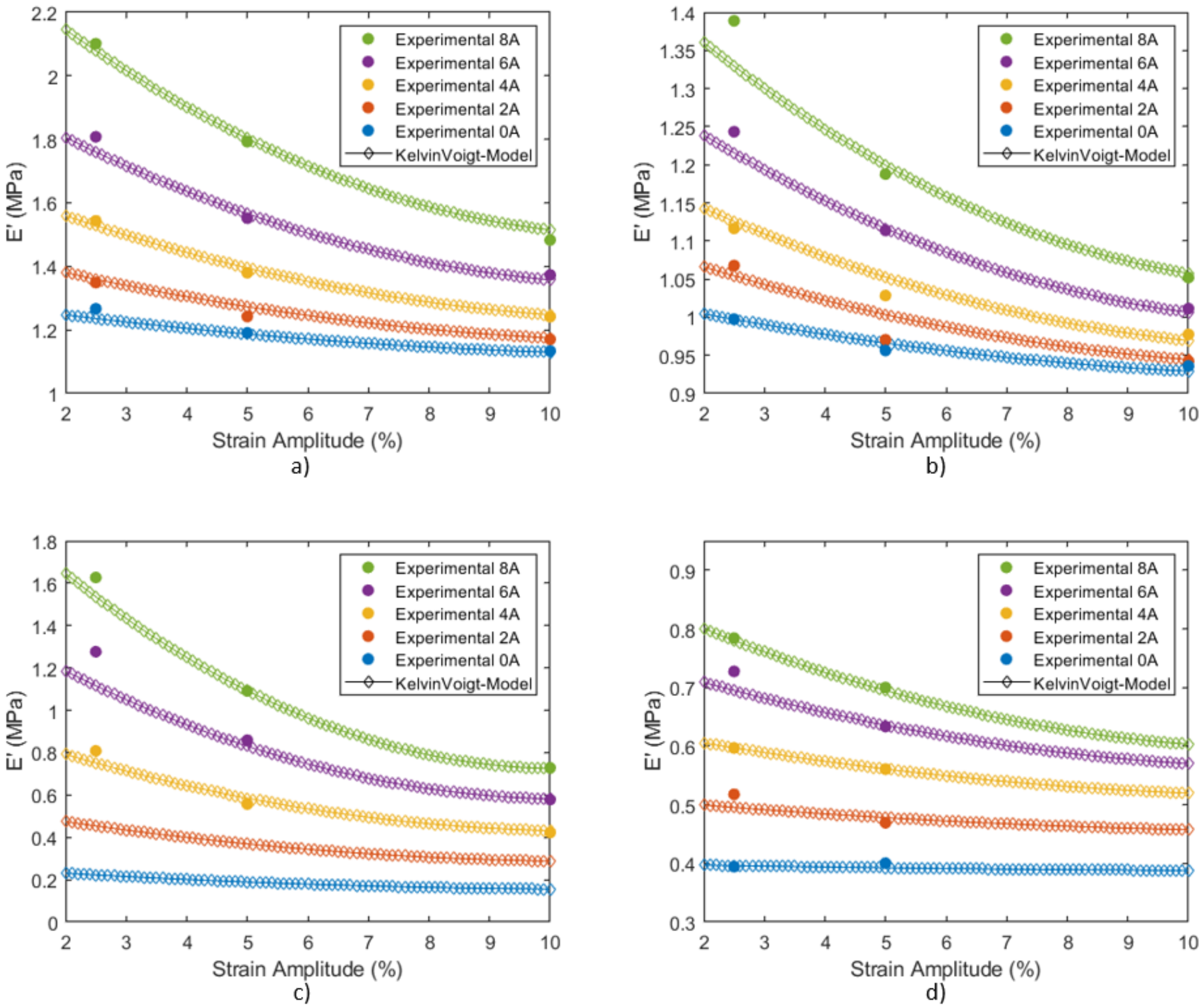

a)

b)

c)

d)

Figure 4.4: Effects of strain amplitude on the elastic modulus of cubic samples at 5 Hz with varying currents - Kevlin Voigt comparison (a) Cube MRE 20mm (b) Cube MRE 30mm (c) Cube MRF-MRE 30mm (d) Cube MRF-E 20mm

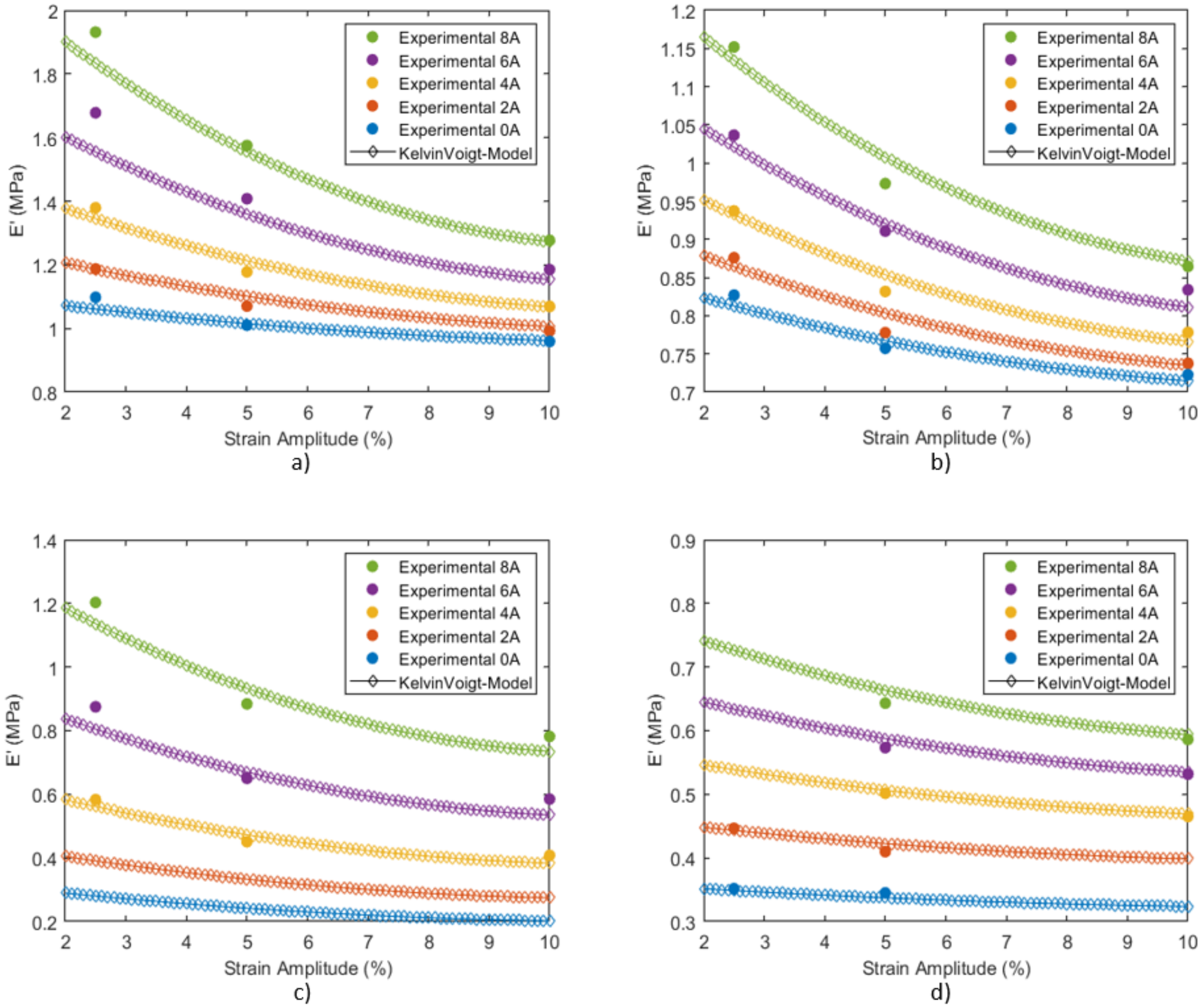
a)
b)
c)
d)

Figure 4.5: Effects of strain amplitude on the elastic modulus of cylindrical samples at 5 Hz with varying currents - Kevlin Voigt comparison (a) Cylinder MRE 20mm (b) Cylinder MRE 30mm (c) Cylinder MRF-MRE 30mm (d) Cylinder MRF-E 20mm

Finally, Figure 4.6 and Figure 4.7 depicts the comparison of the measured data in comparison of the measured elastic modulus with those predicted and their variation with respect to the applied current at a strain amplitude of 5% with varying frequencies.

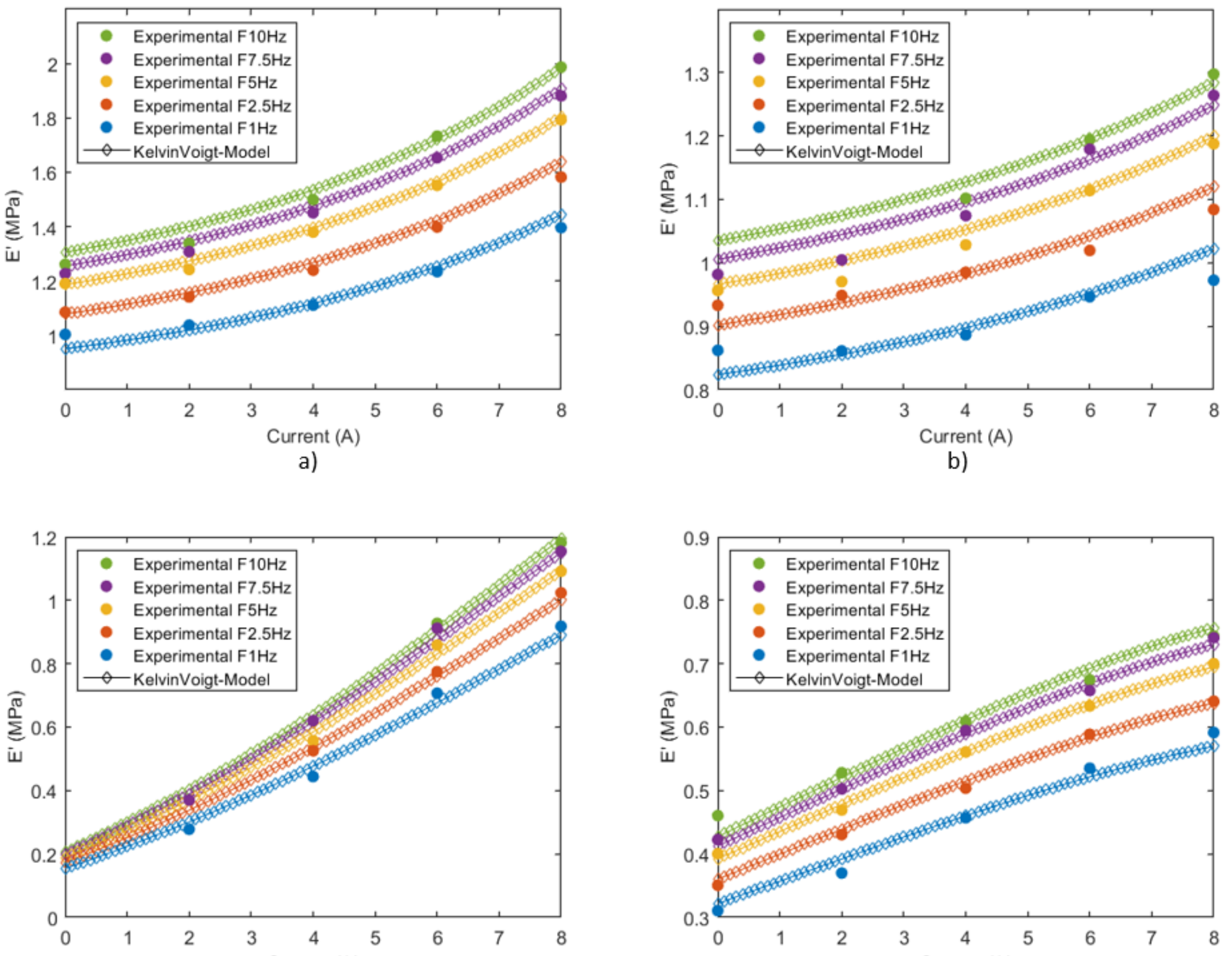

a) b) c) d)

Figure 4.6: Effects of current on the elastic modulus of cubic samples at a strain amplitude of 5% with varying frequencies - Kelvin Voigt comparison (a) Cube MRE 20mm (b) Cube MRE 30mm (c) Cube MRF-MRE 30mm (d) Cube MRF-E 20mm

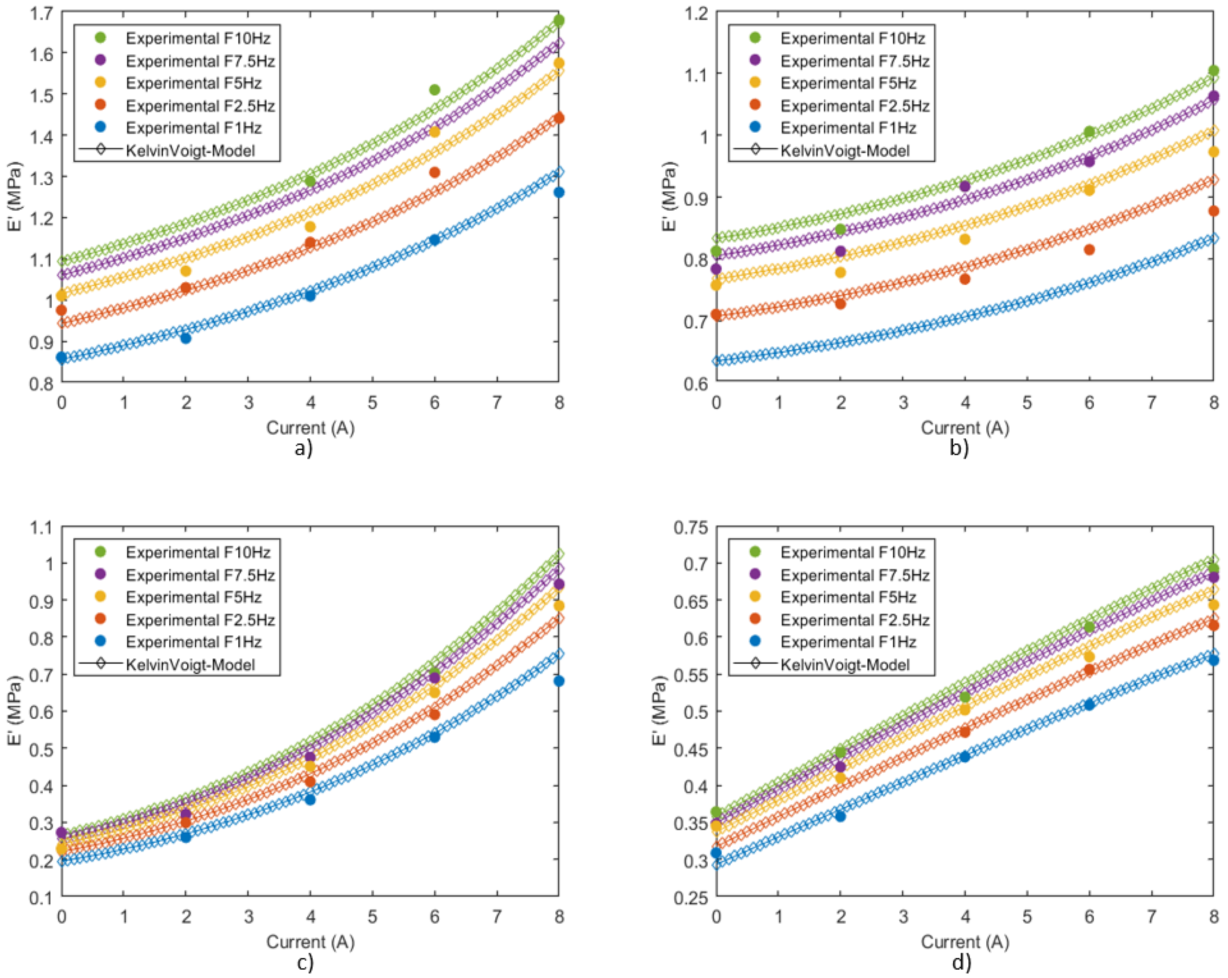

Figure 4.7: Effects of current on the elastic modulus of cylindrical samples at a strain amplitude of 5% with varying frequencies - Kelvin Voigt comparison (a) Cylinder MRE 20mm (b) Cylinder MRE 30mm (c) Cylinder MRF-MRE 30mm (d) Cylinder MRF-E 20mm

Examination of results in Figure 4.2 to Figure 4.7 generally show that the proposed model for elastic modulus can reasonably predict the variation of storage modulus with respect to the excitation frequency, strain amplitude and applied current for all MR samples investigated in this study. The model can accurately capture the strain-rate stiffening and strain-softening effects with minimal error, as well as accurately representing the influence of magnetic field and current on the modulus of the various MR samples.

To further validate these results, in the following section, quantitative analysis is conducted to evaluate the accuracy of the model.

4.4 Model Verification

To portray the performance of the modified Kelvin-Voigt model, the stress-strain hysteresis responses of different MR samples under compression oscillation are plotted and compared using the measured and predicted moduli. It is noted that there are three levels for strain (2.5%, 5%, and 10%) five levels for motion frequency (1 Hz, 2.5 Hz, 5 Hz, 7.5 Hz, and 10 Hz), and five levels of applied current (0 A, 2 A, 4 A, 6 A, and 8 A) that were utilized in modeling procedure. In total, 75 sets of experimental data are prepared for each sample as stress-strain hysteresis loops. As an example, Figure 4.8 shows the comparison between the measured and predicted stress-strain hysteresis responses under varying current at given frequency of 7.5 Hz and strain amplitude of 5% for three types of MR samples using Eqn. 4.2. As it can be realized, the model's estimation is fitted quite well to the measured results. Effects such as the increase in the area of hysteresis loops and the increase in the slope by increasing current is well predicted by the proposed model. The results suggest that the presented viscoelastic model can reasonably predict the stress-strain hysteresis over wide ranges of strain amplitudes, excitation frequencies and magnetic flux densities.

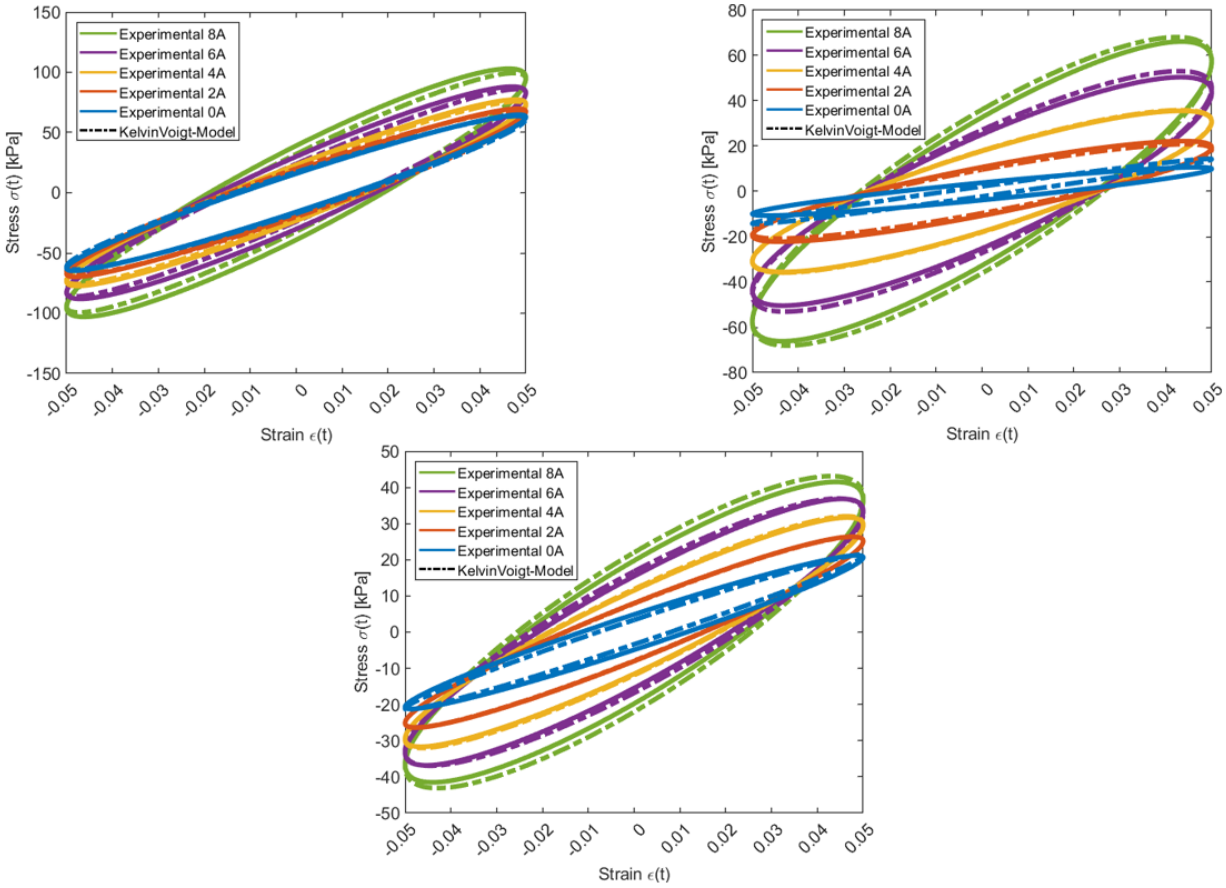

Figure 4.8: Measured vs. Kelvin Voigt modelled stress-strain hysteresis with varying current of 3 different sample types (a) Cube MRE 20mm (b) Cube MRF-MRE 30mm (c) Cube MRF-E 20mm (f=7.5 Hz. ε_0=5%)

To quantitatively evaluate the accuracy of the model, the normalized root mean square function (also known as coefficient of determination) is conducted on all experimental cases and their respective values over all range of currents, frequencies, and displacement amplitudes, are conducted. The normalized root mean square function is carried out to compute the fitness value through the following equation, where σ_{model} represents the model stress and σ_{exp} represents the experimental stress:

$$Fitness\ Value\ (\%) = 100 * \left[1 - \frac{norm(\sigma_{model} - \sigma_{exp})}{norm\left(\sigma_{exp} - mean(\sigma_{exp})\right)}\right] \tag{4.14}$$

It is noted that the fitness value or coefficient of determination ranges from 0 to 100%, where 100% signifies a perfect fit. Using Equation 4.14, the fitness values of the MRF-MRE are provided in Table 4.3 and Table 4.4 while those for the rest of the samples can be found in the Appendix B.

Table 4.3: Fitness value of the proposed model for the Cylinder MRF-MRE 30mm sample

Cylinder MRF-MRE 30mm			
Freq. (Hz)	$\varepsilon_0 = 2.5\%$	$\varepsilon_0 = 5\%$	$\varepsilon_0 = 10\%$
Current = 0A			
1	95.40	-	-
2.5	96.67	-	-
5	-	-	-
7.5	-	-	-
10	-	-	-
Current = 2A			
1	92.40	95.63	-
2.5	88.52	88.52	-
5	-	-	-
7.5	90.74	91.32	-
10	-	-	-
Current = 4A			
1	90.08	92.97	87.64
2.5	89.60	90.20	89.68
5	97.08	95.80	94.80
7.5	88.56	89.36	-
10	-	-	-
Current = 6A			
1	93.96	92.57	89.88
2.5	95.50	95.29	91.87
5	91.27	82.71	91.92
7.5	89.65	95.92	-
10	-	-	-
Current = 8A			
1	96.76	88.27	94.87
2.5	89.83	-	90.92
5	93.33	94.78	93.55
7.5	93.87	88.40	95.19
10	-	-	95.86

Table 4.4: Fitness value of the proposed model for the Cube MRF-MRE 30mm sample

Cube MRF-MRE 30mm			
Freq. (Hz)	$\varepsilon_0 = 2.5\%$	$\varepsilon_0 = 5\%$	$\varepsilon_0 = 10\%$
Current = 0A			
1	84.37	-	-
2.5	78.55	-	-
5	-	-	-
7.5	-	-	-
10	-	-	-
Current = 2A			
1	81.58	91.23	-
2.5	92.20	-	-
5	-	-	-
7.5	-	93.09	84.48
10	-	-	-
Current = 4A			
1	95.21	87.43	92.11
2.5	89.93	90.47	94.25
5	90.65	88.31	96.35
7.5	-	99.22	95.03
10	-	-	92.48
Current = 6A			
1	96.99	89.86	95.46
2.5	95.25	94.06	89.14
5	-	90.06	89.93
7.5	-	94.82	94.07
10	-	98.09	90.13
Current = 8A			
1	96.52	96.88	96.12
2.5	98.37	92.61	85.53
5	98.79	92.52	86.49
7.5	-	94.97	91.20
10	-	98.13	84.88

Out of the usable experimental cases for the cylindrical sample, the fitness value ranges from 81% to 99% and the average of fitness value is around 92%. While for the cubic sample, the range of fitness value is from 80% to 99% and the average of fitness value is 89%. Referring to Table 4.3 and Table 4.4, and data provided in the Appendix B, it becomes apparent that the model accuracy is low when the loading conditions (frequency and applied current) are close to their minimum values. Table 4.5 summarizes the minimum, maximum, and average fitness values across all the samples.

Table 4.5: Fitness value results summarized across all samples

Sample	Min. Fitness Value (%)	Max Fitness Value (%)	Avg. Fitness Value (%)
Cube MRE 20mm	88.88	99.56	95.26
Cube MRE 30mm	89.86	99.58	95.6
Cube MRF-MRE 30mm	78.55	97.07	91.59
Cube MRF-E 20mm	80.5	99.64	89.21
Cylinder MRE 20mm	81.2	99.28	93.12
Cylinder MRE 30mm	89.37	99.33	94.91
Cylinder MRF-MRE 30mm	82.71	99.22	92
Cylinder MRF-E 20mm	68.84	98.28	85.94

Considering Table 4.5, the phenomenological model seems to perform the best for the MRE samples, as fitness values consistently stay above 90% while MRF-Es performed the worst, likely due to discrepancies in the loss modulus from experimental error and nonlinearities.

To further evaluate the performance of the model, the percentage error between the measured and predicted elastic modulus is evaluated for each sample at each individual loading condition increment and provided in Appendix C. The minimum, maximum, and average percentage error between the proposed model and measured elastic modulus for all samples are summarized and provided in Table 4.6.

Table 4.6: The minimum, maximum, and average percentage error between the proposed model and measured elastic modulus for all samples

Sample	Min. % Error	Max % Error	Avg. % Error
Cube MRE 20mm	0.029	8.075	1.961
Cube MRE 30mm	0.04	6.506	1.87
Cube MRF-MRE 30mm	0.062	17.724	4.015
Cube MRF-E 20mm	0.012	11.86	2.314
Cylinder MRE 20mm	0.0041	7.94	2.19
Cylinder MRE 30mm	0.085	5.84	1.6
Cylinder MRF-MRE 30mm	0.0714	13.04	4.23
Cylinder MRF-E 20mm	0.088	8.51	2.09

From Table 4.6, it is apparent that the proposed model can predict the elastic modulus relatively well as the average error across all the MR samples is below 5%. The highest accuracy is observed for MREs, closely followed by the MRF-Es.

4.5 Summary

The modified Kelvin-Voigt model was formulated for predicting the viscoelastic storage and loss moduli of the MREs, MRF-Es, and MRF-MREs across a wide range of shapes, frequencies, strain amplitudes, and currents. The measured data was used to identify the parameters of the model by minimization of an error function between the model and measured responses.

In this process, it is to be noted that several other models were employed. Among them, a modified version of the four-parameter fractional derivative Zener model was attempted due to its solid theoretical basis and its relation to the general fractional derivative constitutive equation of viscoelastic materials. In addition, the model has successfully been fitted to experimental data on a wide variety of materials, especially polymers for vibration damping [52-54]. Additionally, several custom models based on the multiplicative split of the moduli into separate frequency dependent, current dependent, and strain amplitude dependent equations were attempted. However, with the identified parameters, it became apparent that the modified Kelvin-Voigt model greatly outperformed other models.

Verification of the model was carried out by calculating the stress response using the model and measured moduli. Results suggest that the model can capture the behaviour of all the samples in an accurate and simple manner. The normalized root mean square was considered as the criterion to investigate the goodness of fit, which was in the order of 90% across all the samples, showing good agreements between the measured and model responses. The average percentage error retrieved between the model and the measured elastic modulus data was below 5% for all samples. Since the measured loss modulus was largely ignored, the accuracy of the estimated loss modulus was not able to be verified within isolation.

Due to issues with nonlinearities and experimental errors, several elastic modulus data were not able to be used. For example, many samples had issues at a strain amplitude of 15% as the elastic modulus did not conform to the relationship of strain-softening.

Chapter 5: Development of a MR Based Semi-Active System

5.1 Introduction

As discussed in Chapter 1, a common application of MREs is their integration into a base vibration isolator system. Their unique field-dependent elastic modulus allows for the shifting of the natural frequency of an isolator, providing a unique opportunity to control vibrations across a broad range of frequencies. In this chapter, the magnetic cell utilized before for characterization of MR materials is effectively used as the vibration isolator system. The system has been molded as a single degree of freedom (SDOF) system to formulate the transmissibility using the developed model for the elastic modulus.

5.2 Conceptualization of an MRE Based Isolator

In order to further assess the vibration performance of the MR samples, a simplified representation of a SDOF MRE based isolator system is conceptualized as shown Figure 5.1. The system comprises of a payload mass and a field-dependent viscoelastic component representing MR materials.

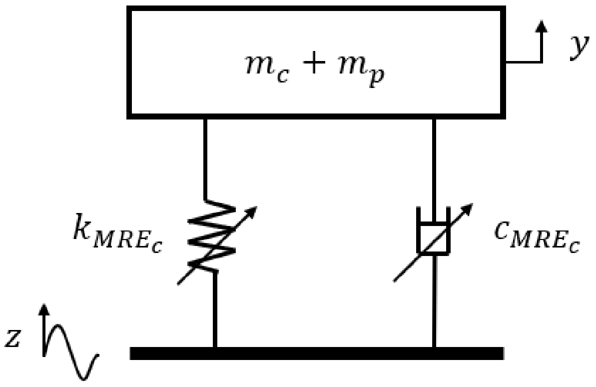

Figure 5.1: Basic model of MRE-based vibration isolator (vertical direction)

In Figure 5.1, m_c represents the mass of the upper section of the electromagnetic core, and m_p represents the payload mass attached on top. k_{MRE}, and c_{MRE} represent the stiffness and damping coefficient of the MR materials, respectively. Considering a harmonic base excitation of ($y = Ysin\omega t$), the giving differential equation of the motion can be derived as [55]:

$$\left(m_c + m_p\right)\ddot{y} + c_{MRE}\dot{y} + k_{MRE}y = k_{MRE}z + c_{MRE}\dot{z} \tag{5.1}$$

where $\ddot{y}$, $\dot{y}$, and y are the vertical acceleration, velocity, and displacement responses of the active mass, respectively. To assess the vibration attenuation performance of the MR based adaptive system, the displacement transmissibility which is the ratio of the response between the active mass and the base displacements can be obtained as:

$$\frac{Y}{Z} = \sqrt{\frac{k_{MRE}^2 + (c_{MRE}\omega)^2}{(k_{MRE} - m\omega^2)^2 + (c_{MRE}\omega)^2}} \tag{5.2}$$

where *m* represents total active mass, including the payload mass (m_p) and mass of core (m_c), and ω is the expiation angular frequency in rad/s.

The equivalent stiffness, k_{MRE}, and damping, c_{MRE}, in Equation 5.2 can be obtained using the following relations for the MR samples under compressive loading [56]:

$$k_{MRE} = \frac{E'(f, I)A_{MRE}}{l_{MRE}} \tag{5.3}$$

$$c_{MRE} = \frac{E''(f, I)A_{MRE}}{2\pi f l_{MRE}} \tag{5.4}$$

It is to note, both the elastic and loss moduli are assumed to be dependent only on the current and frequency and independent of strain amplitude assuming the MR material operates in linear viscoelastic region (strain amplitude is set at 2.5%). Therefore, the elastic and loss moduli in the modified Kelvin-Voigt model, as presented in Chapter 4 and to be utilized in Eqs. (5.3) and (5.4), can be summarized as follows:

$$\begin{cases} E'(f,I)_{\varepsilon_0=2.5\%} = (\beta_1' I^2 + \beta_2' I + \beta_3')\left(\frac{f}{f_0}\right)^{b} 0.025^{(\beta_4' I + \beta_5')} \\ E''(f,I)_{\varepsilon_0=2.5\%} = (\beta_1'' I^2 + \beta_2'' I + \beta_3'')\left(\frac{f}{f_0}\right)^{1+e} \left(e^{-0.025\beta_4''}\right) \end{cases} \tag{5.5}$$

5.3 Vibration Attenuation Performance

With the parameters retrieved from Chapter 4, the transmissibility response of the MR isolator is assessed using Eq. 5.2 combined with Eqs. (5.3 - 5.5) by varying the current in increment of 2A ranging from 0 to 8 A and excitation frequency ranging from 1 to 60 Hz. Furthermore, a total mass ($m_t = m_c + m_p$) of 7.30 kg was used as the active mass. Results for transmissibility for cubic and cylindrical MR samples under varied applied current are provided in Figure 5.2 and Figure 5.3, respectively.

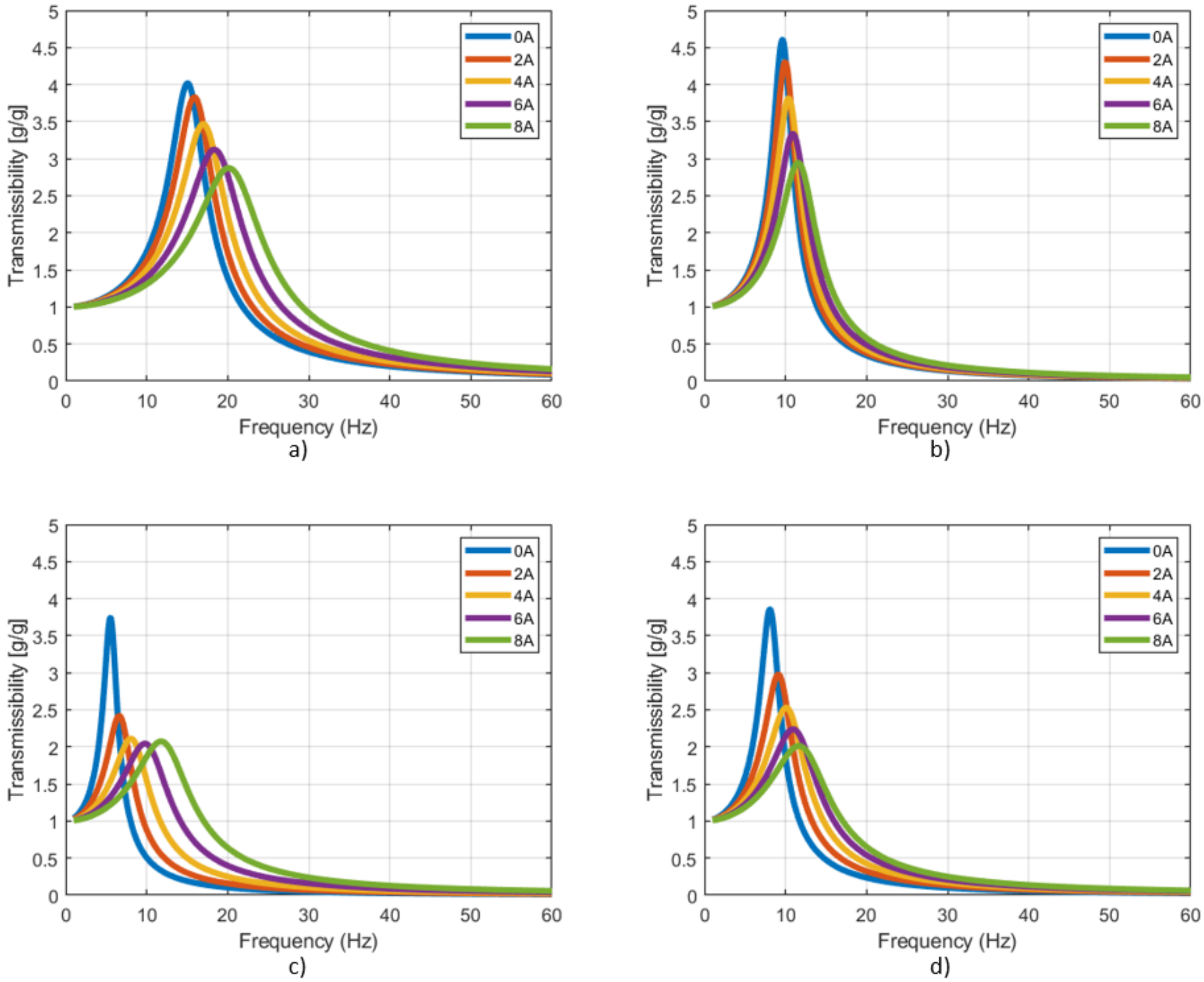

Figure 5.2: Model transmissibility across various currents for cubic samples (a) Cube MRE 20mm (b) Cube MRE 30mm (c) Cube MRF-MRE 30mm (d) Cube MRF-E 20mm

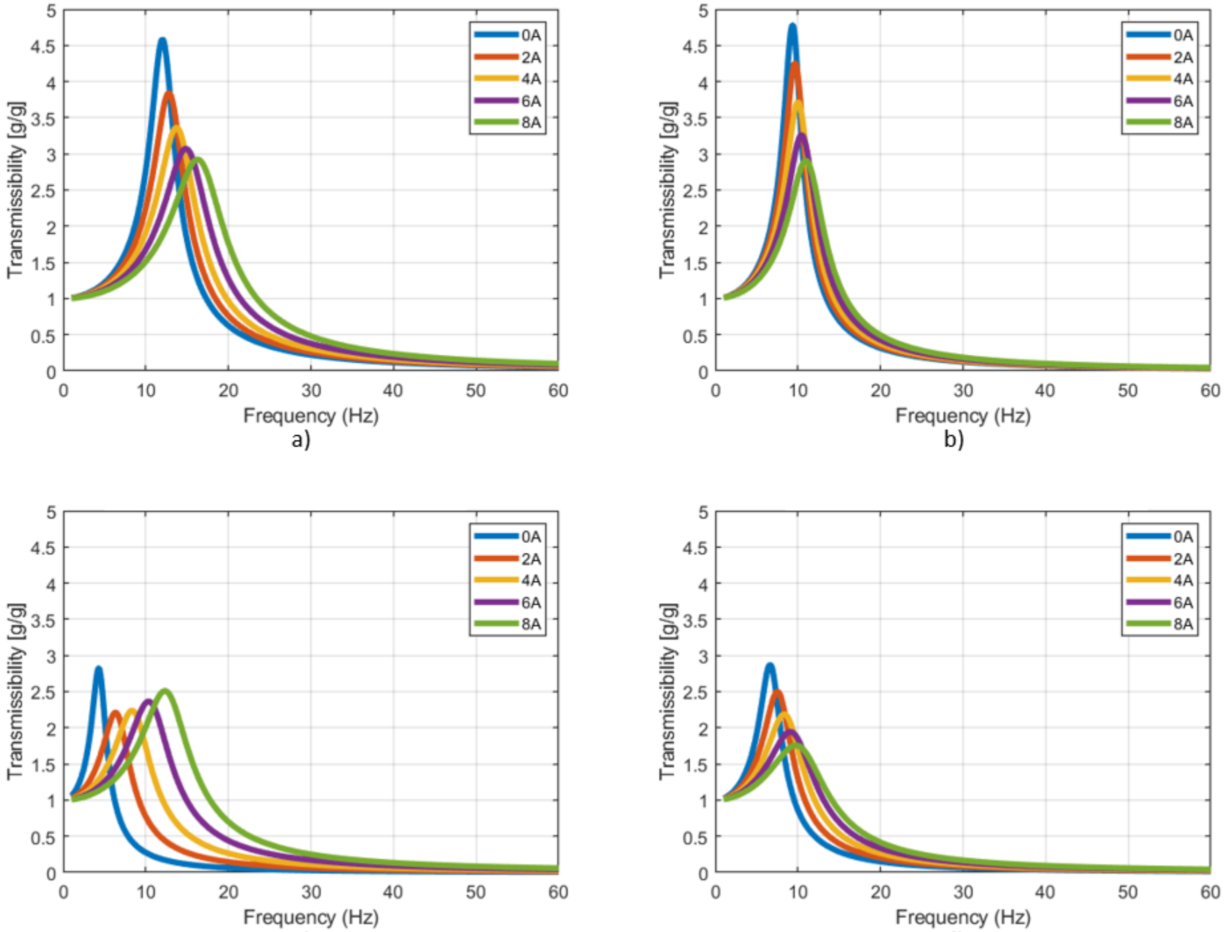

a) b) c) d)

Figure 5.3: Model transmissibility across various currents for cylindrical samples (a) Cylinder MRE 20mm (b) Cylinder MRE 30mm (c) Cylinder MRF-MRE 30mm (d) Cylinder MRF-E 20mm

Figure 5.2 and Figure 5.3 clearly show, the shift in natural frequency of the MR based vibration isolator by increasing the applied current, irrespective of sample type. Table 5.1 summarizes the % shift in natural frequency (f_n) across the MR samples for ease of comparison.

Table 5.1: Summary of natural frequency and its shift at the maximum current (8A) across all samples

Sample	**Static f_n (Hz)**	**Absolute f_n Shift (Hz)**	**Relative f_n Shift (%)**
Cube MRE 20mm	15.1	20.1 - 15.1 = 5	33.11
Cube MRE 30mm	9.6	11.6 – 9.6 = 2	20.83
Cube MRF-MRE 30mm	4.3	12.3 – 4.3 = 8	186
Cube MRF-E 20mm	8.1	11.7 – 8.1 = 3.6	40.96
Cylinder MRE 20mm	12	16.4 - 12 = 4.4	36.6
Cylinder MRE 30mm	9.3	11.1 - 9.3 = 1.8	19.35
Cylinder MRF-MRE 30mm	5.5	11.8 - 5.5 = 6.3	114.54
Cylinder MRF-E 20mm	6.6	9.8 – 6.6 = 3.2	48.48

Examination of results in Table 5.1 show that as expected MRF-MRE samples with cube and cylindrical shape provide the highest percentage shift of nearly 186% and 115%, respectively. Results also show that increasing the shape factor results in higher percentage shift in the natural frequency. For instance, by increasing the shape factor for cylindrical MRE from 0.25 to 0.375, the shift in natural frequency increases from nearly 19% to 37%.

A shaker test was also conducted on an equivalent SDOF system using the same housing unit from the MTS characterization experiment in Chapter 3. Figure 5.4 shows the experimental setup used to estimate the natural frequency of the MRE 30mm Cylinder and Cube samples. The magnetic cell is secured to the shaker table and has a total active mass of 7.30 kg (2.34 kg from the upper section of the housing unit and 4.96 kg from the bottom section of the housing unit with the coil). With this mass, it was possible to apply a pre-strain of approximately 40% to the MRE samples, consistent with the pre-strain applied in the MTS experiments. This was done by measuring the samples original height and comparing it to its compressed height between the bottom and upper section of the housing unit when the payload mass was placed.

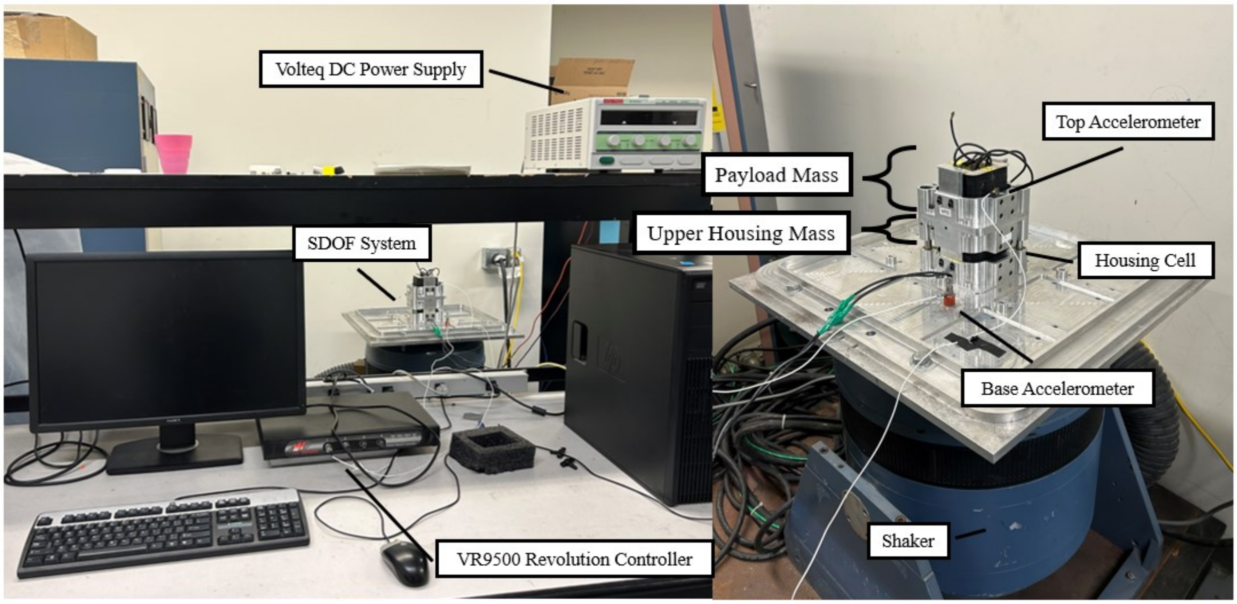

Figure 5.4: Shaker test SDOF experimental setup

The magnetic cell is then excited with a random wide band-limited noise test from 0.5 Hz to 60 Hz with a constant magnitude of 0.0375G RMS. The electromagnet coil is connected to a DC power supply (Volteq HY10416EX) to generate the required magnetic field in the MRE region. During the test, the current was increased in increments of two, starting from 0A and reaching to 4A (0A, 2A, 4A), as problems were encountered beyond this range due to excitation of other modes likely associated with slight unavoidable misalignment of the component. Moreover, at a current above 6A concerns arose regarding overheating the electromagnet, given that the experiment time for one test could extend to nearly 5 minutes or more. Therefore, the data retrieved at 6A and 8A currents were ultimately removed to maintain reputable results. The input signal sent to the shaker is generated using VR9500 Revolution Controller along with the VibrationVIEW software. To measure the system response, two accelerometers are placed, one on the base of the system and one on top of the active mass. The accelerometers used are Bruel & Kjær 4393 charge-type accelerometers. Using the signal retrieved from each accelerometer, the transmissibility of the samples was retrieved using the H2 transfer function. The test for the selected currents was conducted three times to ensure consistency and repeatability, and the results were subsequently averaged. Figure 5.5 shows the experimental transmissibility of the adaptive vibration isolator integrating cube MRE 30mm and cylinder MRE 30mm samples.

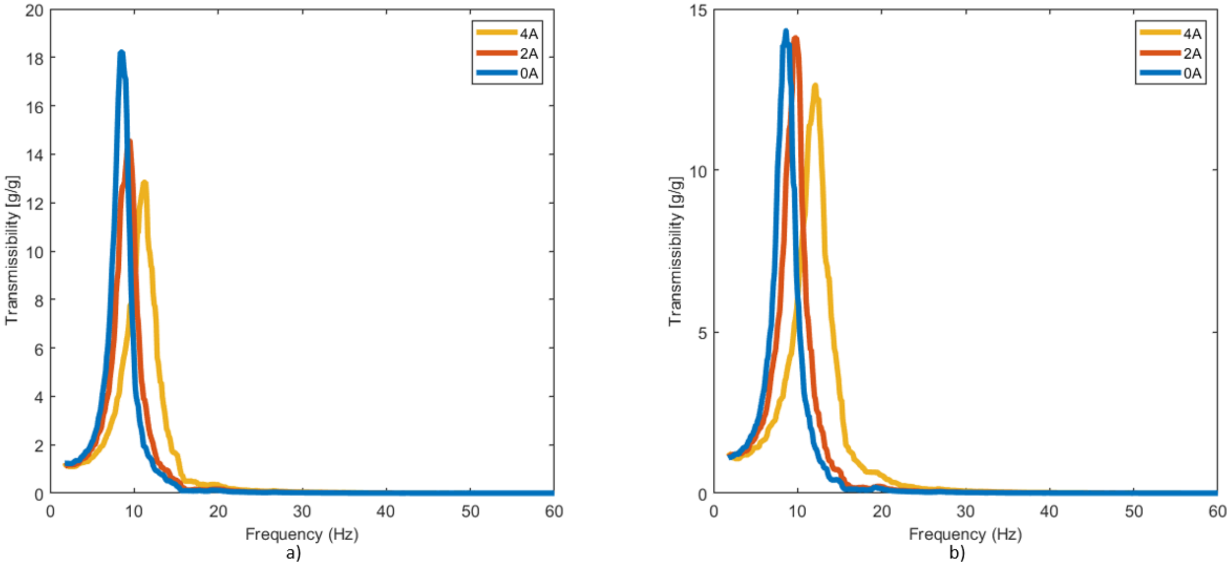

a)

b)

Figure 5.5: Experiment transmissibility at 0.0375G RMS (a) Cube MRE 30mm (b) Cylinder MRE 30mm

Observations show that when the current is applied to electromagnet, the system's natural frequency increases and the magnitude of the transmissibility decreases which is due to the increase and decrease in the sample's stiffness and damping, respectively. A summary of the percent error in natural frequency between the experiment and simulated results are provided in Table 5.2 and Table 5.3 for cubic and cylindrical samples, respectively.

Table 5.2: Comparison of the natural frequency between experiment and model – Cube MRE 30mm

Current	Experimental f_n	Simulation f_n	Percent Error
0A	8.75	9.6	9.7%
2A	9.625	10	3.8%
4A	12.375	10.4	15.95%

Table 5.3: Comparison of the natural frequency between experiment and model – Cylinder MRE 30mm

Current	Experimental f_n	Simulation f_n	Percent Error
0A	8.5	9.3	8.6%
2A	9.375	9.6	2.4%
4A	11.375	10	12.08%

It can be realized that error is generally less than 15% which is acceptable considering many uncertainties in modeling of MR samples, experimental error and idealized SDOF system.

5.4 Summary

The proposed modified Kelvin-Voigt model was effectively utilized to conceptualize an ideal SDOF MR isolator system. The governing differential equation of the system is first derived and then used to formulate the transmissibility function. The transmissibility of MR samples was evaluated across a frequency range of 1 to 60 Hz. The resulting frequency response functions demonstrated the magnetic stiffening effect of the MR samples and further displayed relationships discussed in Chapter 3. To verify the results, two samples (Cube MRE 30mm & Cylinder MRE 30mm) were placed in a similar SDOF system experiment setup. Using a shaker table and accelerometers, the system was excited with a band-limited random test. The resulting FRF showed similarities to the model, specifically, below the 2A range, where the natural frequencies were within reasonable error. However, beyond 2A, the shifting abilities of the MR samples were underestimated.

Possible reasons of error can be attributed to a combination of errors from the housing unit, experimental error and simplification made in modeling. During experimentation, it was found that the housing unit was very dependent on the size and shape of payload mass. Due to its design, which features two supporting rods on opposing corners, the upper part of the cell became unstable if a mass of significant width was used. Eventually, when the lower section of another housing unit was used as a mass, the system became substantially more stable. However, the existence of slight misalignment would likely excite unwanted bending and possibly twisting modes. Nevertheless, the results presented remain grounded and insightful.

Chapter 6: Contributions, Conclusions and Recommendations

6.1 Major Contributions

The main focus of this research was to provide an in-depth investigation on the magneto-mechanical characteristics of a new class of smart materials, magnetorheological fluid encapsulated within a MRE (MRF-MRE). The key contributions are as follows:

- Development of a repeatable and simple fabrication process for eight different samples.
- Design and manufacturing of eight MR samples containing different shapes and heights.
- Design of an experimental setup for static and dynamic characterization in the compression mode under various loading conditions and sample types.
- Formulation of a phenomenological model for estimating the elastic and loss moduli of each MR sample under varying loading conditions.
- Idealized a single-degree-of-freedom system to estimate the transmissibility of each sample using the developed phenomenological model and design of a test to validate the shift in natural frequency.

6.2 Major Conclusions

This dissertation research presents nonlinear stress-strain characteristics of several magnetorheological materials, including new hybrid MREs, as well as the modeling of their moduli using a modified Kelvin-Voigt model. Major conclusions drawn from the research are as follows:

- The shape factor of a sample has major influence on its mechanical and magnetic properties. Reducing the sample height resulted in an increase in the stiffness of an MR sample, while simultaneously enhancing its MR effect.
- The shape of a sample impacts solely the sample's stiffness for MREs and MRF-Es, however, for MRF-MREs it was found to substantially increases its MR effect. Two shapes with equal shape factor and volume fraction were presented in this study, cubic and cylindrical. Due to an increase in contact surface area, the cubic sample was consistently shown to have a higher stiffness or elastic modulus than its cylindrical counter part. Unique to MRF-MREs, when the current was increased the effect of shape was enhanced as the sample became stiffer, therefore, this allowed for the cubic sample to create a much higher MR effect over the cylindrical sample.
- Owing to their viscoelastic nature, the MR samples exhibit significant hysteresis in their stress-strain responses. The enclosed area and the slope of the major axis of the hysteresis loops are highly dependent on the loading frequency, strain amplitude as well as the applied current. The strain softening, strain rate stiffening and the magnetic field stiffening phenomena are identified as the nonlinear hysteresis properties of the MR samples.
- A relative increase of up to 478% in the elastic compression modulus of the new MRF-MRE hybrid sample was observed. This is found to be significant increase in contrast to the other sample types, at similar loading conditions. For instance, the MRF-E exhibited only an increase of 100%. It is possible to conclude that the addition of a MRE to encapsulate the fluid provides the greatest MR effect.
- The proposed modified Kelvin-Voigt model reasonably predicted the measured moduli retrieved from the stress-strain hysteresis loops. The coefficient of determination between

the measured and model elastic modulus was found to have an average percent error of less than 5% across all the samples. Furthermore, the goodness of fit between hysteresis was found to be upwards of 90%, suggesting the model's effectiveness.

- The formulated single-degree-of-freedom spring damper system based on the proposed modified Kelvin-Voigt model was also able to effectively show that the hybrid MRF-MRE sample has the most optimal magnetic shifting properties for a vibration isolation system.

6.3 Recommendations for Future Work

Given the extensive scope of this study and unexpected challenges encountered, there are still many areas that could provide additional insight on the proposed hybrid MRF-MRE. Some of the recommendations to be further investigated are listed below:

- Investigate further the differences between MRF-E and MRF-MRE. Unfortunately, in the process of this research, it was not possible to compare an MRF-E and MRF-MRE of the same shape factor. As concluded, the height of a sample has significant impact on the MR effect and overall stiffness of a sample. Therefore, having the two samples be the same size can help draw further conclusions.
- Perform characterization of the hybrid samples in shear mode to acquire in-depth understanding of their behaviour in the other operation mode.
- Investigate other important parameters that can influence the hybrid sample's magnetic properties, such as, pre-strain, volume fraction of ferromagnetic particles, wall thickness, etc.
- Explore the behaviour of MRF-Es and MRF-MRE in a vibration isolation experimental test.

References

[1] A. Bastola, M. Paudel and W. Li, "Recent Progress of Magnetorheological Elastomers: A Review," *Smart Materials and Structures,* vol. 29, no. 12, 2020.

[2] V. Chaunhan, A. Kumar and R. Sham, "Magnetorheological fluids: A comprehensive review," *Manufacturing Review,* vol. 11, 2024.

[3] M. Kallio, "The Elastic and Damping Properties of Magnetorheological Elastomers," VTT Publications, 2005.

[4] H. Vatandoost, "Fabrication and Modeling of Magnetorheological Elastomer (MRE)," Shahrood University of Technology, 2015.

[5] H. Eshgarf, A. A. Nadooshan and A. Raisi, "An Overview on Properties and Applications of Magnetorheological Fluids: Dampers, Batteries, Valves, and Brakes," *Journal of Energy Storage,* vol. 50, 2022.

[6] J. de Vincente, D. Klingeberg and R. Hidalgo-Alvarez, "Magnetorheological Fluids: A Review," *The Royal Society of Chemistry,* vol. Soft Matter, no. 7, pp. 3701-3710, 2011.

[7] M. Ashtiani, S. Hashemabadi and A. Ghaffari, "A Review on the Magnetorheological Fluid Preparation and Stabilization," *Journal of Magnetism and Magnetic Materials,* no. 374, pp. 716-730, 2015.

[8] L. Vekas, D. Bica, D. Gheorghe, I. Potencz and M. Rasa, "Concentration and Composition Dependence of the Rheological Behaviour of some Magnetic Fluids," *Journal of Magnetism and Magnetic Materials,* vol. 201, no. 1-3, pp. 156-162, 1999.

[9] D. Truong and K. Ahn, "MR Fluid Damper and Its Application to Force Sensorless Damping Control System," *Smart Actuation and Sensing Systems - Recent Advances and Future Challenges,* 2012.

[10] Q.-H. Nguyen and S.-B. Choi, "Optimal Design of MR Shock Absorber and Application to Vehicle Suspension," *Smart Materials and Structures,* vol. 18, no. 3, 2009.

[11] W.-M. Zhong, A.-D. Zhu, X.-X. Frank Bai, N. Werely and N. Zhang, "Integrated Shock Absorber With Both Tuneable and Inertance and Damping," *Frontiers in Materials,* vol. 7, no. 204, 2020.

[12] GM Authority, "General Motors Magnetic Ride Control Technology," Motrolix LLC, 2023. [Online]. Available: https://gmauthority.com/blog/gm/general-motors-technology/gm-chassis-suspension-technology/gm-magnetic-ride-control-technology/.

[13] D. Zhao, J. Zhao, Z. Zhao, Y. Liu, S. Liu and S. Wang, "Design and Experimental Study of the Porous Foam Metal Magnetorheological Fluid Damper Based on Built-In Multi-Pole Magnetic Core," *Journal of Intelligent Material Systems and Structures,* vol. 31, no. 5, pp. 687-703, 2020.

[14] H. Wang and C. Bi, "Study of a Magnetorheological Brake Under Compression-Shear Mode," *Smart Materials and Structures,* vol. 29, no. 1, 2019.

[15] N. Wang, L. Xinhua, G. Krolczyk, Z. Li and W. Li, "Effect of Temperature on the Transmission Characteristics of High-Torque Magnetorheological Brakes," *Smart Materials and Structures,* vol. 28, no. 5, 2019.

[16] S. S. Sun, D. H. Ning, J. Yang, H. Du, S. W. Zhang and W. H. Li, "A Seat Suspension with a Rotary Magnetorheological Damper for Heavy Duty Vehicles," *Smart Materials and Structures,* no. 25, 2016.

[17] D. C, H. G, V. S. Jebadurai, S. L, T. D and J. E. Christy, "A Review on the Magnetorheological Fluid, Damper and Its Applications for Seismic Mitigation," *Civil Engineering Journal,* vol. 4, no. 12, 2018.

[18] D. Cruze, H. Gladston, E. Farsangi, S. Loganathan, D. Tensing and S. Solomon, "Development of a Multiple Coil Megneto-Rheological Smart DAmper to Improve the Seismic Resilience of Building Structures," *The Open Civil Engineering Journal,* vol. 14, no. 78, pp. 78-93, 2020.

[19] G. Liu, F. Gao, D. Wang, Liao and Wei-Hsin, "Medical Applications of Mangeotrheological Fluid: A Systematic Review," *Smart Materials and Structures,* vol. 31, no. 4, 2022.

[20] H. Herr and A. Wilkenfeld, "User-Adaptive Control of a Magnetorheological Prosthetic Knee," *Industrial Robot: An International Journal,* vol. 30, no. 1, pp. 42-55, 2003.

[21] J. Kumar, P. Paul, G. Raghunathan and D. Alex, "A Review of Challenges and Solutions in the Preparation and Use of Magnetorheological Fluids," *International Journal of Mechanical and Materials Engineering,* vol. 14, 2019.

[22] I. Jang, H. Kim, J. Lee, H. Choi and M. Jhon, "Role of Organic Coating on Carbonyl Iron Suspended Particles in Magnetorheological Fluids," *Journal of Applied Physics,* vol. 97, no. 10, 2005.

[23] G. Iglesias, M. Lopez-Lopez, J. Duran, F. Gonzalez-Caballero and A. Delgado, "Dynamic Characterization of Extremely Bidisperse Magnetorheological Fluids," *Journal of Colloid and Interface Science,* vol. 377, no. 1, pp. 153-159, 2012.

[24] G. Schubert and P. Harrison, "Large-Strain Behaviour of Magneto-Rheological Elastomers Tested Under Uniaxial Compression and Tension, and Pure Shear Deformations," *Polymer Testing,* no. 42, pp. 122-134, 2015.

[25] S. Li, Y. Liang, Y. Li, J. Li and Y. Zhou, "Investigation of Dynamic Properties of Isotropic and Anisotropic Magnetorheological Elastomers with a Hybrid Magnet Sheat Test Rig," *Smart Materials and Structures,* vol. 29, no. 11, 2020.

[26] J. Puente-Cordova, M. E. Reyes-Melo, L. Palacios-Pineda, I. Martinez-Perales, O. Martinez-Romero and A. Elias-Zuniga, "Fabrication and Characterization of Isotropic and Anisotropic Magnetorheological Elastomers, Based on Silicone Rubber and Carbonyl Iron Microparticles," *Polymers,* vol. 10, no. 12, 2018.

[27] A. Dargahi, "Fabrication, Characterization, and Modeling of Magnetorheological Elastomers," Montreal, 2017.

[28] G. Susheelkumar, "Theoretical and Experimental Investigation of Model-Free Adaptive Fuzzy Sliding Mode Control for MRE Based Adaptive Tuned Vibration Absorber," *Smart Materials and Structures,* vol. 28, no. 4, 2019.

[29] Y. Li, J. Li, T. Tian and W. Li, "A Highly Adjustable Magnetorheological Elastomer Base Isolator for Applications of Real-Time Adaptive Control," *Smart Materials and Structures,* vol. 22, no. 9, 2013.

[30] B. Kavlicoglu, Y. Liu, B. Wallis, H. Sahin, M. McKee and F. Gordaninejad, "Two-Way Controllable Magnetorheological Elastomer Mount for Shock and Vibration Mitigation," *Smart Materials and Structures,* vol. 29, no. 2, 2020.

[31] S. Sun, "An Adaptive Tuned Vibration Absorber Based on Mulitlayered MR Elastomers," *Institue of Physics Publishing,* vol. 24, no. 4, 2015.

[32] W. M. Kiarie, "Design and Development of Magnetorheological Elastomers for Active Vibration Reduction in Vechiles," Iowa State University, 2021.

[33] H. Vatandoost, "Compression Mode Characterizations of Magnetorheological Elastomers," Montreal, 2020.

[34] A. Bostala, E. Ang, M. Paudel and L. Li, "Soft Hybrid Magnetorheological Elastomer: Gap Bridging Between MR Fluid and MR Elastomer," *Colloids and Surfaces,* vol. A, no. 583, 2019.

[35] A. Ali and A. Muthalif, "Dynamic Behavior Modelling of a Hybrid Magnetorheological Elastomer with Encapsulated fluid for Base Vibration Isolation," *European Journal of Mechanics,* no. 100, 2023.

[36] Z. Xing, M. Yu, S. Sun and W. Li, "A Hybrid Magnetorheological Elastomer-Fluid (MRE-F) Isolation Mount: Development and Experimental Validation," *Smart Materials and Structures,* vol. 25, no. 1, 2015.

[37] A. Bastola, L. Li and M. Paudel, "A Hybrid Magnetorheological Elastomer Developed by Encapsulation of Magnetorheological Fluid," *Journal of Material Science,* no. 53, pp. 7004-7016, 2018.

[38] A. Bastola, V. Hoang and L. Li, "A Novel Hybrid Magnetorheological Elastomer Developed by 3D Printing," *Materials and Design,* no. 114, pp. 391-397, 2017.

[39] X. Wang and F. Gordaninejad, "A New Magnetorheological Fluid-Elastomer Mount: Phenomenological Modeling and Experimental Study," *Smart Materials and Structures,* vol. 18, no. 9, 2009.

[40] W. Zhang, X. L. Gong, S. H. Xuan and Y. G. Xu, "High-Performance Hybrid Magnetorheological Materials: Preparation and Mechanical Properties," *Industrial & Engineering Chemistry Research,* vol. 49, no. 24, 2010.

[41] Y. Choi and N. Wereley, "Controllable Stress of Magnetorheological Fluid Elastomeric Encapsulations," *IEEE Transactions on Magnetics,* vol. 58, no. 2, 2022.

[42] R. Brown, Physical Testing of Rubber, Springer Sceince & Business Media Inc., 2006.

[43] "Exoflex 00-30," Smooth-On, [Online]. Available: https://www.smooth-on.com/products/ecoflex-00-30/.

[44] Basf Coporation, "Carbonyl Iron Powder (CIP)," 2024. [Online]. Available: https://aerospace.basf.com/carbonyl-iron-powder.html.

[45] "MRF-132DG Magneto-Rheological Fluid," Mid Atlantic Rubber, [Online]. Available: https://www.shoplordmr.com/mr-products/mrf-132dg-magneto-rheological-fluid-1-liter.

[46] A. C. Martins, "Design of An Experimental Apparatus for the Performance Evaluation of an Active Seat Cushion System," 2017.

[47] "Standard Guide for Dynamic Testing of Vulcanized Rubber and Rubber-Like Materials Using Vibratory Methods," ATSM D5992-96, 2011.

[48] R. H. Ewoldt, "Nonlinear Viscoelastic Materials: Bioinspired Applications and New Characterization Measures," Massachusetts Institute of Technology, Masssachusetts, 2009.

[49] H. Vatandoost, R. Sedaghati and S. Rakheja, "A New Method to Characterize the Nonlinear Magneto-Viscoelasticity Behavior of Magneto-Active Elastomers Under Large Amplitude Oscillatory Axial (LAOA) Loading," *Nonlinear Dynamics,* vol. 112, no. 5, pp. 3319-3356, 2024.

[50] International Strandards Organization, "ISO 4664-1: Rubber, vulcanized or themorplastic - Determination of dynamic properties - Part 1: General guidance," Geneva, 2011.

[51] A. Payne and R. Whittaker, "Low Strain Dynamic Properties of Filled Rubbers," *Rubber Chemistry and Technology,* vol. 44, no. 2, pp. 440-478, 1971.

[52] Z. Pawlak and A. Denesiewicz, "Identification of the Fractional Zener Model Parameters for a Viscoelastic Material over a Wide Range of Frequencies and Temperatures," *Materials ,* vol. 14, no. 22, 2021.

[53] T. Huu Ham, I. Petrikova and B. Marvalova, "Experimental Characterization and Viscoelastic Modeling of Isotropic and Anisotropic Magnetorheological Elastomers," *Polymer Testing,* vol. 81, 2020.

[54] R. Ma, M. Ni, Q. Chen, Y. Zhou and J. Han, "Viscoelastic Fractional Model Based on Harmonic Excitation," *Mathematical Problems in Engineering,* vol. 2022, no. 1, 2022.

[55] A. Jalali, H. Dianati, N. Mahmood, H. Vatandoost and M. Ghatee, "A Novel Bi-Directional Shear Mode Magneto-Rheological Elastomer Vibration Isolator," *Journal of Intellingent Material Systems and Structures,* vol. 31, no. 17, pp. 2002-2019, 2020.

[56] Y. Wany, H. Vatandoost and R. Sedaghati, "Development of a Novel Magneto-Rheological Elastomer-Based Semi-Active Seat Suspension System," *Vibration,* vol. 6, no. 4, 2023.

Appendix A

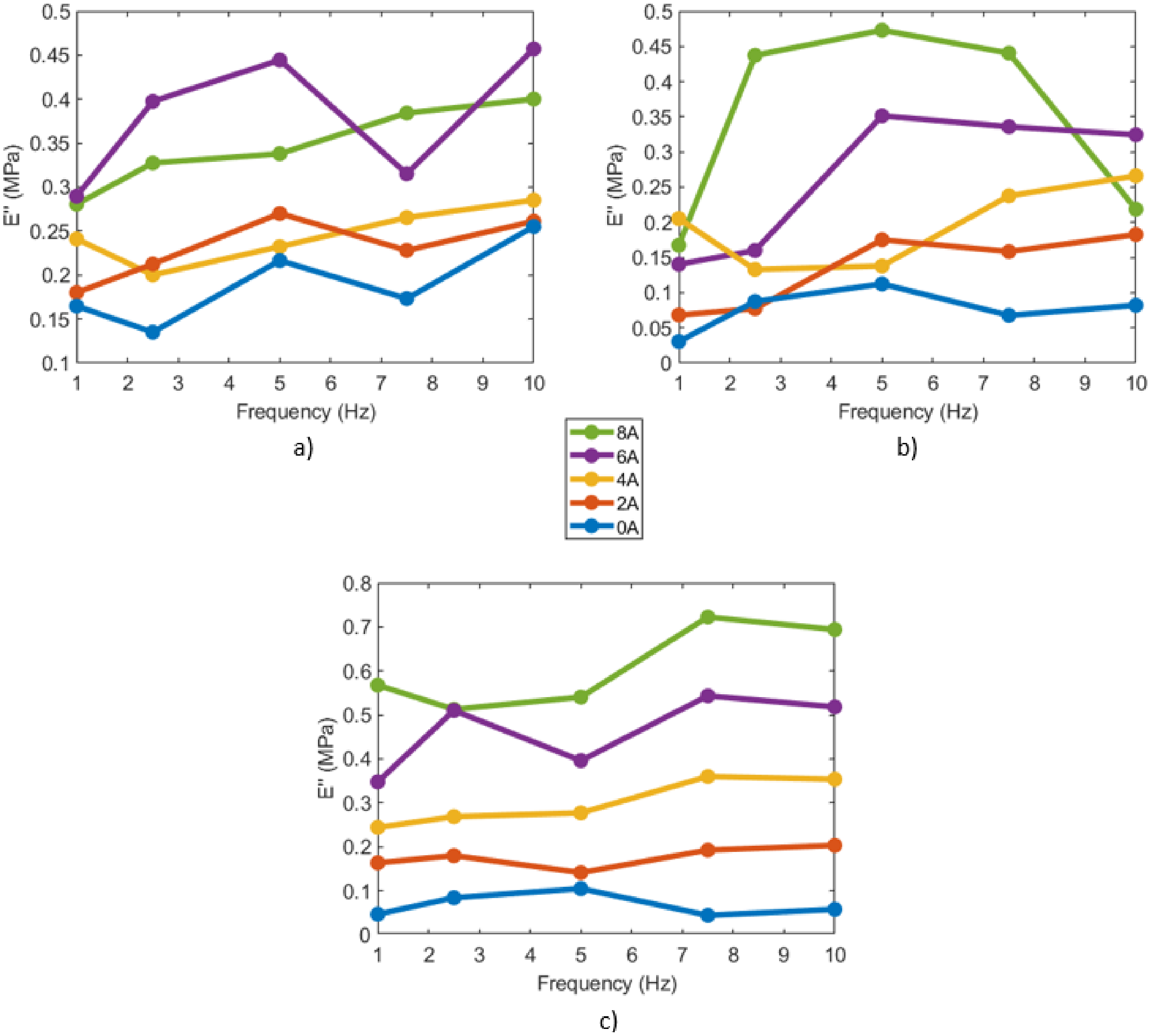

a)

b)

c)

Figure A.1: Effects of frequency on the loss modulus of 3 different MR sample types at a strain amplitude of 5% with varying currents (a) Cube MRE 30mm (b) Cube MRF-E 20mm (c) Cube MRF-MRE 30mm

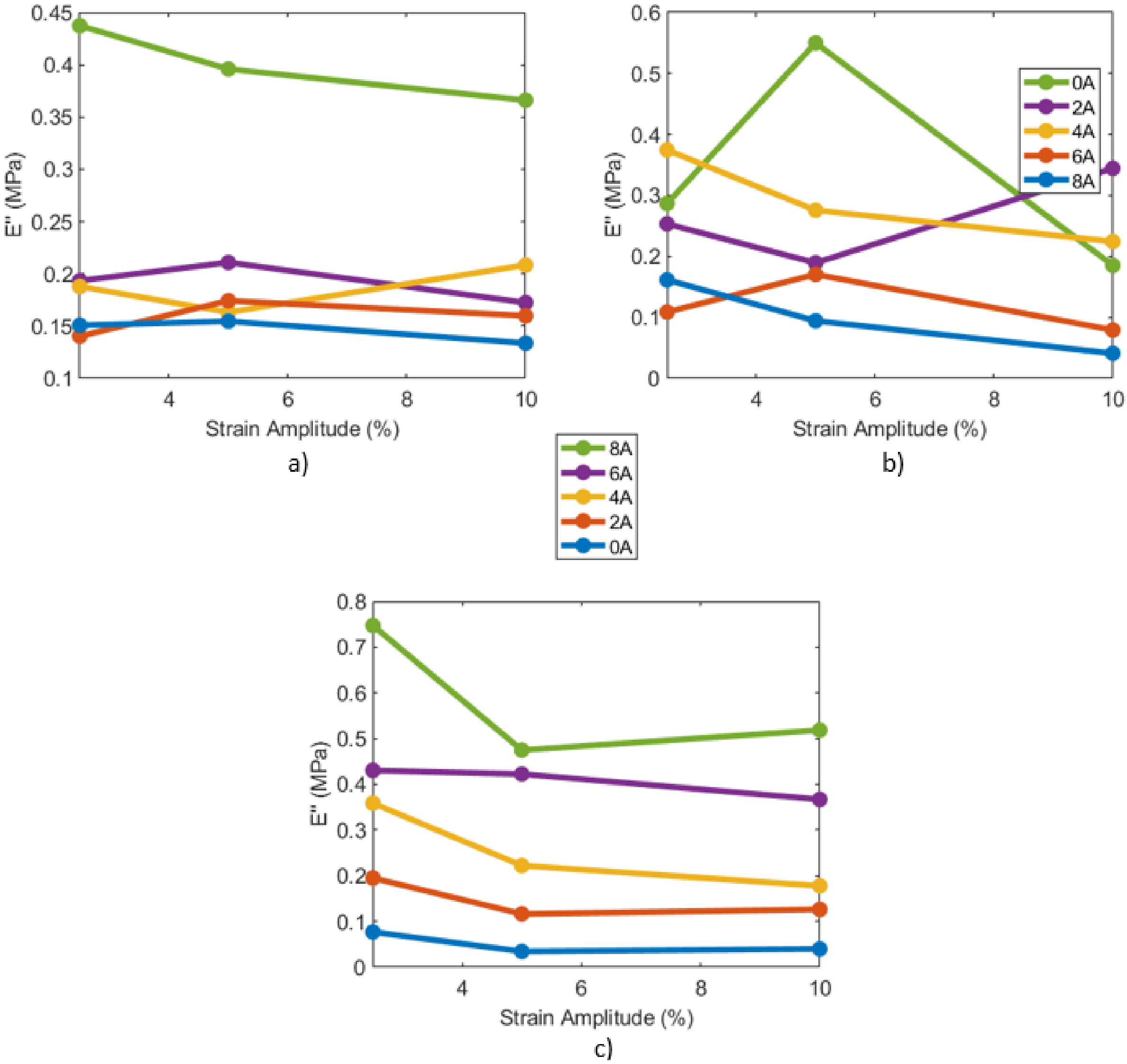

Figure A.2: Effects of strain amplitude on the loss modulus of 3 different sample types at 2.5 Hz with varying currents (a) Cylinder MRE 30mm (b) Cylinder MRF-E 20mm (c) Cylinder MRF-MRE 30mm

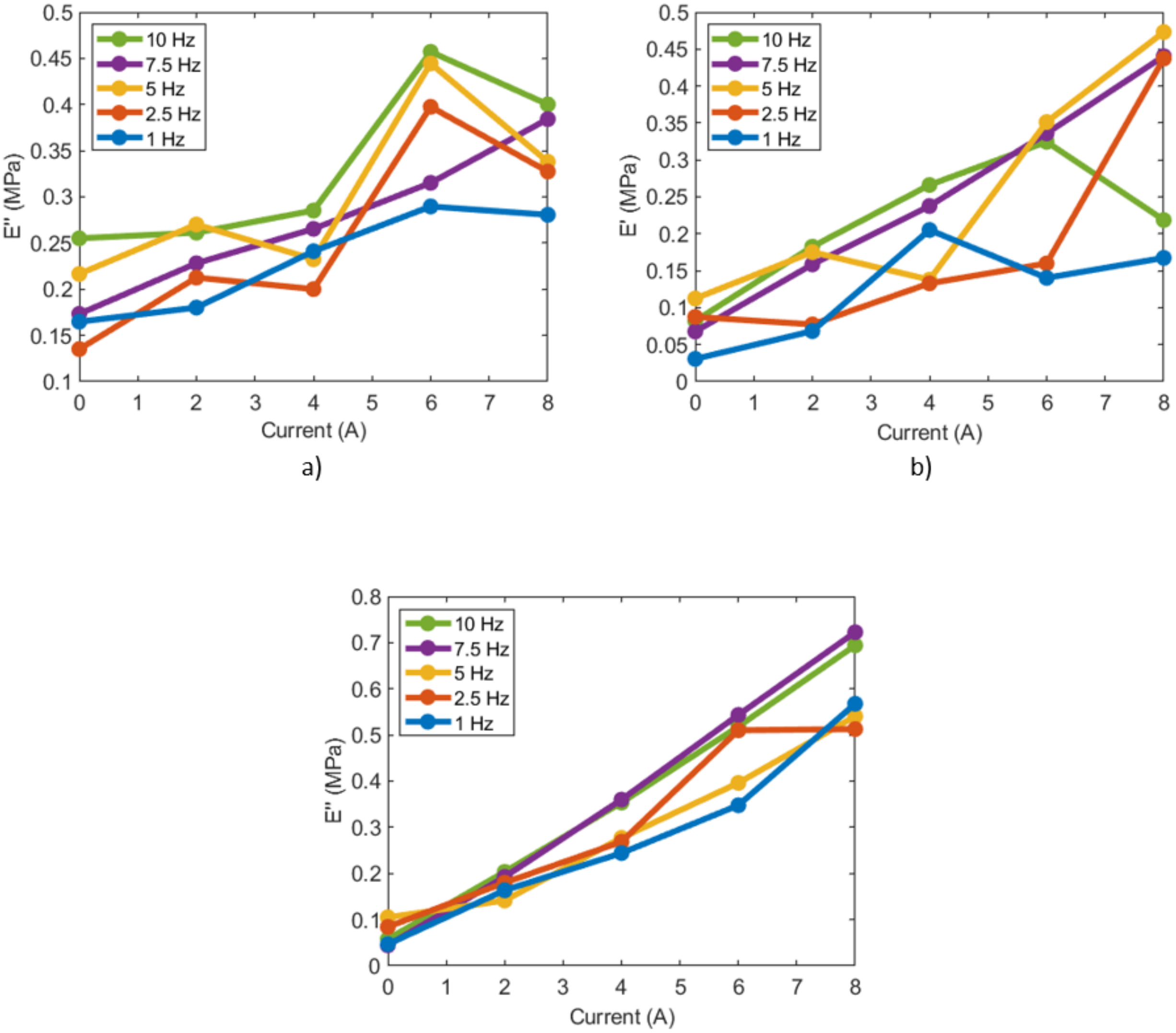

a)

b)

c)

Figure A.3: Effects of current on the loss modulus of 3 different sample types at a strain amplitude of 5% with varying frequencies (a) Cube MRE 30mm (b) Cube MRF-E 20mm (c) Cube MRF-MRE 30mm

Appendix B

Table B.1: Fitness value of the proposed model for the Cube MRE 20mm sample

Cube MRE 20mm			
Freq. (Hz)	$\boldsymbol{\varepsilon_0 = 2.5\%}$	$\boldsymbol{\varepsilon_0 = 5\%}$	$\boldsymbol{\varepsilon_0 = 10\%}$
Current = 0A			
1	95.34	93.41	92.08
2.5	91.90	98.52	97.03
5	95.02	99.56	98.39
7.5	97.75	97.04	95.30
10	94.70	95.63	98.00
Current = 2A			
1	93.80	93.63	92.48
2.5	96.05	98.65	97.43
5	97.32	94.03	98.39
7.5	91.14	96.40	97.36
10	96.27	95.51	95.68
Current = 4A			
1	91.93	97.01	93.39
2.5	97.16	96.10	95.21
5	98.75	96.21	96.25
7.5	94.19	97.61	97.01
10	95.64	95.35	96.04
Current = 6A			
1	95.54	93.55	94.12
2.5	89.66	95.49	93.02
5	96.70	94.91	93.60
7.5	96.58	92.94	93.46
10	97.35	95.68	97.95
Current = 8A			
1	95.56	92.51	94.57
2.5	96.99	93.51	88.88
5	91.15	92.31	92.22
7.5	93.75	92.95	95.83
10	95.44	98.58	97.92

Table B.2: Fitness value of the proposed model for the Cube MRE 30mm sample

Cube MRE 30mm			
Freq. (Hz)	$\boldsymbol{\varepsilon_0 = 2.5\%}$	$\boldsymbol{\varepsilon_0 = 5\%}$	$\boldsymbol{\varepsilon_0 = 10\%}$
Current = 0A			
1	91.39	95.74	-
2.5	-	94.88	95.18
5	97.39	96.98	96.48
7.5	97.10	96.10	97.30
10	-	-	95.92
Current = 2A			
1	96.59	98.81	-
2.5	97.34	98.87	94.53
5	95.80	94.88	98.04
7.5	94.28	95.65	95.55
10	95.33	-	-
Current = 4A			
1	-	98.78	94.65
2.5	99.13	93.58	95.36
5	93.81	94.19	98.28
7.5	92.66	96.01	96.84
10	95.83	96.52	92.57
Current = 6A			
1	95.44	99.37	95.54
2.5	96.79	93.56	92.56
5	94.72	93.02	91.18
7.5	91.08	94.50	96.94
10	95.12	95.05	97.31
Current = 8A			
1	93.23	90.24	95.25
2.5	92.45	91.97	96.74
5	90.62	90.97	96.44
7.5	91.07	93.24	89.32
10	92.47	93.34	91.88

Table B.3: Fitness value of the proposed model for the Cube MRF-E 20mm sample

Cube MRF-E 20mm			
Freq. (Hz)	$\boldsymbol{\varepsilon_0 = 2.5\%}$	$\boldsymbol{\varepsilon_0 = 5\%}$	$\boldsymbol{\varepsilon_0 = 10\%}$
Current = 0A			
1	82.45	91.60	-
2.5	89.47	94.67	-
5	88.16	93.58	-
7.5		92.56	-
10	90.68	91.21	-
Current = 2A			
1	82.51	91.97	-
2.5	89.29	90.93	-
5	91.27	93.20	-
7.5		99.64	-
10	96.03	98.03	-
Current = 4A			
1	96.68	84.46	-
2.5	82.03	93.08	-
5	86.58	88.40	-
7.5		98.67	-
10	82.99	97.70	-
Current = 6A			
1	92.71	93.94	-
2.5	86.19	89.49	-
5	84.98	89.33	-
7.5		96.06	-
10	97.50	97.14	-
Current = 8A			
1	90.56	90.95	-
2.5	86.42	80.49	-
5	81.96	85.49	-
7.5		94.59	-
10	96.75	72.63	-

Table B.4: Fitness value of the proposed model for the Cylinder MRE 20mm sample

Cylinder MRE 20mm			
Freq. (Hz)	$\boldsymbol{\varepsilon_0 = 2.5\%}$	$\boldsymbol{\varepsilon_0 = 5\%}$	$\boldsymbol{\varepsilon_0 = 10\%}$
Current = 0A			
1	90.20	97.53	97.31
2.5	89.33	95.17	93.82
5	97.37	98.56	99.13
7.5	97.09	-	-
10	96.70	-	-
Current = 2A			
1	93.11	97.60	92.45
2.5	97.61	94.26	95.77
5	95.34	96.27	98.19
7.5	95.49	-	-
10	94.37	92.07	93.20
Current = 4A			
1	92.01	98.86	90.18
2.5	91.01	97.55	-
5	95.83	94.76	92.00
7.5	89.66	-	-
10	94.07	93.57	90.70
Current = 6A			
1	91.87	92.56	89.44
2.5	87.64	89.86	89.85
5	86.96	92.03	90.52
7.5	-	-	-
10	95.96	95.95	99.28
Current = 8A			
1	91.30	89.12	88.72
2.5	83.42	92.43	81.20
5	93.89	93.05	87.19
7.5	-	-	-
10	92.64	92.29	92.35

Table B.5: Fitness value of the proposed model for the Cylinder MRE 30mm sample

Cylinder MRE 30mm			
Freq. (Hz)	$\boldsymbol{\varepsilon_0 = 2.5\%}$	$\boldsymbol{\varepsilon_0 = 5\%}$	$\boldsymbol{\varepsilon_0 = 10\%}$
Current = 0A			
1	-	-	-
2.5	-	98.35	96.52
5	98.48	98.75	97.37
7.5	98.50	97.63	99.24
10	97.95	96.83	97.35
Current = 2A			
1	-	-	-
2.5	94.66	97.97	96.56
5	96.76	96.36	98.10
7.5	95.29	92.56	96.76
10	95.11	96.00	94.84
Current = 4A			
1	-	-	-
2.5	96.62	95.61	93.81
5	97.07	96.24	94.62
7.5	96.27	95.52	93.60
10	95.00	95.35	91.32
Current = 6A			
1	-	-	-
2.5	91.61	93.87	94.39
5	95.11	91.44	94.99
7.5	93.13	97.42	97.53
10	95.61	99.05	95.12
Current = 8A			
1	-	-	-
2.5	93.88	92.30	90.92
5	92.04	94.42	94.76
7.5	97.09	98.61	89.91
10	-	99.21	94.48

Table B.6: Fitness value of the proposed model for the Cylinder MRF-E 20mm sample

Cylinder MRF-E 20mm			
Freq. (Hz)	$\boldsymbol{\varepsilon_0 = 2.5\%}$	$\boldsymbol{\varepsilon_0 = 5\%}$	$\boldsymbol{\varepsilon_0 = 10\%}$
Current = 0A			
1	85.16	80.82	-
2.5	86.85	-	-
5	93.10	96.15	-
7.5	-	82.09	-
10	87.40	81.72	-
Current = 2A			
1	79.64	93.76	-
2.5	86.45	-	-
5	90.15	80.26	-
7.5	-	81.82	-
10	-	97.40	-
Current = 4A			
1	-	89.03	-
2.5	78.43	88.51	88.84
5	-	85.75	87.57
7.5	-	-	84.48
10	93.06	96.18	-
Current = 6A			
1	90.10	83.05	88.71
2.5	88.86	82.62	81.98
5	-	78.16	80.97
7.5	-	-	89.80
10	94.48	98.28	92.76
Current = 8A			
1	-	77.45	80.65
2.5	-	79.85	79.56
5	-	82.62	76.55
7.5	-	68.84	85.23
10	93.85	98.05	71.97

Appendix C

Table C.1: Percent error between proposed model and measured elastic modulus for Cube MRE 20mm sample

Cube MRE 20mm			
Freq. (Hz)	$\boldsymbol{\varepsilon_0 = 2.5\%}$	$\boldsymbol{\varepsilon_0 = 5\%}$	$\boldsymbol{\varepsilon_0 = 10\%}$
Current = 0A			
1	4.54	5.26	8.08
2.5	1.69	0.62	3.05
5	1.51	0.31	0.36
7.5	0.93	2.31	1.34
10	1.10	3.56	2.06
Current = 2A			
1	0.03	1.70	7.69
2.5	1.13	1.40	2.65
5	2.32	2.51	0.36
7.5	1.74	2.96	2.64
10	0.10	4.64	3.53
Current = 4A			
1	0.47	0.57	6.33
2.5	1.16	2.31	3.01
5	1.08	1.10	0.48
7.5	0.17	1.68	1.38
10	2.50	2.39	0.10
Current = 6A			
1	0.11	1.60	3.50
2.5	0.42	1.77	1.94
5	0.10	0.89	1.14
7.5	2.97	0.15	2.08
10	2.78	0.59	2.18
Current = 8A			
1	2.57	3.42	0.44
2.5	2.81	3.55	0.42
5	2.09	0.54	2.15
7.5	2.46	1.35	0.44
10	3.48	0.18	2.14

Table C.2: Percent error between proposed model and measured elastic modulus for Cube MRE 30mm sample

Cube MRE 30mm			
Freq. (Hz)	$\boldsymbol{\varepsilon_0 = 2.5\%}$	$\boldsymbol{\varepsilon_0 = 5\%}$	$\boldsymbol{\varepsilon_0 = 10\%}$
Current = 0A			
1	5.73	4.43	-
2.5	-	3.33	4.70
5	0.71	1.01	0.72
7.5	0.40	2.42	1.84
10	-	4.32	2.79
Current = 2A			
1	3.17	0.63	-
2.5	1.95	1.24	4.03
5	0.14	3.41	0.21
7.5	0.09	3.99	1.51
10	1.18	-	-
Current = 4A			
1	-	1.25	4.68
2.5	0.53	0.24	3.67
5	2.36	2.35	0.82
7.5	0.51	1.98	0.58
10	0.98	2.31	1.54
Current = 6A			
1	3.74	0.60	2.87
2.5	0.23	2.26	1.62
5	0.35	0.24	0.49
7.5	2.61	1.44	0.44
10	1.63	0.14	0.40
Current = 8A			
1	6.63	5.17	0.32
2.5	2.43	3.30	1.38
5	2.07	0.98	0.55
7.5	3.64	1.23	0.46
10	2.39	1.01	0.83

Table C.3: Percent error between proposed model and measured elastic modulus for the Cube MRF-MRE 30mm sample

Cube MRF-MRE 30mm			
Freq. (Hz)	$\boldsymbol{\varepsilon_0 = 2.5\%}$	$\boldsymbol{\varepsilon_0 = 5\%}$	$\boldsymbol{\varepsilon_0 = 10\%}$
Current = 0A			
1	15.20	-	-
2.5	-	-	-
5	-	-	-
7.5	-	-	-
10	-	-	-
Current = 2A			
1	17.72	8.36	-
2.5	8.10	-	-
5	-	-	-
7.5	-	5.08	8.17
10	-	-	-
Current = 4A			
1	5.34	7.36	2.86
2.5	0.57	2.00	2.31
5	2.06	5.01	2.24
7.5	-	0.71	4.13
10	-	-	7.37
Current = 6A			
1	2.09	4.23	1.89
2.5	5.12	1.83	2.16
5	-	3.28	0.56
7.5	-	4.12	2.45
10	-	2.17	4.46
Current = 8A			
1	2.29	2.99	0.45
2.5	1.66	2.23	1.75
5	1.14	0.12	0.37
7.5	-	0.34	1.30
10	-	0.93	0.07

Table C.4: Percent error between proposed model and measured elastic modulus for the Cube MRF-E 20mm sample

Cube MRF-E 20mm			
Freq. (Hz)	$\varepsilon_0 = 2.5\%$	$\varepsilon_0 = 5\%$	$\varepsilon_0 = 10\%$
Current = 0A			
1	11.86	3.67	-
2.5	5.69	2.80	-
5	0.66	1.97	-
7.5	-	2.38	-
10	4.26	7.17	-
Current = 2A			
1	3.64	6.00	-
2.5	1.72	1.94	-
5	3.51	1.87	-
7.5	-	0.01	-
10	0.52	1.40	-
Current = 4A			
1	0.26	0.67	-
2.5	1.27	2.27	-
5	1.46	0.05	-
7.5	-	0.81	-
10	2.12	0.37	-
Current = 6A			
1	2.23	2.55	-
2.5	2.98	0.84	-
5	2.54	0.39	-
7.5	-	1.64	-
10	1.70	2.66	-
Current = 8A			
1	1.16	3.67	-
2.5	2.64	0.44	-
5	2.04	0.76	-
7.5	-	1.43	-
10	2.38	1.75	-

Table C.5: Percent error between proposed model and measured elastic modulus for the Cylinder MRE 20mm sample

Cylinder MRE 20mm			
Freq. (Hz)	$\boldsymbol{\varepsilon_0 = 2.5\%}$	$\boldsymbol{\varepsilon_0 = 5\%}$	$\boldsymbol{\varepsilon_0 = 10\%}$
Current = 0A			
1	2.97	0.69	2.70
2.5	5.48	3.30	5.25
5	2.42	0.53	0.31
7.5	2.20	-	-
10	2.49	-	-
Current = 2A			
1	1.06	2.33	1.90
2.5	0.18	0.65	4.21
5	1.57	2.92	1.46
7.5	1.96	-	-
10	4.67	7.94	4.97
Current = 4A			
1	1.98	1.18	1.34
2.5	0.93	1.16	-
5	0.16	2.96	0.11
7.5	0.33	-	-
10	2.02	1.35	3.38
Current = 6A			
1	2.19	0.07	0.14
2.5	4.16	3.60	3.62
5	4.58	3.43	2.63
7.5	-	-	-
10	0.80	3.09	0.28
Current = 8A			
1	5.63	3.89	5.81
2.5	0.77	0.24	0.63
5	1.59	1.23	0.31
7.5	-	-	-
10	0.00	0.31	1.39

Table C.6: Percent error between proposed model and measured elastic modulus for the Cylinder MRE 30mm sample

Cylinder MRE 30mm			
Freq. (Hz)	$\boldsymbol{\varepsilon_0 = 2.5\%}$	$\boldsymbol{\varepsilon_0 = 5\%}$	$\boldsymbol{\varepsilon_0 = 10\%}$
Current = 0A			
1	-	-	-
2.5	-	0.45	3.20
5	0.44	1.31	1.09
7.5	0.21	2.73	0.39
10	0.98	2.49	0.94
Current = 2A			
1	-	-	-
2.5	2.34	1.85	1.51
5	0.29	3.31	0.37
7.5	0.40	3.81	0.84
10	2.08	2.87	0.04
Current = 4A			
1	-	-	-
2.5	2.08	2.55	1.36
5	1.45	2.65	1.50
7.5	0.08	2.35	1.56
10	0.23	1.06	0.19
Current = 6A			
1	-	-	-
2.5	2.53	4.11	1.77
5	0.77	1.06	2.70
7.5	0.70	0.89	1.28
10	3.12	0.70	2.20
Current = 8A			
1	-	-	-
2.5	1.81	5.84	1.91
5	1.10	3.56	0.84
7.5	1.47	0.60	1.43
10	-	1.00	0.82

Table C.7: Percent error between proposed model and measured elastic modulus for the Cylinder MRF-MRE 30mm sample

Cylinder MRF-MRE 30mm			
Freq. (Hz)	$\boldsymbol{\varepsilon_0 = 2.5\%}$	$\boldsymbol{\varepsilon_0 = 5\%}$	$\boldsymbol{\varepsilon_0 = 10\%}$
Current = 0A			
1	6.71	-	-
2.5	8.31	-	-
5	-	-	-
7.5	-	-	-
10	-	-	-
Current = 2A			
1	2.85	0.97	-
2.5	9.09	1.39	-
5	-	-	-
7.5	6.38	5.55	-
10	-	-	-
Current = 4A			
1	4.90	5.78	13.04
2.5	3.10	5.28	7.35
5	0.06	4.86	5.94
7.5	0.49	4.99	-
10	-	-	-
Current = 6A			
1	5.52	2.09	4.19
2.5	4.08	3.39	0.63
5	3.64	2.99	8.48
7.5	0.11	2.49	-
10	0.99	4.45	-
Current = 8A			
1	1.04	10.61	2.08
2.5	0.85	-	2.41
5	1.26	5.53	6.01
7.5	1.80	4.44	4.27
10	-	-	4.81

Table C.8: Percent error between proposed model and measured elastic modulus for the Cylinder MRF-E 20mm sample

Cylinder MRF-E 20mm			
Freq. (Hz)	$\boldsymbol{\varepsilon_0 = 2.5\%}$	$\boldsymbol{\varepsilon_0 = 5\%}$	$\boldsymbol{\varepsilon_0 = 10\%}$
Current = 0A			
1	1.08	5.04	-
2.5	1.15	-	-
5	0.09	2.26	-
7.5	-	0.33	-
10	2.10	1.62	-
Current = 2A			
1	1.21	2.59	-
2.5	0.53	-	-
5	0.30	3.08	-
7.5	-	3.04	-
10	-	1.00	-
Current = 4A			
1	-	0.45	-
2.5	0.82	1.12	4.32
5	-	0.96	0.94
7.5	-	-	0.36
10	0.39	3.65	-
Current = 6A			
1	7.27	0.49	3.46
2.5	3.34	0.57	2.58
5	-	2.48	0.68
7.5	-	-	1.18
10	0.75	1.69	4.62
Current = 8A			
1	-	1.48	8.51
2.5	-	1.49	3.29
5	-	3.16	1.33
7.5	-	1.03	1.18
10	0.09	1.85	7.23